# Study of the cellular detonation dynamics at the sub-cell and macro scales

by

Farzane Zangene

Thesis submitted to the University of Ottawa
in partial fulfillment of the requirements for
the Ph.D degree.
in
Department of Mechanical Engineering
Faculty of Engineering
University of Ottawa

## Publications

The research work presented in this thesis has been presented and published in the following articles.

1. **Zangene, F.**, Radulescu, M. (2024). Role of the argon and helium bath gases on the detonation structure of $H_2/O_2$ mixture. Submitted to *Combustion and Flame*. (Revision requested)

2. **Zangene, F.**, Radulescu, M. (2024). The critical conditions for the reignition and detonation formation from Mach reflections of curved decaying shocks. *Proceedings of the Combustion Institute*, 40(1-4), 105774.

3. **Zangene, F.**, Xiao, Q., Radulescu, M. (2022). Critical diffraction of irregular structure detonations and their predictability from experimentally obtained $D$-$\kappa$ data. *Proceedings of the Combustion Institute*, 39(3), 2935-2944.

### Conference Proceedings

1. **Zangene, F.**, Yang, H., Radulescu, M. (June 2024). Pressure dynamics resulting from head-on reflection of detonation. In *Proceedings of the 15$^{th}$ International Symposium on Hazards, Prevention, and Mitigation of Industrial Explosions*, Naples, Italy.

2. **Zangene, F.**, Radulescu, M. (May 2024). Detonation formation and reignition following the Mach reflection of two decaying curved shocks. In *Proceedings of the Combustion Institute Canadian Section*, Kingston, Canada.

3. Yang, H., Wang, W., **Zangene, F.**, Cheevers, K., Maley, L., Radulescu, M. (July 2023). Detonation attenuation and quenching in hydrogen mixtures after the interaction with cylinders. In *Proceedings of the 34$^{th}$ International Symposium on Shock Waves*, Daegu, Korea.

4. **Zangene, F.**, Radulescu, M. (July 2023). Modelling and experiments of triple point reflection in detonations. In *Proceedings of the 34$^{th}$ International Symposium on Shock Waves*, Daegu, Korea.

5. **Zangene, F.**, Radulescu, M. (July 2023). The critical conditions for forming a Mach from shock reflections. In *Proceedings of the 29$^{th}$ International Colloquium on Dynamics of Explosions and Reactive Systems*, Seoul, Korea.

6. **Zangene, F.**, Sow, A., Radulescu, M. (June 2022). Predictability of $H_2/O_2/Ar/He$ detonations in thin channels: new experiments and improvements in the quasi-two-dimensional model. In *Proceedings of the 28$^{th}$ International Colloquium on Dynamics of Explosions and Reactive Systems*, Naples, Italy.

7. Radulescu, M., Pekalski, A., **Zangene, F.** (June 2022). The explosion length as a measure of detonability: Review of data in methane and hydrogen. In *Proceedings of the 10$^{th}$ International Seminar on Fire and Explosion Hazards*, Oslo, Norway.

8. **Zangene, F.**, Qiang, X., Radulescu, M. (May 2022). Prediction of the critical diffraction in unstable detonation. *Combustion Institute Canadian Section*, Ottawa, Canada.

9. **Zangene, F.**, Hong, Z., Xiao, Q., Radulescu, M. (September 2021). The role of the argon and helium bath gases on the detonation structure of $H_2/O_2$ mixture. In *Proceedings of the 9$^{th}$ International Conference on Hydrogen Safety*, Edinburgh, Scotland.

**Conference Abstracts**

1. **Zangene, F.**, Radulescu, M. (November 2023). The critical conditions for the formation of the Mach shock from shock reflections. *The 76$^{th}$ Annual Meeting of the APS, Division of Fluid Dynamics*, Washington, United States.

## Declaration of Authorship

I hereby certify that this thesis is entirely my own original work except where otherwise indicated. I am aware of the University of Ottawa regulations concerning plagiarism, including those regarding consequent disciplinary actions. Any use of the works of any other author, in any form, is properly acknowledged at their point of use.

## Abstract

This thesis, presented as a series of articles, aims to provide a deeper understanding of how small-scale dynamics, i.e., the cellular structure of the reaction zone, influence large-scale dynamics, i.e., the shape and dynamics of the wave globally, and to develop a rational model for predicting the detonation dynamics at these large scales. Previous studies on detonation propagation in curved channels and suddenly enlarging area have shown that, while the detonation front remains cellular, the geometry induces a global curvature that is integrated over many cells. The resulting detonation dynamics can be effectively described by a speed-curvature ($D - \kappa$) relationship, where non-steady effects are negligible at this scale. However, both curvature and non-steady effects are very important when investigating the detonation behaviour at the cellular level. This thesis aims to elucidate these effects through experimental analyses and modelling of detonation dynamics and behaviour.

The first article, presented in Chapter 2, investigates the evolution of a multi-cellular, irregular detonation structure, predicting its behaviour based on the global response of the detonation front to geometric influences. We introduce new experiments on detonation diffraction in a 2D channel, focusing on the highly irregular cellular structure of detonations in stoichiometric mixtures of ethylene, ethane, and methane with oxygen as the oxidizer. The critical conditions for detonation diffraction and the critical channel height for each mixture are determined experimentally. Critical curvature data obtained from single-headed detonation experiments conducted in a separate study were found to provide a good prediction of critical diffraction in detonation diffraction experiments. This finding supports the view that the concept based on the ($D - \kappa$) relationship is meaningful in predicting critical diffraction of irregular structure detonations.

Chapter 3 examines whether incorporating the global effect of curvature is a relevant approach to understanding the weakly transient phenomenon of detonation initiation. A novel experimental technique is proposed to isolate detonation formation from the reflection of two decaying shocks. The test gases include a regular cellular structure mixture of $2H_2/O_2/2Ar$ and a highly irregular cellular structure of $CH_4/2O_2$. Through these experiments, we identified three distinct regimes: detonation formation, a Mach shock followed by a flame, and a case where no ignition occurs behind the Mach shock. The transition between detonation formation and ignition was found to follow the critical curvature theory of quasi-steady curved detonations closely. Moreover, the boundary between re-ignition and no re-ignition was accurately predicted by the critical decay rate theory.

In Chapter 4, we study the propagation of detonation waves in narrow channels which are subjected to boundary layer losses. The effect of boundary layer losses appears as the lateral divergence of the flow due to the increase in boundary layer displacement thickness. Two highly regular cellular structure mixtures of $2H_2/O_2/7Ar$ and $2H_2/O_2/7He$ are employed as test gases. Both diluents, argon and helium, have identical kinetics, Mach number, and specific heat ratio; however, their transport properties differ. The experiments showed variations in velocity deficits and cell sizes, despite being designed to maintain a constant induction zone length across the mixtures. These differences were explained by modelling the impact of global lateral flow divergence caused by boundary layer losses.

Therefore, it appears that the large-scale dynamics are controlled by the long reaction zone thickness and are decoupled from the rapid dynamics of the front.

In Chapter 5, we use the same experimental setup—a narrow channel—to investigate the hydrodynamic thickness of detonations in the regular mixture of $2H_2/O_2/7Ar$ and irregular mixture of $CH_4/2O_2$ cellular structures. We experimentally measure the mean pressure evolution within a detonation cell as well as the pressure changes resulting from the head-on reflection of the detonation wave. Our experiments show that, on a global scale, the hydrodynamic thickness corresponds to the length of one cell in both mixtures. Furthermore, we confirm that the overall pressure evolution of the detonation wave and its reflection can be accurately reconstructed using the one-dimensional ZND model for the regular mixture. For the irregular mixture, we introduce a simplified one-step model tailored to the global structure of the reaction zone. Building on the work presented in Chapter 4, we further confirm that in narrow channel experiments, the large-scale dynamics, in mixtures characterized by the extended reaction zone, can be decoupled from the fast dynamics of the front. These findings suggest that a physically accurate model of the reaction zone is adequate to capture the detonation dynamics.

In Chapter 6, we take the next step toward developing a sub-cellular model within a cell. While transient effects are crucial within a detonation cell, the onset of the reaction occurs much faster initially than its decay rate. Therefore, this work focuses on predicting detonation dynamics within a single cell, specifically determining the shock strength at the start of the cell based on its strength at the end. To achieve this, we reformulate the triple-point reflection model, assuming that the Mach shock is reactive. The objective is to predict the strength of the lead shock following the triple-point collision. The model's predictions are then compared to experimental data from detonations propagating in narrow channels with an enlarged cell structure, with high-speed schlieren imaging capturing the reflection dynamics. Despite experimental uncertainties, the model demonstrates a strong agreement with the observed results.

**Acknowledgements**

First and foremost, I would like to express my deepest gratitude to my supervisor, Professor Matei. I Radulecu, for his unwavering support, guidance, and mentorship throughout this PhD journey. The path has been challenging at times, but his consistent encouragement and support made the process not only manageable but also rewarding and memorable. I am particularly grateful for his dedication to helping me grow both as a researcher and as a person, pushing me to uncover my full potential. His ability to challenge me in constructive ways allowed me to identify and improve my weaknesses, while also enhancing my strengths and using them to their fullest.

I would like to express my heartfelt gratitude to all my friends and colleagues in the Detonation and Reactive Dynamics Laboratory (DRDL) and the office at the University of Ottawa for their support, insightful discussions, and the unforgettable memories we've shared beyond the academic sphere. This journey would not have been as enjoyable without their presence.

Finally, I am deeply grateful to my family for standing by me every step of the way, believing in me, and offering their unconditional support throughout this process. Their love and encouragement have been my constant source of strength.

# Table of Contents

# Chapter 1

# Introduction

## 1.1 Motivation

Supersonic self-sustained combustion waves, called detonations, are composed of a strong leading shock wave closely followed by a reaction zone. The gas is heated after passing through the strong shock due to the compression, which subsequently initiates the reaction. The leading shock is sustained as a result of the expansion of the gases due to the rapid deposition of the chemical energy [1–3]. These characteristics make detonation waves ideal for use in advanced propulsion systems, such as rotating detonation engines, pulse detonation engines, and oblique detonation engines. The majority of self-sustaining detonations occurring in gaseous explosive mixtures exhibit a non-steady, three-dimensional cellular structure [2, 4, 5] comprised of the incident, Mach and transverse shocks. The periodic interaction of these three shock waves in reactive mixtures forms the cellular structure of the detonation [2]. In a detonation cell, the local details of reaction zone structure dictate how fast is energy being released and how fast it amplifies local gas dynamic phenomena [6]. Despite decades of research and detailed studies of cellular structures [7, 8], predicting detonation dynamics on an engineering scale is currently not feasible because of the experimental and numerical challenges in resolving the fine scales of the detonation, the nonlinear coupling between chemistry and gas dynamics, as well as the inherent instability of the flow [9]. This highlights the need for physics-informed macroscopic models that can be used for predictive purposes.

The primary objectives of this thesis are to investigate how small-scale dynamics, i.e., cellular structure, influence large-scale detonation behaviour, i.e., global wavefront, and to develop a rational model capable of predicting large-scale dynamics relevant to engineering applications.

## 1.2 Detonation cellular structure, local dynamics

It is well-established that detonation waves in gases exhibit a three-dimensional and transient cellular structure. Numerous researchers have studied the structure of propagating

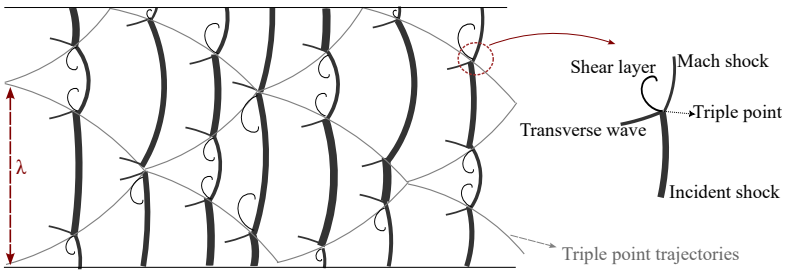


Figure 1.1: Schematic of the detonation cellular structure; the detonation wave propagates from left to right.

detonation waves through both experimental and numerical approaches [5]. The first evidence of this cellular structure was obtained in the early 1960s by Denisov and Troshin using soot foils [10], followed by White using interferometry [11], and more widely through the schlieren technique [12].

The key feature of the detonation structure is the triple point, which intersects the incident shock, Mach shock, and the transverse shock. The detonation wave structure and its cell diamond shape are shown in Fig. 1.1. The triple point collisions lead to the formation of a cellular structure that is a manifestation of the front instability [2, 5, 13]. During cellular pulsation, the gas behind the weaker part of the front accumulates as unreacted for a much longer time. The remaining unreacted gases will further heat up and react by passing through the transverse waves which move perpendicular to the front. In each cell, the leading shock is continuously decaying and only re-amplifies when two triple points collide and give rise to a new stronger shock. The formation of a diamond shape following the intersection of triple points has been previously observed in experiments using soot foils [5, 14, 15]. The variable $\lambda$ is an important length scale indicating the cell size. In a variety of problems, $\lambda$ finds widespread application in characterizing detonation limits, direct initiation energy, and the critical tube diameter associated with detonations [5]. Experimental and numerical studies have shown that the global reaction zone thickness corresponds to approximately $4\lambda$ [6, 16] and $120\Delta_i$, where $\Delta_i$ is the induction zone length based on Zel'dovich-von Neumann-Döring (ZND) model [17–19].

The cellular structure of detonation differs based on the sensitivity of the tested mixture. Schlieren and soot foil observations records of detonation front identified two types of cellular structures, regular and irregular, illustrated in Fig. 1.2. Mixtures with high argon dilution exhibit a very regular structure whereas those with nitrogen dilution or hydrocarbon mixtures display a more irregular cellular structure [7, 21]. For lower activation energies the detonations with less sensitive chemical reactions to temperature perturbation have a regular structure, shown in Fig. 1.2 (a). The reaction zone structures of regular detonations are typically laminar and adiabatic shock compression is the main mechanism of ignition, which can be effectively predicted using the ZND model. This model only considers the ignition delay history of a shocked particle and treats a detonation as a one-dimensional steady inviscid reactive wave with no cellular structure. On the other hand, Fig. 1.2 (b) shows the schlieren visualizations of the detonation structure in the irregular

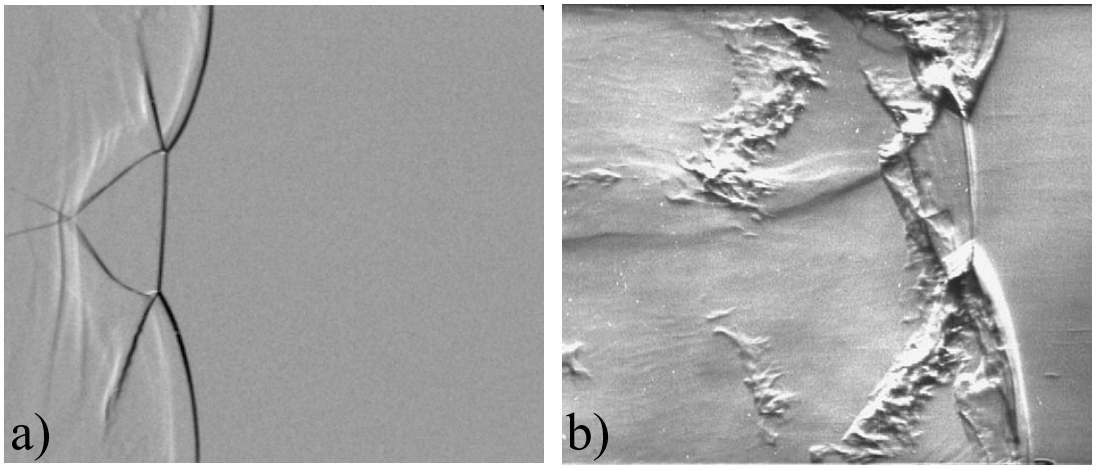


Figure 1.2: Schlieren images of detonation propagation in a) regular cellular structure of $2H_2/O_2/7Ar$ mixture [20] and b) irregular cellular structure of $CH_4/2O_2$ mixture [6].

cellular structure of $CH_4/2O_2$ mixture. In irregular structure detonation, chemical activities primarily occur on a small scale at the front of the wave. As the wave propagates, pockets of unreacted gas can separate from the front, leading to further randomization of the reaction process. This separation is often caused by transverse waves that travel perpendicular to the main propagation direction of the detonation wave and contribute to the complex dynamics and behaviour of the detonation wave, including the formation of the cellular structures and the mixing of reactants with unreacted regions. In these mixtures, the ignition mechanism is a combination of adiabatic shock compression and turbulent combustion [3, 22]. Therefore, the ZND model does not accurately predict the structure behind the detonation front in irregular mixtures [6, 23, 24].

Determining the role of the cellular structure on detonation dynamics in the limit of propagation, particularly in sensitive mixtures with irregular structures has been one of the main challenges in detonation research. The question that still lacks a response pertains to the influence of cellular dynamics, where both curvature and non-steady effects are significant, on overall energy release and the methods by which these influences can be integrated into a macroscopic model.

## 1.3 Detonation waves with laterally diverging flows, global dynamics

Extensive experiments have been conducted on detonation propagation in curved channels and suddenly enlarging area [27–30]. These studies show that, although the detonation front remains cellular, the influence of geometry causes it to become globally curved, as shown in Fig. 1.3. In a quasi-planar detonation wave, the large-scale dynamics of a cellular front can be viewed as a collection of individual mean ray tubes, each containing one cell. At small scales, this involves the reaction zone structure with triple-point collisions. When

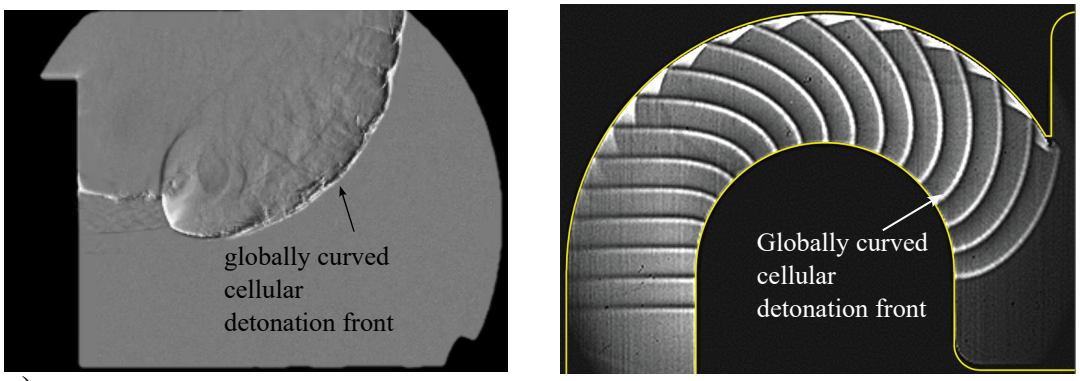


a) b)

Figure 1.3: Examples of curved detonation fronts occurring in a) diffraction around a corner [25] b) curved channel [26].

analyzing detonation dynamics, it is unclear whether the focus should be a global one emphasizing the effect of global curvature or a local one where the explosion originates from triple point collisions on the front and controls the reactivity. However, empirical evidence [26, 27] has demonstrated that detonation dynamics can be effectively captured by a speed-curvature, $D - \kappa$, relationship [24, 26, 27], where the curvature is a global one averaged over several cells. Considering that the cellular structure and the global reaction zone thickness are much smaller than the characteristic radius of the front, one can treat the detonation front as a thin front and disregard the details of what happens within its thickness. This suggests that the large-scale dynamics of detonations can be potentially described by a much simpler description of a global reaction rate dictating the macro-scale effective kinetics. Additionally, analyses of unstable detonations have shown that, despite their inherently multi-dimensional nature with turbulent reaction zones, the structure often recovers a quasi-one-dimensional average form similar to the ZND model, including an average sonic surface [31–33]. This suggests that, with a suitable kinetic description for the averaged fluid state and a speed determined by an effective rate of energy release, the ZND model and its extensions can provide an appropriate framework for modelling real detonations at a macro-scale. In this regard, by extending the classical ZND model, several models for one-dimensional detonation waves have been developed to account for non-ideal effects such as flow divergence and unsteadiness [5, 34]. A comprehensive review of theories related to quasi-one-dimensional, quasi-steady detonation shock evolution can be found in the recent review of Bdzil and Stewart [34].

### 1.3.1 Controlling mechanism in globally curved detonations

The propagation of a curved detonation wave can be studied as a series of quasi-steady waves with an area enlargement. As illustrated in Fig. 1.4, when a curved front results in an increase in surface area, $A_f$, the curvature is defined as $\kappa = \frac{1}{A}\frac{dA_f}{dx}$. When the radius of curvature is much larger than the global reaction zone thickness, unsteady effects can be

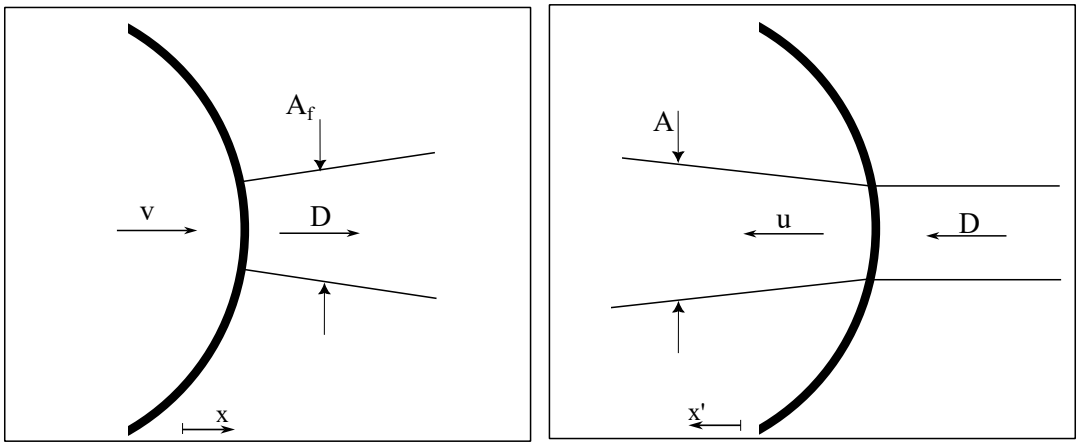


a) Laboratory reference frame b) Shock reference frame

Figure 1.4: Laterally divergenc of the flow in detonation attached reference frame.

neglected. The local description of the wave structure can be approximated as a quasi-1D flow, with the streamtube area increase given in terms of the front curvature by $\alpha = \frac{d \ln A_f}{dx} = \frac{v}{u}\kappa$. To solve the governing equations directly, the governing equations—generalized ZND equations for detonations with lateral flow divergence—can be integrated explicitly. Details on the direct integration method can be found in the works of Klein et al [35] and Radulescu and Borzou [24]. The steady, inviscid, reacting quasi-1D governing equations with a source term can be expressed in the frame of reference attached to the shock front:

$$\frac{dp}{dx'} = -\rho v \frac{(\dot{\sigma} - v\alpha)}{1 - M^2} \tag{1.1}$$

$$\frac{d\rho}{dx'} = -\frac{\rho}{v}\frac{(\dot{\sigma} - vM^2\alpha)}{1 - M^2} \tag{1.2}$$

$$\frac{dv}{dx'} = \frac{(\dot{\sigma} - v\alpha)}{1 - M^2} \tag{1.3}$$

here, $p$, $\rho$, $v$, and $M$ represent the pressure, density, velocity, and Mach number of the flow in the post-shock region, within the shock-attached reference frame. $\dot{\sigma}$ denotes the thermicity, while $v\alpha$ represents the strain rate due to the lateral divergence of the flow. By directly integrating the governing equations, one can determine how the velocity depends on the flow divergence [24, 35].

Figure 1.5 presents the numerically obtained $D-\kappa$ curves for a mixture of $2H_2+O_2+2Ar$ at an initial pressure of 10 kPa, using the San Diego chemical mechanism [36]. In a curved detonation front, the divergence of the flow in the reaction zone, $v\alpha$, opposes the thermicity, $\dot{\sigma}$. In the shock-attached reference frame, the flow behind the shock starts subsonic. The thermicity accelerates the flow toward $M = 1$, while the diverging flow acts as a diffuser, decelerating it. Referring to the right-hand side of Eqs. (1.1), (1.2), and (1.3), as the flow approaches $M = 1$, if it reaches this point before the numerator reaches zero, the solution

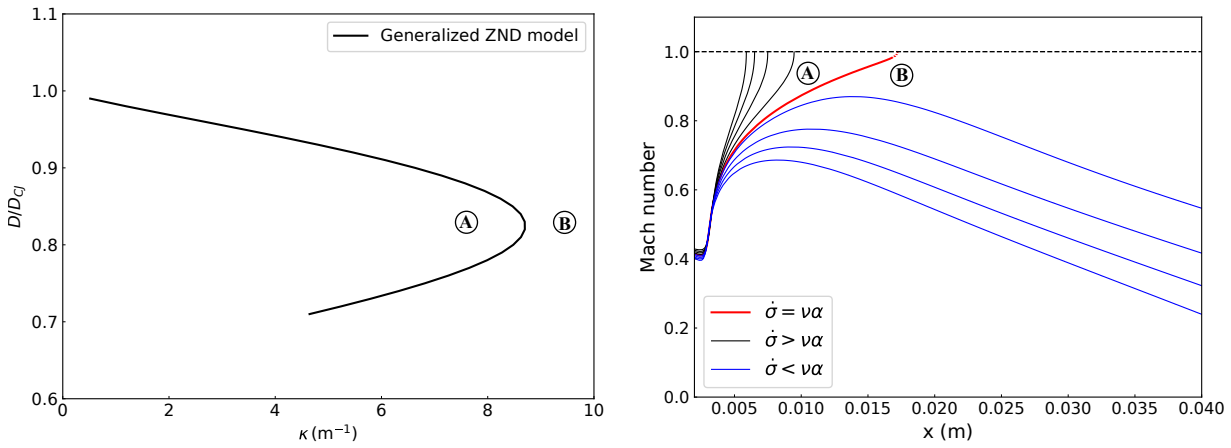


Figure 1.5: Relationship between the non-dimensional detonation velocity and the curvature of the front, $\kappa$, for the mixture $2H_2 + O_2 + 2Ar$ at $p_0 = 10\,\text{kPa}$, obtained using the San Diego chemical kinetic mechanisms.

blows up ($\dot{\sigma} > v\alpha$), as seen in region A of Fig. 1.5. This results in an unphysical solution. Conversely, if the post-shock flow is too slow, the flow never reaches $M = 1$, as the diffuser effect dominates ($\dot{\sigma} < v\alpha$), which corresponds to region B in Fig. 1.5. For a given level of lateral flow divergence, or equivalently front curvature ($\kappa$), there is a single value of post-shock speed that allows the flow to reach $M = 1$ as the numerator approaches zero simultaneously, $\dot{\sigma} - v\alpha = 0$, yielding a the valid physical solution. The sonic point, where $M = 1$, acts as a saddle point, with trajectories in region A ($M > 1$) and region B ($M < 1$) diverging from this point. Satisfying both zero thermicity and $M = 1$ corresponds to the generalized CJ conditions.

### 1.3.2 Analytical approximations

The steady traveling wave solution for quasi-one-dimensional flow in the presence of lateral flow divergence can be obtained using approximate models [37, 38]. These models are based on extensions of the classical one-dimensional ZND model, with deviations from the ZND model treated as perturbations. In this regard, the theoretical problem of steady detonations for weakly curved detonations has been investigated by He and Clavin [37], Klein et al. [35], Yao and Stewart [39], and others. The governing equations in the shock-attached reference frame (conservation of mass, momentum, and energy while neglecting viscosity and heat conduction) for quasi-1D flow are as follows:

$$\frac{d}{dx}(\rho u) = -\frac{2\rho(D-u)}{R_s - x} \tag{1.4}$$

$$\frac{d}{dx}(\rho u^2 + p) = -\frac{2\rho u(D-u)}{R_s - x} \tag{1.5}$$

$$\frac{d}{dx}\left(\frac{\gamma}{\gamma-1}\frac{p}{\rho}-q_c\lambda+\frac{u^2}{2}\right)=0 \tag{1.6}$$

here, $p$, $\rho$, $u$, $R_s$, and $D$ denote the pressure, density, flow velocity in the x-direction, shock radius and velocity of the leading shock, respectively. The chemical energy released per unit mass is represented by $q_c$, while $\lambda$ is the progress variable for the exothermic reaction, with $\lambda = 1$ in the burned gas and $\lambda = 0$ in the unburned gas. The perturbation analysis of the inner structure of detonations is carried out under the assumption of large activation energy for weakly curved fronts while using a quasi-steady-state approximation. This approximation holds when the characteristic timescale for changes in the radius and propagation velocity is much longer than the transit time of a fluid particle through the inner structure of the detonation wave. The equations mentioned above were integrated across the inner structure using a square wave model, where the chemical reaction is suppressed during the induction zone and completed instantaneously. As a result, the detonation thickness is approximately on the order of the induction length, $\Delta_i$.

$$\frac{(\rho_b u_b-\rho_u D)}{\rho_u D}\approx -I_1 \tag{1.7}$$

$$\frac{(\rho_b u_b^2+p_b)-(\rho_u D^2+p_u)}{\rho_u D^2}\approx -I_2 \tag{1.8}$$

$$\frac{\gamma}{\gamma-1}\frac{p_b}{\rho_b}+\frac{u_b^2}{2}\approx\frac{\gamma}{\gamma-1}\frac{p_u}{\rho_u}+\frac{D^2}{2}+q_c \tag{1.9}$$

where

$$I_1=\frac{2}{\rho_u D}\int_0^{\Delta_i}\frac{\rho(D-u)}{R_s-x}\,dx \tag{1.10}$$

$$I_2=\frac{2}{\rho_u D^2}\int_0^{\Delta_i}\frac{\rho u(D-u)}{R_s-x}\,dx \tag{1.11}$$

in the equations above, the subscript $u$ refers to the unburned gas, while $b$ denotes the burned gas. For weakly curved detonations, $\epsilon = \Delta_i/R_s \ll 1$, and since $I_1$ and $I_2$ are of the order of $\epsilon$, the inner structure of the detonation can be analyzed using perturbation methods in the limit of $\epsilon \ll 1$. Given that the right-hand side of the equations, $I_1$ and $I_2$, is small, they can be expressed in terms of the non-perturbed values at the shock state. Invoking also the dependence of the induction length on the perturbations, they derive the relationship between detonation speed and curvature as follows:

$$2\beta_N\left(\frac{D_{CJ}-D}{D_{CJ}}\right)\exp\left\{-2\beta_N\left(\frac{D_{CJ}-D}{D_{CJ}}\right)\right\}=\frac{16\gamma^2}{\gamma^2-1}\beta_N\frac{\Delta_{i,CJ}}{R_s} \tag{1.12}$$

where, $\beta_N$ represents the non-dimensional activation energy, $D_{\mathrm{CJ}}$ is the Chapman-Jouguet velocity, $\gamma$ is the specific heat ratio, and $\Delta_{\mathrm{CJ}}$ is the induction zone length referenced to the CJ state. The C-shaped curve shown in Fig. 1.6 is generated using Eq. (1.12) for $\gamma = 1.4$ and $\beta_N = 5.33$. This plot illustrates the maximum curvature, beyond which no solution exists for $\kappa > \kappa_{\max}$.

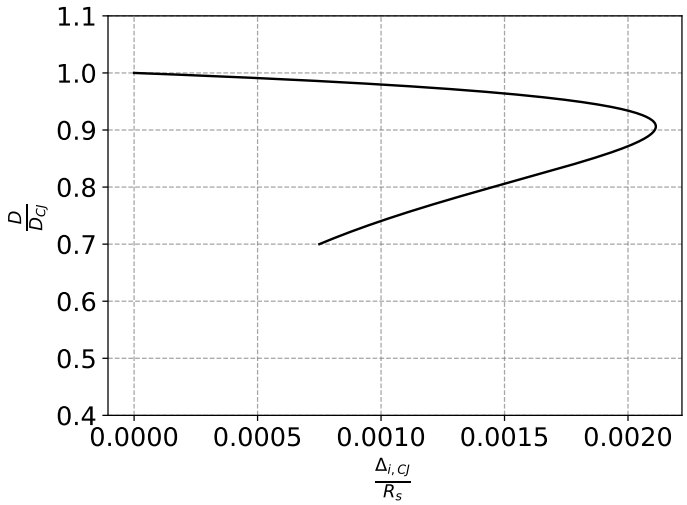


Figure 1.6: Non-dimensional detonation velocity versus non-dimensional curvature.

The analysis above can be extended to account for not only curvature but also weak unsteady effects as perturbations. As a result, an evolution equation that incorporates shock acceleration ($\dot{D}$)—specifically a $\dot{D}$–$D$–$\kappa$ relation—can be derived to describe the dynamics of the pre-existing detonation waves [40, 41].

While the theoretical framework for steady detonations with constant lateral flow divergence is well understood, Radulescu and Borzou [24] recently introduced an experimental technique using exponentially diverging ramps (exponential horns) to induce curved detonations, shown in Fig. 1.7. Their experiments ensured that detonations propagated in quasi-steady conditions with a constant mean lateral strain rate, corresponding to a constant mean front curvature. This was achieved by maintaining a constant derivative of the logarithmic cross-sectional area with respect to distance. Their experiments were conducted with two mixtures of varying instability: the highly irregular mixture of $C_3H_8/5O_2$ and the weakly irregular mixture of $2C_2H_2/5O_2/21Ar$. They reported $D(\kappa)$ curves for each mixture, noting that beyond a critical lateral strain rate, detonations become unsustainable. A comparison of experimentally obtained $D(\kappa)$ curves with those predicted by the generalized ZND model, accounting for lateral strain rates, showed better agreement in detonations with a more regular structure compared to irregular ones. They explained that in irregular mixtures the differences between the experiment and the inviscid model are due to the importance of diffusive processes in the burn-out of the non-reacted pockets.

Xiao and Radulescu [42] used the same experimental setup, the enlarging ramp, to study the details of detonation dynamics in regular cellular structure detonations. Their findings revealed excellent agreement between velocity deficits and the flow divergence predictions made by the steady ZND model with lateral strain rates for all the mixtures tested. Near the detonation propagation limit, minor discrepancies were observed, with experimental detonations continuing to propagate at slightly higher lateral strain rates and velocity deficits than predicted. Furthermore, in a different study [43] investigating detonation diffraction, the velocity-curvature data from quasi-steady detonation dynamics in ramp

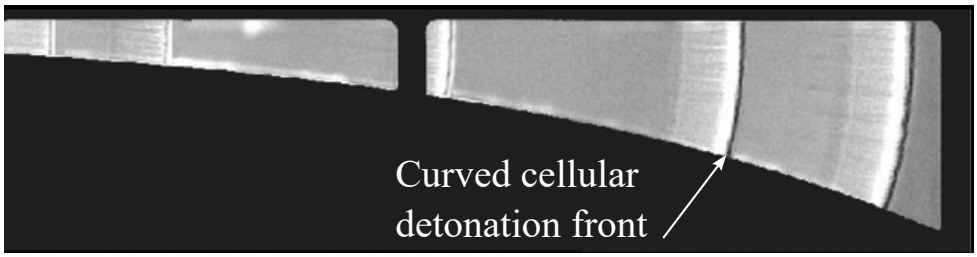


Figure 1.7: Detonation front evolution in themixture of $C_3H_8/5O_2$ along the long ramp at initial pressures of 12 kPa [24].

experiments showed a strong correlation with the $D(\kappa)$ data obtained from detonation diffraction experiments in similarly regular structures. This suggests that unsteady effects and cellular structures play a negligible role in the macro-scale dynamics of weakly unstable detonations, further explaining that the critical diffraction of such detonations can be captured by the maximum curvature of a steady ZND detonation.

In a follow-up study by the same authors [22], the experiments of detonation using enlarging ramps were extended to mixtures with irregular cellular structure, including stoichiometric methane-oxygen ($CH_4/2O_2$), ethylene-oxygen ($C_2H_4/3O_2$), and ethane-oxygen ($C_2H_6/3.5O_2$). The characteristic $D-\kappa$ relationships, which describe the mean propagation speeds and dimensionless flow divergence, were reported for each mixture, and compared with the generalized ZND model predictions for quasi-1D detonation dynamics under lateral strain, using detailed chemical kinetics. In general, the hydrocarbon-oxygen detonations observed in these experiments were found to propagate at significantly higher limiting global divergence rates and exhibited greater maximum velocity deficits than those predicted by the steady ZND model. This globally enhanced burning mechanism was attributed to intensified auto-ignition, assisted by turbulent diffusive burning of unreacted gas pockets.

## 1.4 Objectives and methodology

Considering the empirically established $D-\kappa$ relationship, it is possible to decouple the sub-scale phenomena of triple point collisions within the cellular structure from the larger-scale processes related to the front's propagation. This approach was used in experiments on detonation diffraction involving very regular cellular structures, where it was demonstrated that the influence of unsteadiness and cellular structure on the macro-scale dynamics of regular cellular structure detonations is limited, leading to a unique velocity-curvature relationship at macro scale [43]. The question is whether the evolution of a multi-cellular, irregular detonation structure can be predicted solely based on its response to geometric effects. To explore this, we conduct experiments on detonation diffraction in mixtures with highly irregular cellular structures. These experiments allow us to study the global dynamics of the diffracted wave, regardless of the fine-scale structure of the front. The details of this study are presented in Chapter 2 of this thesis.

The next question is whether incorporating the global effect of curvature will be effective in capturing transient phenomena of detonation formation. The experimental setup involves the interaction of two weakly decaying shock waves, resulting in the formation of a new Mach shock characterized by global curvature. This configuration allows us to investigate the $D - \kappa$ relationship in the context of detonation initiation. The details of this study are presented in Chapter 3 of this thesis.

Another scenario where lateral divergence plays a significant role in detonation is when it propagates through thin channels, where lateral flow divergence is driven by boundary layer effects along the side walls. Unlike the previous cases of detonation diffraction and initiation, the detonation in this configuration propagates as a quasi-steady wave, allowing for a clearer comparison of the coupling between the cellular structure and global divergence. In Chapter 4, we present the results of detonation propagation in narrow channels and further model the effects of these losses numerically at global scales.

In Chapter 5, we aim to establish a link between the transient dynamics at the sub-cellular level and a mean cell description, connecting the sub-scale phenomena with the global dynamics described by the ZND model. This approach is inspired by previous works that provided an averaged description of cellular detonations in numerical simulations [31–33]. We measure the mean pressure evolution of detonations propagating in narrow channels (considering the presence of losses) and examine whether this can be explained using a global 1D model.

To develop a predictive model within a detonation cell, one must link sub-scale processes to global kinetics, which requires a more detailed understanding of cell dynamics. In Chapter 6, as the first step toward creating a cell model, we extend shock polar analysis to reactive gases. A model is introduced that incorporates detailed chemical and thermodynamic properties to analyze reactive triple-point collisions. This model aims to predict the strength of the leading shock after these collisions, which defines the onset of the detonation cell.

# Chapter 2

# Critical diffraction of irregular structure detonations and their predictability from experimentally obtained $D$-$\kappa$ data

The first investigation is a test to see whether critical macro-scale curvature is a useful concept in the time-dependent problem of detonation diffraction at a corner. We explore the phenomenon of detonation diffraction, where lateral flow divergence is caused by the channel's geometry. The goal of this study is to assess whether the global dynamics of the diffracted wave can be accurately predicted using empirically measured $D - \kappa$ data from quasi-steady ramp experiments [22].

This study was published in *Proceedings of the Combustion Institute*, in 2022 and is included in the following pages of this thesis. The author carried out the experiments, performed the analysis, and wrote the paper. The second author, Qiang Xiao, contributed to the preliminary experiments of the detonation diffraction. Conceptual planning and paper editing were done in collaboration with the PhD supervisor, Prof. M. I. Radulescu.

Available online at www.sciencedirect.com

ScienceDirect

Proceedings of the Combustion Institute 39 (2023) 2935–2944

Proceedings of the Combustion Institute

www.elsevier.com/locate/proci

# Critical diffraction of irregular structure detonations and their predictability from experimentally obtained $D - \kappa$ data

Farzane Zangene [a,*], Qiang Xiao [a,b], Matei Radulescu [a]

[a] *Department of Mechanical Engineering, University of Ottawa, Ottawa, ON K1N6N5, Canada*
[b] *now at the National Key Laboratory of Transient Physics, Nanjing University of Science and Technology, Nanjing 210094, China*

Received 5 January 2022; accepted 14 November 2022
Available online 10 December 2022

**Abstract**

The present work reports new experiments of detonation diffraction in a 2D channel configuration in stoichiometric mixtures of ethylene, ethane, and methane with oxygen as oxidizer. The flow field details are obtained using high-speed schlieren near the critical conditions of diffraction. The critical initial pressure for successful diffraction is reported for the ethylene, ethane and methane mixtures. The flow field details revealed that the lateral portion of the wave results in a zone of quenched ignition. The dynamics of the laterally diffracting shock front are found in good agreement with the recent model developed by Radulescu et al. (Physics of Fluids 2021). The model provides noticeable improvement over the local models using Whitham's characteristic rule and Wescott, Bdzil and Stewart's model for weakly curved reactive shocks. These models provide a link between the critical channel height and the critical wave curvature. The critical channel heights and global curvatures are found in very good agreement with the critical curvatures measured independently by Xiao and Radulescu (Combust. Flame 2020) in quasi-steady experiments in exponential horns for three mixtures tested. Furthermore, critical curvature data obtained by others in the literature was found to provide a good prediction of critical diffraction in 2D. These findings suggest that the critical diffraction of unstable detonations may be well predicted by a model based on the maximum curvature of the detonation front, where the latter is to be measured experimentally and account for the role of the cellular structure in the burning mechanism. This finding provides support to the view that models for unstable detonations at a meso-scale larger than the cell size, i.e., hydrodynamic average models, are meaningful.


*Keywords:* Diffraction; Irregular structure detonations; Critical curvature

## 1. Introduction

The diffraction of detonations at an abrupt area change is a fundamental problem of detonation dynamics. The critical tube diameter $d_c$ (or channel

* Corresponding author.
*E-mail address:* fzang055@uottawa.ca (F. Zangene).

https://doi.org/10.1016/j.proci.2022.11.004

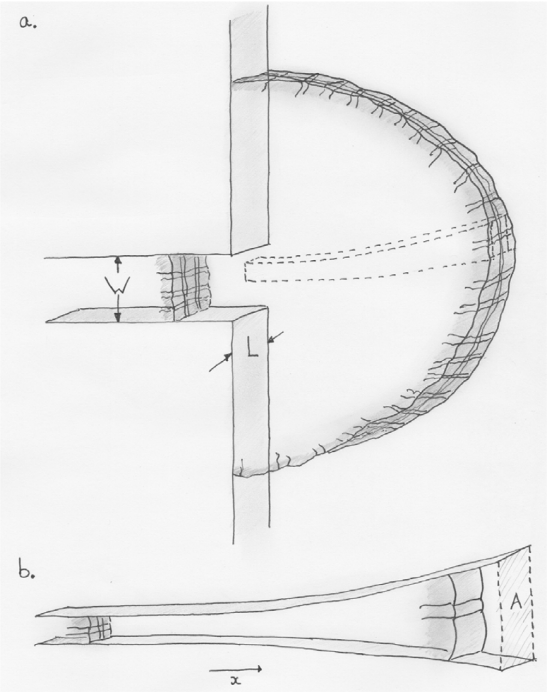


Fig. 1. The diffraction of a detonation wave from a slot (a) and the concept of a unit-cell ray tube of lateral divergence rate $\kappa = \mathrm{d}\ln A/\mathrm{d}x$ to characterize the dependence $D(\kappa)$ for cellular detonations [13,14].

slot height $W_c$ in two-dimensional channels) is considered a measure of the detonability of detonations. It is known empirically to depend on other such dynamic parameters, offering an alternative measure of a length scale proportional to the detonation reaction zone thickness (cell size, hydrodynamic thickness, critical explosion length for direct initiation) [1,2]. For a wide range of mixtures, empirical evidence suggests that $d_c/\lambda \simeq 13$ ($\lambda$, detonation cell size) for detonation diffraction from tubes, while a generally larger value is observed in detonations with very regular structures [3]. The good correlation with cell size suggests the importance of the cellular dynamics in controlling the detonability of gases.

For the equivalent problem in 2D, the situation is more complicated. When a planar cellular detonation propagates in a channel of depth $L$ and height $W$ and transits into a much larger channel of the same depth $L$ (Fig. 1), the empirical evidence suggests the limit $W_c/\lambda$ is very strongly influenced by the width of the channel $L$ [4–7]. For thin channels, where there are nominally less than one cell across, i.e., $L/\lambda \lesssim 1$, and the cellular structure approaches a 2D structure, the limit observed was $W_c/\lambda \simeq 10$ [4,8,9]. In much wider channels in which the detonation cellular structure is 3D, the limit varies between $W_c/\lambda \approx 3$ and $W_c/\lambda \approx 6$, with a smaller value in more irregular systems. At present, this variation from 3 to 10 is not well understood.

A possible explanation is the known intrinsic difference in cellular dynamics between 2D and 3D cellular structures, preliminary results being reported by Crane et al. in these proceedings [10]; how a 3D cellular detonation may offer a more robust propagation mechanism remains to be explained, although multiple mechanisms are possible (Kolmogorov cascade only in 3D, differences between 2D and 3D shock dynamics and ensuing reactivity, etc...). Also compatible with the lower limit of $W_c/\lambda \approx 3$ in more irregular mixtures is the role of stochasticity. Since the critical transmission always displays some level of stochasticity [11] inherent from the cellular dynamics and manifested through discrete explosion centers, it is expected that wider channels favour transmission, as the probability of a single re-initiation center across the whole surface of diffracting shock increases proportionally with the channel width. A single remaining explosion center could then *percolate* across the entire front, a scenario suggested to explain analogous results for detonation quenching in non-ideal energetic materials subjected to lateral flow divergence [12].

The resulting anomalous scaling between the critical tube diameter and channel width $d_c/W_c$ has been recognized as a signature of the cellular structure and local stochasticity. It is expected to be 2 based on simple geometric arguments relating the radius of curvature of the front and the characteristic scale controlling the diffraction $d_c$ or $W_c$ [7]. The complications accounted above did not permit to warrant conclusive comparisons between experiments and models, except in very regular systems. The present experiments in a 2D geometry address the limits in 2D. We conduct experiments in sufficiently wide channels in order to allow a 3D cellular structure, but sufficiently narrow to prevent the stochasticity associated with very wide channels, which is left for future study.

The prediction of detonation diffraction from first principles, using detailed hydrodynamic simulations, is usually restricted to hydrogen detonations at low pressures, mixtures that are not overly sensitive to gas dynamics perturbations and have a very regular cellular structure [15]. In most other detonations, simulations have been restricted to qualitative observations using model parameters in a global one-step description [16,17], sometimes far removed from the real thermo-kinetic data. These types of simulations also face a plethora of numerical and modelling difficulties, stemming primarily from the necessity to tackle small-scale diffusive phenomena in real detonations [13,18]. For these unstable detonations, the prediction of the critical conditions for diffraction relies on correlations of the type discussed above.

Recently, Nakayama et al. [19] have demonstrated that dynamics of detonations in several mixtures can be approximately described by a unique relation between the detonation speed, $D$, and the mean curvature of the front, $\kappa$. These observations were borne out from experiments of detonation diffraction in curved channels with varying wave curvatures and wave speeds. While possible non-steady effects cannot be ruled out from these experiments, the good collapse of the entire data in terms of $D(\kappa)$ only suggests these be of minor importance. These observations strongly suggest that a Detonation Shock Dynamics approach, developed by Bdzil and Stewart [20] and used in condensed phase detonation engineering applications [21], can be a useful tool for predicting gaseous detonations in complex geometries. In this approach, the dynamics of a cellular front at large scales could be modeled as a collection of individual mean ray tubes containing at least one cell (see Fig. 1). A simple experiment was recently devised by Radulescu and his students to measure the response of a unit cell to a global geometrical effect by using an exponential horn [14,22,23] as to keep the mean curvature of the front $\kappa = \mathrm{d}\ln A/\mathrm{d}x$ constant, yielding the desired empirical shock speed curvature $D(\kappa)$ relation for closure. This method thus permits to unambiguously determine the $D(\kappa)$ curves for a given explosive mixture at a hydrodynamic average scale larger than the cell size, as it automatically takes into consideration the complex cellular dynamics of detonations. It also provides an estimate of the maximum curvature obtainable in quasi-steady state.

Recently, we have shown that the $D(\kappa)$ dependence obtained from the ZND model was found in reasonable agreement with experiment in very regular $H_2/O_2$/Ar detonations. With a shock diffraction model linking the shock curvature on the axis to the channel width $W$, this permitted to reasonably predict the critical diffraction slot width $W$ in these systems [24,25]. While the ZND model is not expected to work in more irregular detonations [23], we wish to determine whether this critical diffraction slot width $W$ can be predicted using the *experimentally* measured maximum curvature in more irregular detonations, for which more non-idealities addressed above are present. We thus report detonation diffraction experiments in a range of mixtures of varying cellular regularity: $C_2H_6/3.5O_2$, $C_2H_4/3O_2$ and $CH_4/2O_2$. These experiments are performed at conditions such that the cellular structure is 3D, i.e., $L > \lambda$ but sufficiently narrow as to not encounter substantial stochasticity in the third dimension. The critical conditions for diffraction are then compared with the model formulated recently by Radulescu et al. [24], using the $D(\kappa)$ limiting conditions obtained experimentally by Xiao and Radulescu [23]. The model prediction is extended also to other mixtures where experimental maximum front curvature is available [14,19,22].

## 2. Experiments

### 2.1. Experimental details

Experiments were conducted in a 3.4-m-long thin aluminum channel with an internal cross-section height and width of 0.203 m and 0.019 m, respectively. The schematic illustrating the experimental set-up is shown in Fig. 2. The rectangular shock tube comprises three parts, i.e., the detonation initiation section, the propagation section, and the glass-equipped test section for visualization purposes, as detailed elsewhere [14]. The premixed combustible mixture was ignited in the first part by a capacitor discharge. Inserted mesh wires ensured a detonation was formed in the first section of the tube. Subsequently, detonations travelled in the second propagation part and then entered the third test section. For the present diffraction experiments, a rectangular polyvinyl-chloride plate of 0.683 m in length was placed at the start of the test section. The height of the plate block was 0.165 m, such that the opening height permitting detonations to propagate was 0.038 m, which is twice of the channel width and less than 1/5 of the channel height. Once exiting the reduced opening section, detonations diffracted around the sharp corner into the much larger cross-section area. The diffraction process was then visualized by utilizing the classical Z-type schlieren technique with the Phantom v1210 camera at 77,108 frames per second (about 12.9 $\mu s$ for each interval). The schlieren visualization was implemented with a vertical knife edge utilizing a light source of 360 W, with the exposure time set to 0.44 $\mu$s and the frame resolution kept at $384 \times 288$ px$^2$. Five 113B27 and three 113B24 piezoelectric PCB pressure sensors were mounted on the top wall of the shock tube for recording pressure signals. The set-up is identical to our previously reported diffraction experiments in $H_2/O_2$/Ar detonations [15].

Three different hydrocarbon-oxygen mixtures were tested, stoichiometric ethane-oxygen ($C_2H_6/3.5O_2$), ethylene-oxygen ($C_2H_4/3O_2$) and methane-oxygen ($CH_4/2O_2$). Detonations in these mixtures have an irregular cellular structure. The characteristic structure of these detonations and the dependence of detonation speed on front curvature have been measured in these mixtures by Xiao and Radulescu [14]. Each mixture was prepared in a separate mixing tank by the method of partial pressures and was then left to mix for more than 24 hours. Once the shock tube was evacuated below the absolute pressure of 80 Pa in every single experiment, the mixture was then introduced into the shock tube through both ends of the channel at

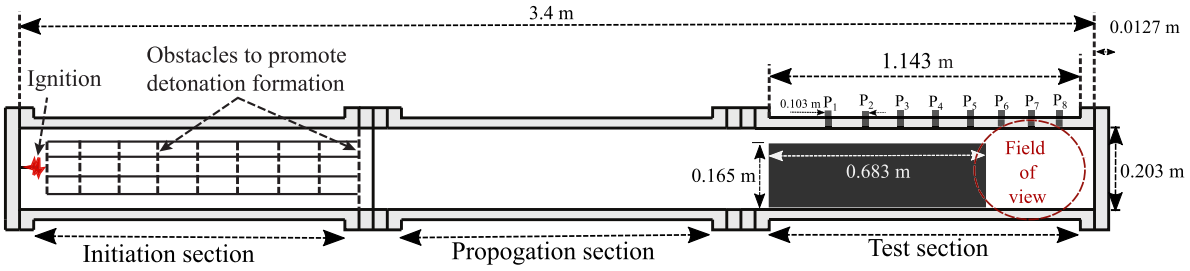


Fig. 2. Schematic of the shock tube used in the diffraction experiments.

the desired initial pressure. The initial pressure was varied in order to control the mixture sensitivity and identify the critical conditions for diffraction.

We report the critical diffraction condition in terms of the channel height $W$ normalized with the either $\Delta_i$, the ZND induction zone length or by the cell size $\lambda$. The induction zone length was calculated using an in-house ZND code [13] and the San Diego chemical mechanism. Corrections for the velocity deficits were incorporated in the calculations by using the experimentally determined detonation velocity. The cell size for each mixture was taken from the Detonation Database [26], fitted to the relation $\lambda = Ap_0^{-B}$, where the fitting parameters A and B for each mixture are presented in table 4 of Xiao and Radulescu [23].

### 2.2. Results

Typical examples of the different flow fields obtained near the critical diffraction conditions are shown in Fig. 4. For all experiments, we evaluated the top-wall mean propagation speed of detonations, before being impacted by the penetration of failure waves, to be in the range of 0.97∼0.99 $D_{CJ}$, which is very close to the ideal Chapman-Jouguet (CJ) detonation speed (2223 m/s for ethylene, 2250 m/s for ethane and 2330 m/s for methane mixtures). It thus suggests that detonations before diffraction can be reasonably assumed to be ideal and losses to the transparent walls are small.

Fig. 4a shows the unsuccessful transmission of a detonation in $C_2H_4/3O_2$. Multiple frames are shown superimposed in the same image. The detonation originating in the channel of dimension $W/2 = 38$ mm, where $W$ is the typical bi-diffraction channel height, is clearly evident to have a cellular structure. The cellular structure starts being affected by the expansion wave originating from the corner in the fourth frame. Since the schlieren photographs record density gradients, the demarcation between burned and shocked but non-burned gases is very clear. This reaction zone is seen to systematically fall behind the lead shock. In this experiment, the lead shock continuously decays to low speeds and the detonation is quenched by the diffraction process.

The details of the critical diffraction in a more sensitive mixture obtained at a slightly higher pressure are shown in Fig. 4b. At these critical conditions, the detonation wave remains coupled near the top wall. The cellular structure, although enlarged, remains. In the region below approximately the corner level, the detonation decouples as for the subcritical case discussed above. The reformation of a detonation wave proceeds from the growth of a kernel originating near the axis, although the generally irregular structure does not permit to identify the location and mechanism. Very similar sequence of events have recently been reported in more regular $H_2/O_2$/Ar detonations [24,27,28]. In these studies, new detonation heads were preferentially observed slightly off-axis. Our results show that although the establishment of the detonations with the smallest cells are slightly off-axis, the front near the axis (top wall in our experiments) never fails for successful experiments.

A similar sequence of events were also observed in $C_2H_6/3.5O_2$ mixture. Two typical front evolution records bracketing the critical conditions for transmission are shown in Figs. 4c and d. The cellular structure in this mixture is more irregular. This is compatible with stability considerations, reflected by the instability parameter, $\chi = (t_i/t_r)(E_a/RT_{VN})$ [29], the product of the ratio of induction and reaction time and the temperature sensitivity of the induction zone. For the mixtures tested, $\chi$ takes the value of 17, 45 and 480 for the ethylene, ethane and methane mixtures respectively [23].

The experiments performed in the less sensitive mixture of $CH_4/2O_2$ were not able to produce a successful transmission until $p_0 = 30$ kPa. However, we only visualized the detonation for subcritical pressures below 26 kPa for safety reasons. For higher pressures, we used aluminum side plates instead of glass. The successful/unsuccessful transmission of detonation diffraction was identified using pressure transducers. In these experiments, the rectangular obstacle inside the shock tube was moved back 0.8 m to have 7 pressure transducers while the diffraction is occurring. The highest pressure tested for successful transmission was 38 kPa. Two typical sub-critical detonation diffraction events are shown in Figs. 4e and f. In the lower pressure experiment of Fig. 4e, the decoupling of

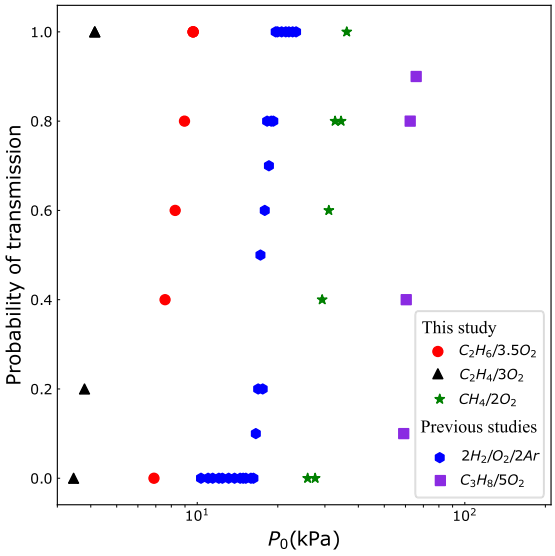


Fig. 3. Probability of successful transmission of a detonation as a function of initial pressure. The $2H_2/O_2/2Ar$ data are from 2D diffraction experiments reported in [15] and $C_3H_8/5O_2$ are 3D diffraction experiments reported in [11]. Diffraction experiments of hydrogen and propane mixtures were repeated 10 times at each pressure.

the reaction zone from the diffracting lead shock is clearly evident. The saw-tooth shape of the reaction contour is the vestigial structure of the original cellular structure. At the highest pressure where visualization was possible, shown in Fig. 4f, although the detonation eventually fails, a complex filamentous structure is observed.

Near criticality, repeated experiments showed that both transmission and failure were observed over a particular range. Repeated experiments were performed at each pressure tested and a probability for transmission was established. Fig. 3 provides the probability of detonation transmission for the mixtures tested, along with previous data obtained in previous studies. The critical pressures for transmission are $8.3 \pm 1.4$ kPa for $C_2H_6/3.5O_2$, $3.7 \pm 0.3$ kPa for $C_2H_4/3O_2$ and $32 \pm 4$ kPa for $CH_4/2O_2$ mixtures. The range of pressures in which both success and failure are possible represents approximately 34%, 17% and 25% of the critical pressures recorded for $C_2H_6/3.5O_2$, $C_2H_4/3O_2$ and $CH_4/2O_2$ mixtures, respectively. The large spread in critical conditions for transmission is in good agreement with the results measured by Loiseau and Higgins [11] for propane-oxygen detonations diffraction in tubes (ranges over 6.7 kPa). Their apparatus consists of a 1.8-m-long tube with a 5-cm-internal-diameter followed by a 40-cm-long cylindrical test chamber with a 19-cm-internal-diameter. The critical pressures of detonation diffraction experiments in $2H_2/O_2/2Ar$ mixture spread over 3 kPa as shown in Fig. 3. These experiments were reported by Mevel et al. [15] and obtained in the same narrow channel used in this study.

Table 1
Critical diffraction conditions obtained experimentally.

| Mixture | $P_0$ (kPa) | $W_c/\Delta_i$ | $W_c/\lambda$ | $L/\lambda$ |
|---|---|---|---|---|
| $C_2H_6/3.5O_2$ | 8.3±1.4 | 170±28 | 3.5±0.6 | $\simeq 1.1$ |
| $C_2H_4/3O_2$ | 3.7±0.3 | 150±13 | 3.8±0.3 | $\simeq 1.0$ |
| $CH_4/2O_2$ | 32±4 | 51±7 | 6.9± 0.9 | $\simeq 1.7$ |

It is more convenient to present the critical diffraction condition in terms of the channel height $W$ normalized with either $\Delta_i$, the ZND induction zone length or by the cell size $\lambda$. The resulting critical $W_c/\Delta_i$ and $W_c/\lambda$ are given in Table 1. Also provided is an estimate of the number of cells across the channel thickness close to the limit, given by $L/\lambda$. In the methane experiments, $L/\lambda > 1$, while approaching unity in the other mixtures. This suggests that the methane experiments approached the desired 3D cellular structure, while the other mixtures may have been somewhat affected by wall effects. Interestingly, the limit observed in the methane system was precisely half of the $d_c/\lambda = 13$ correlation for tubes as expected from simple geometrical scaling based on wave curvature, while somewhat lower in the other two mixtures. We have not pursued further investigation into these differences, given that cell-size data are usually accurate to within a factor of 2.

## 3. Predicted critical slot height $W_c$ from experimental $D(\kappa)$ data

As explained in the introduction, we wish to test the prediction of critical diffraction slot height using experimental $D(\kappa)$ data. Nakayama et al. [19] reported that $D(\kappa)$ data for $C_2H_4/3O_2$, the same mixture as tested in the present study, was characterized by a maximum curvature of $\kappa\lambda \simeq 0.11$, which was found similar to the value in $2H_2/O_2$ and $2C_2H_2/5O_2/7Ar$. Xiao and Radulescu [23] determined the $D(\kappa)$ data and the maximum curvature in the mixtures tested in the present study, normalized by the induction zone length. These data can readily be used to predict the detonation diffraction critical slot width provided a link is found expressing the relation between the slot width $W$ and the maximum frontal curvature of the front. This link is provided by the study of the subcritical shock diffraction recently formulated by Radulescu et al. [24]. Since the diffraction of the detonation leads to de-coupling of the reaction zone from the lead shock except for a kernel near the top wall, the curvature at critical conditions is expected to be the curvature imposed by the decoupled shock. This de-coupled shock evolves as an inert shock. The problem is approximately self-similar.

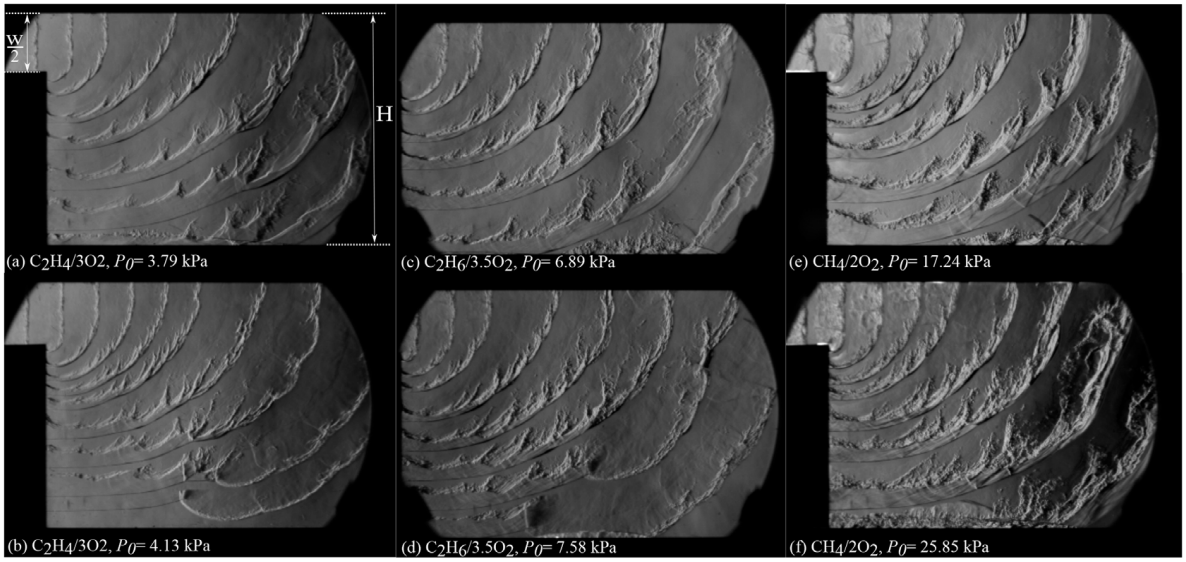


Fig. 4. Composite schlieren images of detonation diffraction in the three mixtures tested at initial temperature 295 K and varying pressures; the distances $H$ and $W/2$ indicated in (a) are 203 mm and 38 mm, respectively. Video animations are provided as supplemental material illustrating the detailed evolution process.

### 3.1. The curvature imposed by the decoupled shock

In essence, the self-similar shock diffraction can be found in closed form using Whitham's geometrical shock dynamics method [30], provided closure of the exponent $n$ describing the local dynamics of the shock is available [24]. The exponent $n$ links the shock speed $D$, its deceleration $\dot{D}$ and its curvature $\kappa$:

$$n \equiv -\frac{D^2\kappa}{\dot{D}} \tag{1}$$

The maximum curvature occurs when a transverse signal along the shock reaches the axis of symmetry. Considering the half height of the bi-diffraction channel is $W/2$, Whitham's geometric shock dynamics yields the following relation between the maximum curvature and the channel height [24]:

$$W_c = \frac{2}{\kappa}\left(\frac{\sqrt{n}}{n+1}\right) \tag{2}$$

The exponent $n$ can be modeled with different closures, Whitham's characteristic rule [30], Westcott's reactive model [31] and Radulescu's weakly support shock hypothesis, the latter being found to provide the best agreement in the tests of hydrogen detonations [24]. We thus wish to test how these closures perform for predicting the dynamics of the decoupled shocks in the current experiments of diffracting detonations.

In the limit of a strong shock, Whitham's well known characteristic rule [30] gives

$$n = 1 + \frac{2}{\gamma} + \sqrt{\frac{2\gamma}{\gamma - 1}} \tag{3}$$

Table 2
Summary of the modelling exponent $n$. VN refers to the von Neumann state.

| Mixture | $P_0$ (kPa) | $\gamma_{VN}$ | $n_R$ | $n_W$ | $n_{WSB}$ |
|---|---|---|---|---|---|
| $C_2H_6/3.5O_2$ | 8.3±1.4 | 1.15 | 3.74 | 6.64 | 5.60 |
| $C_2H_4/3O_2$ | 3.7±0.3 | 1.17 | 3.71 | 6.42 | 5.56 |
| $CH_4/2O_2$ | 32±4 | 1.17 | 3.71 | 6.43 | 5.56 |

where $\gamma$ is the ratio of specific heats, assumed constant in the model. In this model, the rear boundary conditions have an insignificant influence on the shock dynamics. Note that the strong shock assumption is relevant to our study, as the Mach number of detonations is approximately 7.

Wescott, Stewart and Bdzil [31] assumed the detonation in a quasi-steady state with an embedded sonic surface. The exponent $n$ was found to be:

$$n = 3\frac{\gamma + 1}{\gamma} \tag{4}$$

Radulescu et al. [24] proposed a weakly supported shock model in which $(1/\dot{D})\partial u/\partial t \ll 1$. This yielded $n$:

$$n = 2\frac{\gamma + 1}{\gamma} \tag{5}$$

The resulting value of modeling exponent $n$ from the three models (weak support (R), Whitham (W) and Wescott, Stewart and Bdzil (WSB) are shown in Table 2, for the critical pressures of diffraction experiments. The ratio of specific heat was evaluated behind the shock.

The performance of the three models discussed above in predicting the shock evolution is shown

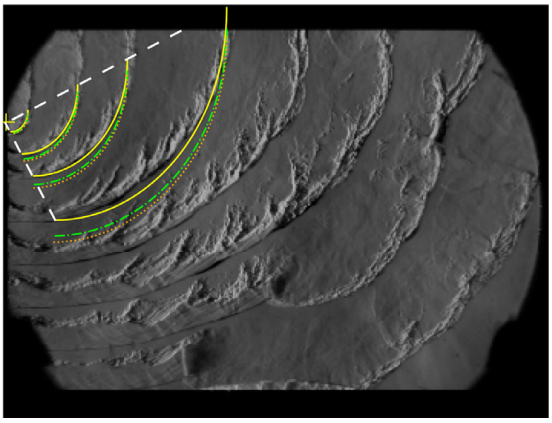

Fig. 5. Composite schlieren images of detonation diffraction in the critical diffraction of $C_2H_6/3.5O_2$ mixture at initial temperature and pressure 295K and 7.58 kPa.

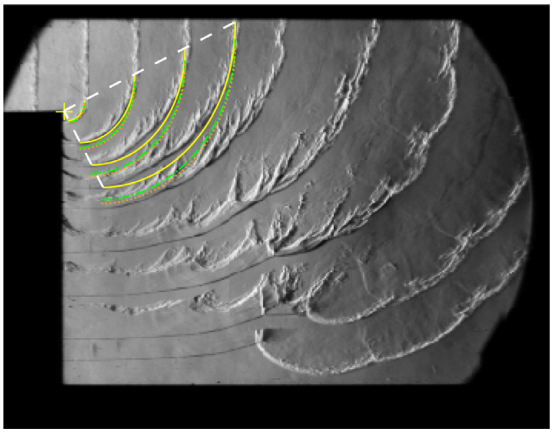

Fig. 6. Composite schlieren images of detonation diffraction in the critical diffraction of $C_2H_4/3O_2$ mixture at initial temperature and pressure 295K and 4.13 kPa.

in Figs. 5, 6 and 7 for critically transmitted detonations in $C_2H_6/3.5O_2$, $C_2H_4/3O_2$ and $CH_4/2O_2$. In a coordinate system centered at the corner, the shock shape is given by Whitham's self-similar solution:

$$\frac{X}{D_{CJ}t} = \sqrt{\frac{n+1}{n}} \exp\left(\frac{\theta}{\sqrt{n}}\right) \sin(\eta - \theta) \tag{6}$$

$$\frac{Y}{D_{CJ}t} = \sqrt{\frac{n+1}{n}} \exp\left(\frac{\theta}{\sqrt{n}}\right) \cos(\eta - \theta) \tag{7}$$

where $\eta$ is given by $\tan\eta = \sqrt{n}$ and $\theta$ is the angle of the unit normal to the shock surface with the $x$-axis. In all the figures, the solid yellow lines correspond to the weakly supported shock model, the dash-dotted green lines to the WSB model, and the dotted orange lines to Whitham's inert shock model, at the sequential frames of experiments. The dashed white lines are the characteristic lines which show the propagation of the signal from the corner for

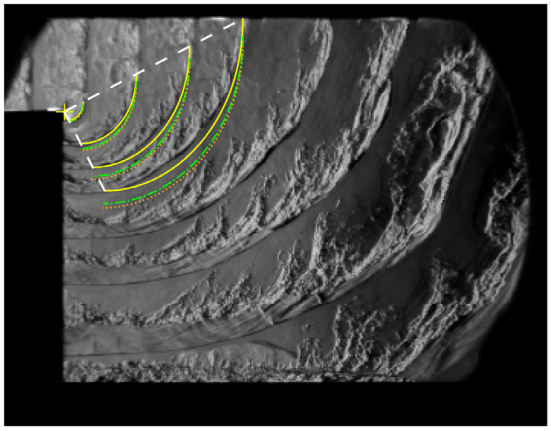

Fig. 7. Composite schlieren images of detonation diffraction in sub-critical diffraction of $CH_4/2O_2$ mixture at initial temperature and pressure 295K and 25.85 kPa.

the weakly supported shock model of Radulescu. Accordingly, the region where the model is valid is between the indicated characteristic lines.

In all of the diffraction experiments, the weakly supported self-similar model is predicting the curvature of the diffracted shock very well from early to later times of diffraction with maximum error of curvature 20% for $C_2H_6/3.5O_2$ and $CH_4/2O_2$, and 15% for $C_2H_4/3O_2$ mixtures. These results show that the shock support model of Radulescu offers an improvement over the other two models, which under-estimate somewhat the shock wave curvature.

### 3.2. Prediction of critical channel height

Given the good agreement of the weakly supported model to predict the shock wave evolution, we substituted the value of $n$ provided by Eq. (5) in Eq. (2) to close the model for the critical channel height for successful detonation diffraction, in terms of the maximum curvature. This can also be re-written as:

$$\frac{W_c}{\Delta_i} = 2\frac{\sqrt{n}}{(n+1)\kappa\Delta_i} \tag{8}$$

The maximum curvature required for closure is obtained from the $D/D_{CJ} = f(\kappa\Delta_i)$ empirical data measured by Xiao and Radulescu in the exponentially diverging ramp in the mixtures tested in the present study. These data are reproduced in Fig. 8 [23]. Their results show a good scaling of detonation deficit with the non-dimensional curvature $\kappa\Delta_i$. With increasing curvature, the detonation is slower and there is a maximum curvature that can sustain a steadily propagating cellular detonation. We use this maximum curvature $\kappa\Delta_i$, which is in the range of 0.0047-0.0054 for $C_2H_6/3.5O_2$, 0.0067-0.0093 for $C_2H_4/3O_2$ and 0.0185-0.027 for $CH_4/2O_2$. The uncertainty ranges are shown as vertical dashed lines in Fig. 8. These provided $D-\kappa$

Table 3
Summary of diffraction experiments and models prediction. Exp: Experiment, R: Radulescu (weakly supported shock model), WSB: Wescott, Bdzil and Stewart's model and W: Witham's model.

| Mixture | $W_c/\Delta_i$, Exp | $W_c/\Delta_i$, Model, R | $W_c/\Delta_i$,WSB | $W_c/\Delta_i$, W | $W_c/\Delta_i$, ZND |
|---|---|---|---|---|---|
| $C_2H_6/3.5O_2$ | 170±28 | 161±12 | 141±9 | 133±9 | 593 |
| $C_2H_4/3O_2$ | 150±13 | 102±15 | 89±12 | 85±12 | 300 |
| $CH_4/2O_2$ | 51±7 | 36± 6 | 31±5 | 30±5 | 767 |

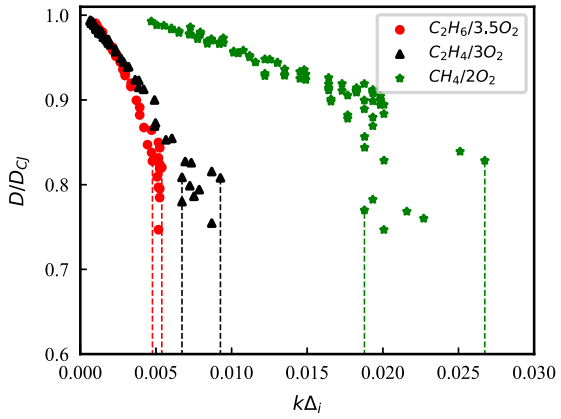


Fig. 8. The non-dimensional $D-\kappa$ characteristic relationships obtained experimentally, adapted from [23].

data for cellular detonations near failure shown in Fig. 8 have certainly a measure of stochasticity which is linked with the presence of fluctuations and requires a stochastic approach with very large datasets. Future work needs to establish whether this stochasticity in the $D-\kappa$ limits is sufficient to infer the diffraction stochasticity or not.

The critical values obtained for the $W_c/\Delta_i$ using Eq. (8) and the data for the maximum curvatures outlined above, along with their confidence levels based, are tabulated in Table 3. The ratio of specific heats required were calculated at the Von Neumann state for each mixture at the critical diffraction conditions. These predicted values of $W_c/\Delta_i$ can now be compared with the experimental values. Note that the results were corrected to account for the slight lengthening of the induction zone length due to the losses by accounting for the velocity deficits.

The predictions for critical slot width $W_c$ tabulated in Table 3 are in general good agreement with the experimental value. Among the predictions made with different exponents $n$, the model of Radulescu provides the closest agreement with experiment. For the $C_2H_6$ mixture, the prediction is in excellent agreement with the experiment with less than 5% discrepancy. For the $C_2H_4$ and $CH_4$ mixtures, the model under-predicts the experimental limit by 32% and 38% respectively. When considering the uncertaities due to the noted stochasticities, the agreement is in fact much better. We can thus conclude that the model is successful in predicting the critical failure conditions. The paradigm tested, mainly, can the diffraction of cellular detonations be predicted by a $D(\kappa)$ law for a unit cell, is thus successful.

It is also of interest to test the predictability of the detonation limits using the maximum curvature predicted by the ZND model, as opposed to the experimental value. This is provided in last column of Table 3, obtained from Eq. 14 in [24]. As expected, this model significantly over-predicts the limits, by more than an order of magnitude for the methane system, as expected from our previous work [23]. This highlights again the need to construct a model for detonations that takes into account the cellular processes and how they enhance the propagation mechanism.

### 3.3. Failure prediction using other experimentally measured $D-\kappa$ data

Nakayama et al. [19] reported that the $D(\kappa)$ curves for stable detonation propagation in $C_2H_4/3O_2$, $2H_2/O_2$ and $2C_2H_2/5O_2/7Ar$ were identical when scaled with the cell size. The maximum curvature of $\kappa\lambda \simeq 0.11$ was found. Re-writing Eq. (8) normalized by the cell size as:

$$\frac{W_c}{\lambda} = 2\frac{\sqrt{n}}{(n+1)\kappa\lambda} \tag{9}$$

and using the exponent $n$ of 3.71, it yields a critical slot width of $W_c/\lambda \approx 7$. This value is slightly over-predicting the limits found in the current study, in the range of 3-7. Given that Nakayama et al. only report stable propagation, i.e., devoid of the typical non-steadiness observed near the limits, it means that the real maximum curvature is somewhat larger and the limit $W_c/\lambda$ is smaller than 7. Nevertheless, the limit reported by them is also compatible with the diffraction in tubes, where one would expect that $d_c/\lambda$ to be twice as for channels. This further supports the idea that critical diffraction of cellular detonations can be predicted by $D(\kappa)$ data for cellular detonations.

Datasets for $D(\kappa)$ were obtained in other mixtures by Radulescu and Borzou [22] and Xiao and Radulescu [14] in mixtures of $C_3H_8/5O_2$, $2C_2H_2/5O_2/21Ar$, $2H_2/O_2/2Ar$, $2H_2/O_2/3Ar$ and $2H_2/O_2/7Ar$ using the exponential horn technique. Xiao and Radulescu [23] reduced these data in terms of $\kappa\lambda$ (figure 18 in their paper). The limiting value of curvature was found to be in the range of 0.2 to 0.6, the larger values for more regular

$H_2/O_2$/Ar system. This yields, according to Eq. (9), limiting diffraction values of 2 to 4. This agrees well with the experimental value of 3 to 6 for the more irregular detonations but underpredicts the limits generally accepted for more regular detonations. Empirically, it thus appears that the DSD treatment of cellular detonations, whereby diffraction can be predicted by experimentally measured $D(\kappa)$ datasets work better for more irregular systems.

At this point, we can only speculate why a quasi-steady $D(\kappa)$ response is more adequate for irregular detonations, based on the physics of the propagation of regular and irregular detonations. Regular detonations behave similarly to laminar ZND-detonations where the ignition mechanism is by adiabatic compression. As the limits are approached, non-steady effects can no longer be neglected and the structure no longer responds as in quasi-steady state. On the other hand, the ignition mechanism of irregular detonations is by a combination of adiabatic compression near the front and diffusion assisted burning of pockets at the later stages. The latter does not have the strong coupling to non-steady gasdynamic effects, and a more quasi-steady response is expected. Since the thin front responds much faster than the thick main reaction zone, one would expect the entire structure to remain in quasi-steady state on the longer time scales associated with the entire reaction zone structure. Empirically, we also find that the quasi-steady prediction to work better for irregular mixtures, where this particular reaction structure is more prevalent. Clearly, however, these transient effects need to be carefully studied in the future for cellular detonations. It is expected that these transient effects influence not only the limits in diffraction phenomena but also the methods of measurement of the steady responses to begin with, where entrance effects need to be carefully evaluated.

## 4. Closing remarks

In the present study, we have showed that the critical diffraction of irregular detonations can be very well predicted from an experimentally determined $D(\kappa)$ law. The prediction error of less than 5% was observed for $C_2H_6/3.5O_2$, while the limits were underpredicted by 32% for $C_2H_4/3O_2$, and 38% for $CH_4/2O_2$ mixtures. Given the inherent stochasticity near failure in the diffraction experiments and available $D(\kappa)$ of approximately 20 to 30% for each, the agreement is actually much better.

This generally good agreement supports the view that the detonation diffraction critical conditions are associated with a maximum rate of frontal stretch, or curvature [31,32]. More generally, the present study suggests that the physics of propagating detonations can be encapsulated in the problem of a single unit cell propagating in a diverging ray tube. It highlights the necessity for models to be developed for this canonical problem, that account for cellular instabilities.

## Declaration of Competing Interest

The authors declare that they have no known competing financial interests or personal relationships that could have appeared to influence the work reported in this paper.

## Acknowledgments

M.I. Radulescu acknowledges the financial support provided by the Natural Sciences and Engineering Research Council of Canada (NSERC) through the Discovery Grant “Predictability of detonation wave dynamics in gases: experiment and model development”.

## Supplementary material

Supplementary material associated with this article can be found in the online version. Supplementary material associated with this article can be found, in the online version, at doi:10.1016/j.proci.2022.11.004.

## References

[1] J.H.S. Lee, Dynamic parameters of gaseous detonations, Annu. Rev. Fluid Mech. 16 (1) (1984) 311–336.
[2] J. Lee, The detonation phenomenon, Cambridge University Press, 2008.
[3] I. Moen, A. Sulmistras, G. Thomas, D. Bjerketvedt, P. Thibault, Influence of cellular regularity on the behavior of gaseous detonations, Dyn. Explos. (1986) 220–243.
[4] G. Thomas, D. Edwards, J. Lee, R. Knystautas, I. Moen, Y. Wei, Dynamics of Explosions, vol. 106, AIAA, 1986, pp. 144–154.
[5] W. Benedick, R. Knystautas, J.H. Lee, Large-scale experiments on the transmission of fuel-air detonations from two-dimensional channels, Am. Inst. Aeronautic. Astronautic. (1983).
[6] J. Meredith, H.D. Ng, J.H. Lee, Detonation diffraction from an annular channel, Shock Waves 20 (6) (2010) 449–455.
[7] Y. Liu, J. Lee, R. Knystautas, Effect of geometry on the transmission of detonation through an orifice, Combust. Flame 56 (2) (1984) 215–225.
[8] V. Mitrofanov, R. Soloukhin, The multifront detonation diffraction, Dokl. Akad. Nauk SSSR 159 (5) (1964) 1003–1006.
[9] D. Edwards, G. Thomas, M. Nettleton, The diffraction of a planar detonation wave at an abrupt area change, J. Fluid Mech. 95 (1) (1979) 79–96.
[10] J. Crane, J. Lipkowicz, X. Shi, I. Wlokas, A. Kempf, H. Wang, Three-dimensional detonation structure

and its response to confinement, Proc. Combust. Inst. 39 (2022) inpress.
[11] J. Loiseau, A.J. Higgins, Statistical measurement of critical tube diameter(2007).
[12] A. Higgins, Measurement of detonation velocity for a nonidead heterogeneous explosive in axisymmetric and two dimensional geometries, AIP Conf. Proc. 1195 (1) (2009) 193–196.
[13] M.I. Radulescu, A detonation paradox: why inviscid detonation simulations predict the incorrect trend for the role of instability in gaseous cellular detonations? Combust. Flame 195 (2018) 151–162.
[14] Q. Xiao, M.I. Radulescu, Dynamics of hydrogen–oxygen–argon cellular detonations with a constant mean lateral strain rate, Combust. Flame 215 (2020) 437–457.
[15] R. Mevel, Q. Xiao, S. Gallier, M.I. Radulescu, Hydrogen-oxygen-argon detonation diffraction in a narrow channel, Proc. Twenty-six ICDERS, Boston (2017).
[16] M. Arienti, J. Shepherd, A numerical study of detonation diffraction, J. Fluid Mech. 529 (2005) 117–146.
[17] L. Shi, K.C.K. Uy, C.Y. Wen, The re-initiation mechanism of detonation diffraction in a weakly unstable gaseous mixture, J. Fluid Mech. 895 (2020).
[18] M.I. Radulescu, C.K. Law, The transient start of supersonic jets, J. Fluid Mech. 578 (2007) 331–369.
[19] H. Nakayama, J. Kasahara, A. Matsuo, I. Funaki, Front shock behavior of stable curved detonation waves in rectangular-cross-section curved channels, Proc. Combust. Inst. 34 (2) (2013) 1939–1947.
[20] J.B. Bdzil, D.S. Stewart, Modeling two-dimensional detonations with detonation shock dynamics, Phys. Fluid A 1 (7) (1989) 1261–1267.
[21] D.E. Lambert, D.S. Stewart, S. Yoo, B.L. Wescott, Experimental validation of detonation shock dynamics in condensed explosives, J. Fluid Mech. 546 (2006) 227–253.
[22] M.I. Radulescu, B. Borzou, Dynamics of detonations with a constant mean flow divergence, J. Fluid Mech. 845 (2018) 346–377.
[23] Q. Xiao, M.I. Radulescu, Role of instability on the limits of laterally strained detonation waves, Combust. Flame 220 (2020) 410–428.
[24] M.I. Radulescu, R. Mevel, Q. Xiao, S. Gallier, On the self-similarity of diffracting gaseous detonations and the critical channel width problem, Phys. Fluids 33 (2021) 066106.
[25] Q. Xiao, R. Mével, S. Gallier, M.I. Radulescu, Ray–tracking methods for characterizing the dynamics of curved detonation, Phys. Fluids 34 (6) (2022) 066104.
[26] M. Kaneshige, J.E. Shepherd, Detonation database (1997).
[27] S. Gallier, F. Le Palud, F. Pintgen, R. Mével, J. Shepherd, Detonation wave diffraction in $h_2$-$o_2$-ar mixtures, Proc. Combust. Inst. 36 (2) (2017) 2781–2789.
[28] F. Pintgen, J. Shepherd, Detonation diffraction in gases, Combust. Flame 156 (3) (2009) 665–677.
[29] M.I. Radulescu, The propagation and failure mechanism of gaseous detonations: Experiments in porous-walled tubes, McGill University, Ph.D. thesis, 2003.
[30] G.B. Whitham, Linear and nonlinear waves, volume 42, John Wiley & Sons, 2011.
[31] B. Wescott, D.S. Stewart, J. Bdzil, On self-similarity of detonation diffraction, Phys. Fluids 16 (2) (2004) 373–384.
[32] J. Lee, Dynamics of Exothermicity, Gordon and Breech, 1996, pp. 321–336.

# Chapter 3

# The critical conditions for the re-ignition and detonation formation from Mach reflections of curved decaying shocks

In this chapter, we identify the conditions governing the transition between large-scale and small-scale structures and isolate the process of detonation formation under strong transient effects. A canonical experimental set-up is designed to reliably generate two decaying shock waves, whose interaction results in the formation of a Mach shock. This setup allows for the quantification of the Mach shock dynamics on a global scale and enables the investigation of its effects.

This study was published in *Proceedings of the Combustion Institute*, in 2024 and is included in the following pages of this thesis. The author conducted the experiments, performed the analysis, and wrote the paper. The conceptual planning and paper editing was done in collaboration with the PhD supervisor, Prof. M. I. Radulescu.

Proceedings of the Combustion Institute 40 (2024) 105774

Contents lists available at ScienceDirect

Proceedings of the Combustion Institute

journal homepage: www.elsevier.com/locate/proci

# The critical conditions for the re-ignition and detonation formation from Mach reflections of curved decaying shocks

Farzane Zangene *, Matei I. Radulescu

*Department of Mechanical Engineering, University of Ottawa, Ottawa, ON K1N6N5, Canada*

ARTICLE INFO

*Keywords:*
Detonation formation
Shocks reflection
Decay rate model
Weakly non-steady curved detonations

ABSTRACT

The objective of this study is to determine the critical conditions for a detonation wave formation following a Mach reflection of two incident shocks. This problem is central to the propagation mechanism of cellular detonations, where such periodic reflections occur continuously. A new experimental technique is introduced that permits the isolation of this Mach reflection. The technique is inspired by that of White (1963) and uses a detonation passing through a bifurcated converging–diverging nozzle to reproducibly generate the desired shock reflection at its exit, where the two transmitted mis-aligned incident shocks interact. The collision process was monitored with high-speed schlieren videos permitting to measure the strength, decay rate and curvatures of the incident and Mach waves. The experiments were performed in mixtures of $CH_4/2O_2$ and $2H_2/O_2/2Ar$, which span the degree of cellular regularity of detonations in reactive gases. Three distinct regimes of transmission were identified: detonation formation, decaying Mach shock followed by a flame, and inert Mach shock with no re-ignition. For both mixtures, the condition separating the re-ignition and no re-ignition was very well predicted by the critical decay rate ignition theory of Eckett et al. On the other hand, the transition between detonation formation and ignition was found to correlate much better with the critical curvature concept of quasi-steady curved detonations of Kasimov and Stewart. Both experiments in the regular and irregular mixtures were found in excellent agreement with this criterion, established on the basis of experimental velocity–curvature data available in the literature for these mixtures. For the hydrogen detonations, this criterion was also in agreement with the critical curvature predicted by the ZND theory. For the methane detonations, order of magnitude disagreement was observed with the ZND model prediction, further confirming the propensity of irregular cellular detonations to propagate under higher curvatures than predicted by laminar detonation theory.

## 1. Introduction

It is well known that all self-sustaining detonations in gases have a three-dimensional cellular structure [1]. These interactions are believed to control the propagation mechanism of detonations, as they periodically generate highly overdriven detonations well above the Chapman–Jouguet (CJ) speed, which then decay through the cycle and reform from new triple point collisions [2]. In the propagation of detonation waves, especially in the vicinity of marginal propagation conditions within the detonation cell, various outcomes can occur following the collision of two triple points. In some cases, a local detonation wave is generated, where the Mach shock couples with the reaction wave behind it, displaying a fine cellular structure. In other instances, the shock ignites the gas but continues to decay, failing to form a detonation. Finally, in some scenarios, minimal exothermicity occurs behind the newly formed Mach shock, leaving the majority of the gas unreacted. This unreacted gas subsequently combusts within a turbulent flame [3,4].

Previous attempts at identifying a canonical configuration to study this phenomenon have yielded limited success. In situ study of Mach reflections in detonations is difficult owing to the small scale and stochasticity of the phenomenon. Attempts to generate reproducible Mach reflections in the wakes of obstacles placed in the path of detonations have also yielded limited success, due to the presence of both regular and Mach reflections in the same experiment [5]. In the present study, we formulate a novel configuration to isolate this Mach reflection. The technique is inspired by that of White [6] and uses a detonation passing through a bifurcated converging–diverging nozzle to reproducibly generate the desired shock reflection at its exit, where the two transmitted mis-aligned incident shocks interact. We report experiments using this technique. We observe three distinct regimes

* Corresponding author.
*E-mail address:* fzang055@uottawa.ca (F. Zangene).

https://doi.org/10.1016/j.proci.2024.105774
Received 4 December 2023; Accepted 10 September 2024
Available online 17 October 2024

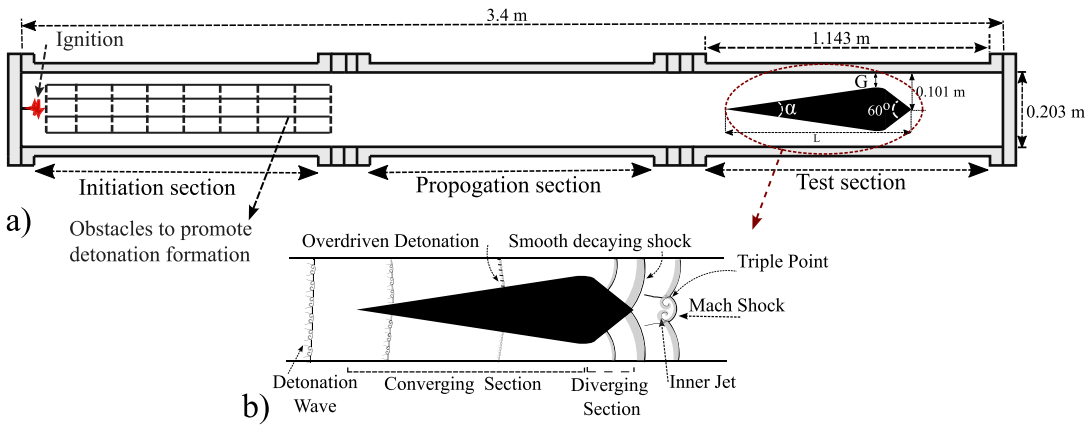


**Fig. 1.** The schematic of the experimental apparatus. The angle $\alpha$ is set to either 15° for $G$ values of 0.0265 m and 0.0132 m, or 20° for a $G$ value of 0.0065 m. The length of the object $L$ is 0.706 m, 0.828 m, and 0.7 m for gap heights of 0.0065 m, 0.0132 m, and 0.0265 m, respectively.

**Table 1**
The experimental test gases and their properties.

| Mixture | $p_0$ [kPa] | $\gamma_{VN}$ | $\chi$ |
|---|---|---|---|
| $CH_4/2O_2$ | 15 | 1.17 | 510 |
| $2H_2/O_2/2Ar$ | 15 | 1.4 | 3.7 |

of transmission: Mach reflection without re-ignition, Mach reflection with re-ignition and Mach reflection with the generation of coupled detonation waves generating a fine-scale transverse wave structure.

The conditions separating the various regimes of transmission are discussed in terms of two conceptual models: the critical expansion model for gas ignition [7–11] and the critical sustenance criteria of weakly curved and weakly non-steady detonations anticipated in Detonation Shock Dynamics theory [12–14].

## 2. Experiments

### 2.1. Experimental set-up

The experiments were performed in a 3.4-m-long shock tube, with 0.019-m-thickness and 0.203-m-height [15]. The schematic illustrating the experimental set-up is shown in Fig. 1a. A diamond shape object made of aluminum was inserted into the test section to create an inverted converging–diverging nozzle with the top and bottom walls of the shock tube, symmetrically.

The variable $G$ in Fig. 1a represents the gap height prior to the occurrence of detonation diffraction. Three different objects were specifically designed to control the structure of the two decaying shocks through the diffraction process, creating gap heights of 0.0265 m, 0.0132 m and 0.0065 m. The angle of the converging section, denoted by $\alpha$, was chosen to be 15° for the gap heights of 0.0132 m and 0.0265 m, and 20° for the gap height of 0.0065 m. This selection aimed to provide two smooth overdriven detonation waves without any kink on the structure as documented in a separate study [16]. To ensure a smooth transition, the object's throat connecting the converging and diverging channels had a rounded tip with a radius of curvature equal to the gap height. In the diverging section, the detonation is made to recover an idealized quasi-laminar structure of a shock followed by a reaction wave. As sketched in Fig. 1b, the two symmetrical decaying shocks from the top and bottom channels interact at the apex of the diamond and generate a Mach reflection. The angle of the diverging section for each geometry was maintained at 30°. This selection was motivated by the observed tendency of detonation Mach reflections to have a 30° angle of incidence of the incident shocks [9,17].

The propagation and reflection process were visualized using the schlieren technique using 30 cm diameter field mirrors, a high-speed Phantom v1210 camera and a continuous white light source from an incandescent automotive light bulb. The inter-frame times were 13.6 μs and 12.9 μs for resolutions of 384 × 304 px$^2$ and 384 × 288 px$^2$, respectively. The two mixtures studied were a stoichiometric mixture of methane and oxygen ($CH_4/2O_2$) and a stoichiometric mixture of hydrogen–oxygen diluted with argon ($2H_2/O_2/2Ar$). For each mixture, its sensitivity was controlled by changing the initial pressure of the test gas. These two mixtures were selected by their substantial differences in cellular regularity. Their characteristic properties are also summarized in Table 1. Their adiabatic index evaluated at the Von-Neumann state, $\gamma_{VN}$, and the detonation stability parameter [3], $\chi$, change over a sufficiently wide range. All the reported experiments are conducted at an initial temperature of 293 K.

### 2.2. Experimental results: the role of the CD nozzle

The role of the converging section was to overdrive the detonation. Fig. 2 depicts the detonation structures of the two mixtures during this compression. It appears that a Mach type reflection is not evident at these small angles of incidence, which is in qualitative agreement with previous works [16]. This appears to be a signature of reactive Mach reflections, as recently studied by Short et al. [18]. This desirable feature makes the technique adequate, as it does not introduce strong reflections that will persist in the diverging section of the nozzle. Nevertheless, the cellular structures persist on the front of the overdriven detonations. The methane–oxygen detonation retains the spotty structure indicative of non-reacted pockets, as well as its long-lived transverse waves. These features are less pronounced in the hydrogen–oxygen–argon mixture. In these experiments, the detonation speed increases to approximately $1.1D_{CJ}$ and $1.06D_{CJ}$ at the throat in the methane–oxygen and hydrogen–oxygen–argon mixtures, respectively.

The success of our technique requires that the detonation transmission in the enlarging section is subcritical, giving rise to a decaying shock followed by a decoupled reaction zone. The criterion for this was found in good agreement with detonation diffraction phenomenology. By applying equation (12) from [19], which establishes a relationship between the exponential sensitivity of cell size and induction zone length to velocity deficit in the strong shock limit, we estimated the cell size of the overdriven detonation, denoted as $\lambda$, at the end of the converging section. Our findings indicate that the conditions for the wave to undergo attenuation after the transition to the diverging section align with the critical gap height in diffraction problems. The reported critical gap height ranges from $G/\lambda \approx 3-10$, with variations dependent on mixture irregularity and the dimensions of the opening [20].

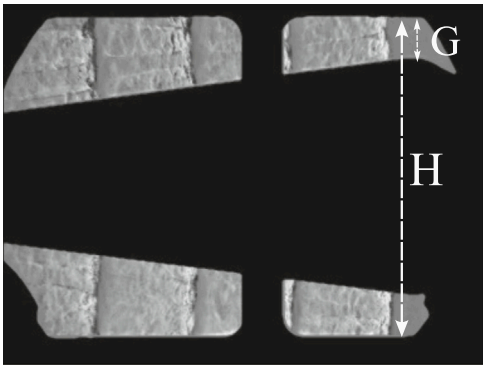


(a) $CH_4/2O_2$ at $p_0$= 17 kPa

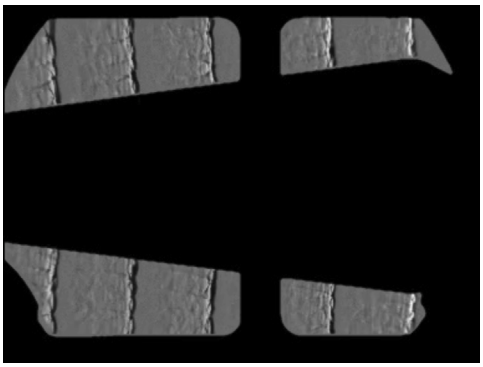

(b) $2H_2/O_2/2Ar$ at $p_0$= 9.6 kPa

**Fig. 2.** Composite schlieren images of the formation of the overdriven detonation through the converging channels. The height of the channel, $H$, is 0.203-m and the gap height, $G$, is 0.0265-m. Supplemental video materials illustrate the evolution process.

### 2.3. Experimental results: the Mach reflection

In our experimental observations, we identified three distinct regimes immediately following the reflection of the two incident shocks. These regimes are the formation of a detonation wave, the creation of a decaying Mach shock accompanied by a reaction front, and the generation of an inert Mach shock with no ignition occurring behind it.

Fig. 3(a) illustrates the diffraction of the detonation in the diverging channel followed by the formation of Mach shock from shock reflection. Multiple frames are overlaid in the same image to illustrate the evolution of the two incident shocks over time before the reflection. Schlieren photographs, capturing density gradients, distinctly reveal the boundary between burned and shocked yet non-burned gases. The reaction zone consistently lags behind the lead shock. Following the interaction of the two decaying shocks on the plane of symmetry, a strong overdriven detonation is formed and continues propagating along the channel. The cellular structure in the newly formed detonation is clearly visible, with very small cells in the order of millimeters.

In a slightly less sensitive mixture, detonation fails to form from the reflection, signifying the close proximity to the transition between the two regimes. An example is shown in Fig. 3(b). The transmitted Mach reflection takes the form of a decaying shock followed by a reaction zone trailing far behind. The absence of combustion coupled to the shock front leads to the accumulation of unburned gas behind the decaying shock over time. Altering the geometry to reduce the gap height by a factor of four ($G$ = 0.0065 m) significantly accelerates the decoupling between the shock and reaction front in the diverging section, as evident in Fig. 3(c). The two incident shocks decay much more rapidly, observable in the schlieren images as the unreacted region behind the shock front progressively increases. At the apex of the object where the two incident shocks interact, an inert Mach shock is formed, indicating the absence of ignition behind the shock front. The accumulation of unreacted gas behind the shock serves as a signature of the shock's weakness compared to the other scenarios. A similar pattern was observed in the geometry with a gap height of $G$ = 0.0132 m, where ignition never occurred behind the front, videos are provided as supplementary material.

The strength of the decaying shocks prior to the collision and the strength of the Mach shocks for the three previous examples are shown in Fig. 4. The data presented are from repeated experiments conducted under identical conditions. The speed of the incident shock waves decaying in the diverging section was measured along the top and bottom walls. The speed of the Mach shock was measured along the centerline. It is evident that the local speed profile undergoes significant deceleration along the diverging section, decreasing the velocity from $1.05D_{CJ}$ to $0.6D_{CJ}$ for both cases of detonation and decoupled Mach shock-reaction front. This deceleration is even more pronounced in the no ignition case, particularly when a small gap height is involved, dropping the velocity to $0.5D_{CJ}$. Following the interaction of the two decaying shocks, the velocity of the newly formed Mach shock is approximately $0.95D_{CJ}$ (in average for repeated experiments) for the detonation formation and due to the effect of combustion it rapidly increases to CJ speed and continues to propagate at around $0.9D_{CJ}$. Conversely, in scenarios where detonation did not occur, the Mach shock velocity in average is around $0.85D_{CJ}$ and continues to decay to lower velocities as it is decoupled from the reaction front. The Mach shock velocity is estimated utilizing an interframe time of 12 μs. High-speed video analysis shows this interframe time does not resolve the occurrence of the ignition event. Consequently, the Mach shock velocity in the detonation case is higher (0.95) compared to the ignition and decay case (0.85). In the case of no ignition, where the two incident shocks exhibit relatively low strength, the Mach shock's velocity only experiences a 10% increase after the reflection, reaching $0.65D_{CJ}$. Subsequently, it continues to decay rapidly, given its nature as a weak inert shock.

The experiments conducted in the methane–oxygen mixtures showed qualitatively similar behavior. Fig. 5(a) illustrates a reflection giving rise to a detonation. Fig. 5(b) illustrates a reflection giving rise to ignition and decay, whereas Fig. 5(c) shows a case with quenched ignition behind the decaying shock. Both the experiments in Figs. 5(a) and 5(b) were obtained at the same operating conditions, hence reflect the critical conditions separating the two regimes. Due to the cellular irregularity and highly sensitive chemistry of the methane–oxygen mixture, the reaction front is characterized by significant hydrodynamic fluctuations and unreacted pockets, which remain even in the enlarging sections of the channel. The presence of these sub-scale phenomena may have contributed to the re-ignition process after the reflection. This stands in contrast to the mostly laminar reaction front observed in the hydrogen–oxygen–argon mixture as it decays in the diverging section.

The detonation initiation case of Fig. 5(a) displays the characteristic very fine cellular structure on the front and transverse detonations. These can be identified by the very high levels of light emission overwhelming the schlieren signal. A much finer-scale inner structure than the hydrogen detonations is clearly evident. The presence of numerous cells across the channel thickness, 19 mm, indicates that the boundary layer has a negligible impact on small scales in the detonation formation process. Over the length required for detonation to form, approximately 100 mm, the boundary layer thickness only grows to 0.8 mm. In contrast to the previous case, Fig. 5(b) shows a decaying Mach shock followed by a mostly laminar reaction front. The transverse waves are non-reactive in this case, and long tongues of unburned gas are apparent, accompanied by a very fine scale structure. At the nascence of this Mach reflection, ignition and forward jet entrainment are obvious — see the high-speed videos available as supplementary material. These take the same form as the jet structure observed in

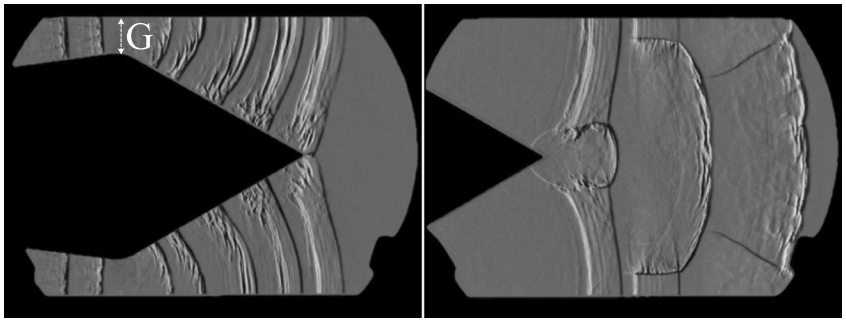


(a) Detonation formation, $G$= 0.0265-m, $p_0$= 9.6 kPa

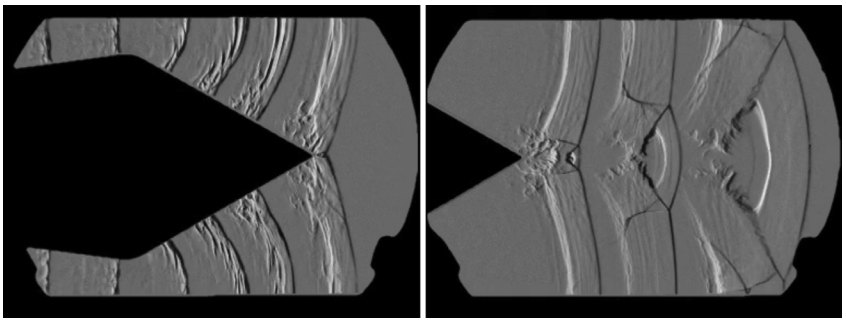

(b) Decaying Mach shock followed by a flame, $G$= 0.0265-m, $p_0$= 9 kPa

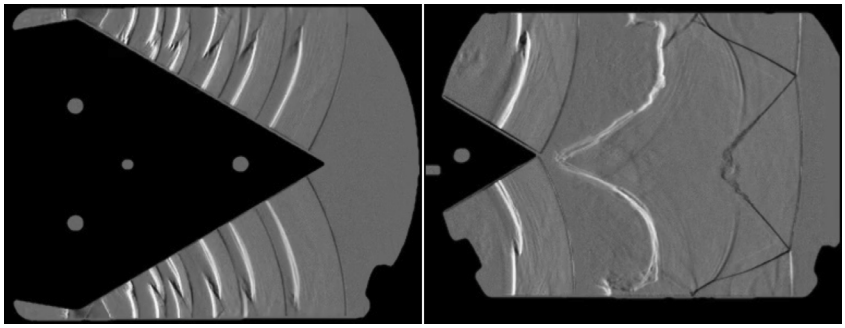

(c) Inert Mach shock with no re-ignition, $G$= 0.0065-m, $p_0$= 9.6 kPa

**Fig. 3.** Composite schlieren images of the formation of the three distinctive regimes in the $2H_2/O_2/2Ar$ mixture. Supplemental video materials illustrate the evolution process.

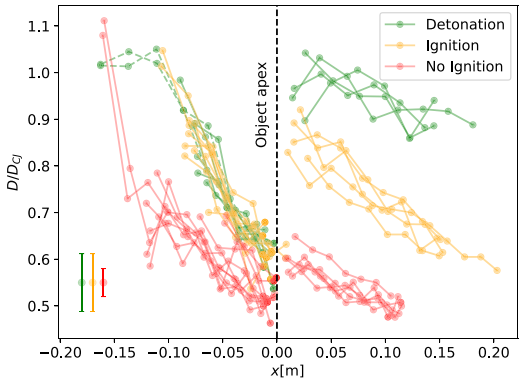


**Fig. 4.** The evolution of the non-dimensional velocity with distance for the decaying incident shocks on the top and bottom walls of the shock tube and the Mach shock on the centerline in the $2H_2/O_2/2Ar$ mixture. Similar to Fig. 3, for the detonation and no ignition cases $p_0$ = 9.6 kPa and for the ignition case at $p_0$ = 9 kPa. The error bars show the velocity uncertainty calculated from video analysis.

our previous studies using round obstacles to induce the reflection process [5].

For the experiment illustrated in Fig. 5(c) for a reduced gap height, there is a pronounced quenching effect on the two incoming incident shocks as they diffract. These decaying shocks are very smooth, with a combustion zone decoupled in the back. The resulting Mach reflection did not re-ignite the gas. Instead, the detailed structure of a double Mach reflection followed by a forward-facing jet is clearly observable. Shear layer instabilities along the vortex line joining the jet head are also clearly discernible. Similarly, the gap height of 0.0132 m led to Mach reflection without ignition. The video is included as supplementary material.

Fig. 6 shows the velocity evolution along the shock tube walls in the diverging channel and the center line after the reflection for the methane–oxygen, based on multiple experiments performed under the same initial conditions. In all three scenarios of detonation, ignition, and no ignition, the velocity transitions from overdriven detonation to a weak shock before the collisions of the two triple points. However, in the first two cases, after the collision, it increases to approximately 0.85 $D_{CJ}$, while in the no ignition case, the reflection of two extremely weak shocks forms a weaker Mach shock of approximately 0.6 $D_{CJ}$. The disparities in velocities of the Mach shocks between the ignition and detonation scenarios are not as prominent as observed in the hydrogen–oxygen–argon cases. This may be attributed to the presence of the forward jet behind the Mach shock, turbulent reaction front, and other

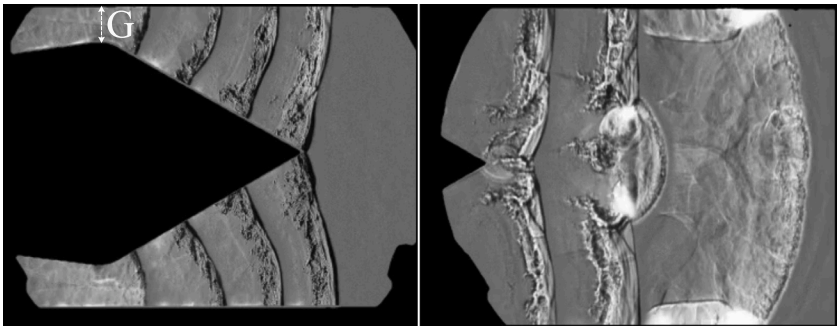


(a) Detonation formation, $G$= 0.0265-m, $p_0$= 19 kPa

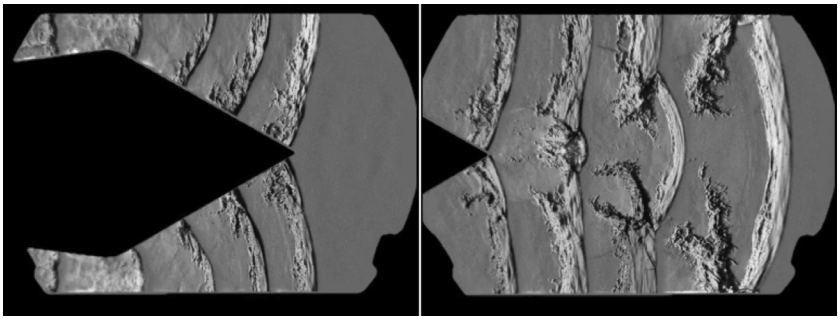

(b) Decaying Mach shock followed by a flame, $G$= 0.0265-m, $p_0$= 19 kPa

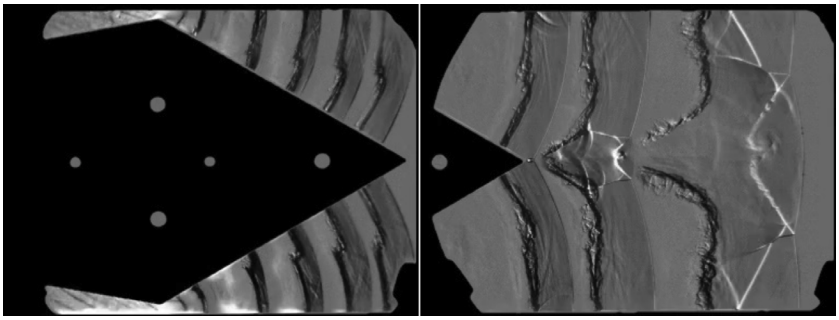

(c) Inert Mach shock with no re-ignition, $G$= 0.0065-m, $p_0$= 19 kPa

**Fig. 5.** Composite schlieren images of the formation of the three distinctive regimes in the $CH_4/2O_2$ mixture. Supplemental video materials illustrate the evolution process.

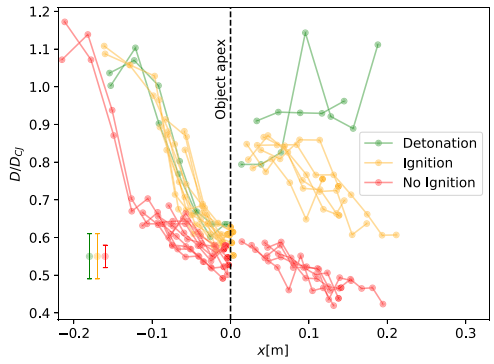


**Fig. 6.** The evolution of the non-dimensional velocity with distance for the decaying incident shocks on the top and bottom walls of the shock tube (represented by dashed lines) and the Mach shock on the centerline (illustrated by solid lines) in the $CH_4/2O_2$ mixture. Similar to Fig. 5, for all three cases $p_0$ = 19 kPa. The error bars show the velocity uncertainty calculated from video analysis.

hydrodynamic instabilities in the more unstable mixture of methane–oxygen. The sole differentiation between the two regimes based on speed alone makes the difference between the locally gasdynamically coupled detonation and the shock followed by turbulent combustion less obvious. Nevertheless, the two regimes are markedly different in the structure of the front. The detonation initiation is accompanied by a very fine scale cellular structure, while the shock-turbulent flame is not.

Repeated experiments (minimum five times) were performed at each pressure tested and a probability of detonation formation was established. Fig. 7 shows the results for both mixtures. The critical pressure of formation is $9 \pm 0.75$ kPa for the $2H_2/O_2/2Ar$ mixture and $18.1 \pm 2.6$ kPa for the $CH_4/2O_2$ mixture. The range of pressures in which both success and failure are possible represent approximately 17% and 29% of the critical pressures recorded for $2H_2/O_2/2Ar$ and $CH_4/2O_2$ mixtures, respectively. Beyond these limits, the detonation does not completely quench in the diverging section.

## 3. Prediction of detonation, ignition and no ignition scenarios

In the following two sections, the conditions that differentiate between the various transmission regimes are explored using two conceptual models related to detonation dynamics: the critical ignition due to volumetric expansion behind decaying shocks and critical conditions for establishing local gasdynamics choking and quasi-steady propagation.

**Table 2**
Summary of the experimental measurements and Mach shock calculation in the $2H_2/O_2/2Ar$ mixture.

| Regime | $p_0$ [kPa] | $\frac{\dot{D}}{D}$ [$s^{-1}$] | $D_{\text{incoming}}$ [$m\,s^{-1}$] | $D_M$ [$m\,s^{-1}$] |
|---|---|---|---|---|
| Detonation formation | $9.4 \pm 0.3$ | $-3257 \pm 598$ | $1485 \pm 19$ | $1870 \pm 24$ |
| Decaying Mach shock followed by a flame | $8.9 \pm 0.4$ | $-3884 \pm 875$ | $1442 \pm 20$ | $1815 \pm 24$ |
| No re-ignition | $9.6 \pm 1.5$ | $-2357 \pm 295$ | $1077 \pm 23$ | $1361 \pm 29$ |

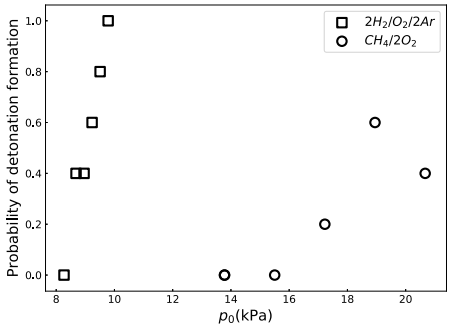


**Fig. 7.** Probability of successful detonation formation as a function of initial pressure.

### 3.1. Model for critical ignition behind decaying Mach shock

The quenching of chemical reactions in the presence of strong gas dynamic expansions has been identified by numerous researchers as an important mechanism controlling ignition behind decaying shocks [7, 8,10,21]. A summary of the state of the art is provided by Cheevers and Radulescu [11]. The main contribution is that by Eckett et al. [8], who analyzed the ignition process along a particle path and identified a critical expansion rate, which prevents ignition. Extinction is then predicted to occur when

$$\zeta = \frac{Ea}{RT_s}(\gamma - 1)\frac{t_i}{t_{exp}} > 1 \tag{1}$$

where $\frac{Ea}{RT_s}$ is the dimensionless activation energy, $\gamma$ is the specific heat ratio in the post-shock region, $T_s$ is the post-shock temperature, $t_i$ is nominal ignition delay time in the absence of expansion and $t_{exp}$ is the characteristic time of the expansion along a particle path. To link this criterion to ignition behind a decaying shock, it is sufficient to determine the relation between the expansion rate along a particle path, the shock speed, decay rate and curvature. Radulescu [10] established this relation by using the shock change equations. For a strong shock, the relation is:

$$t_{exp}^{-1} = \frac{1}{\rho}\frac{D\rho}{Dt} = \frac{6\dot{D}}{(\gamma+1)D} + \frac{2D\kappa(\gamma-1)}{(\gamma+1)^2} \tag{2}$$

this relation generalizes the result of Eckett et al. obtained for planar shocks, where only the first term in Eq. (2) appeared in their analysis.

To test this ignition model in our experiments, we require the speed of the Mach shock, $D$, its decay rate, $\dot{D}$, its curvature, $\kappa$, and the ignition delay behind the inert Mach shock, $t_i$. We determine the strength of the Mach shock in our experiments by employing real gas calculations of standard Mach reflections, assuming a flat Mach shock [22]. The schematic of the problem is illustrated in Fig. 8(a). All waves in this scenario are treated as oblique shocks relative to the triple point reference frame. This model requires three inputs: the mixture composition, the normal velocity of the incoming shock, $D_{\text{incoming}}$, and the inclination angle of the shock, $\alpha$, in the pre-reflection region. The triple point trajectory angle relative to the axis of symmetry after the reflection is denoted as $\eta$. The correct value of $\eta$ is determined using the bisection method to satisfy the conditions of matching pressure and flow direction across the shear layer, as identified by regions 1 and 2.

In this study, shown in Fig. 8(b), the calculation of the angle $\eta$ requires the speed of the incoming shocks. This velocity is derived from our experiments by averaging the velocities of the two incoming shocks at the top and bottom of the object. This calculation tracks the position of the normal shock across multiple frames before reflection, during which the shock and combustion front became detached, resulting in the formation of a decaying shock. The uncertainty associated with measurements of the incoming decaying shock can reach up to ±250 m/s across different experiments. With $\alpha$ fixed at 30° due to the geometry, the strength of the newly formed Mach shock is estimated [17].

Tables 2 and 3 present the quantitative data for the average velocity of the incoming shocks, $D_{\text{incoming}}$, and the calculated Mach shock velocity, $D_{\text{M}}$, using the three-shock theory. These values, along with their standard deviations, are shown for both mixtures across the given range of initial pressures, $p_0$. Finally, the nominal ignition delay time was determined using constant-volume homogeneous reactor calculations from Cantera [23]. To determine the deceleration of the Mach shock, we make use of the relation:

$$\frac{\dot{D}}{D} = \frac{\mathrm{d}D}{\mathrm{d}x} \tag{3}$$

Our monitoring of the Mach reflection in the inert regime indicates that $\frac{\dot{D}}{D}$ remains approximately constant through the reflection. Fig. 9 demonstrates the constancy of the expansion rate for both the incoming decaying shock prior to reflection and the newly formed Mach shock after the reflection. The data points represent experimental velocity measurements, while the fitted lines indicate the linear regression for both shocks. The uncertainty in the slope was determined to be approximately 30%. This was estimated using the `curve_fit` function from the SciPy library [24], which performs a non-linear least squares fit to the data while accounting for uncertainties in the dependent variable (D-values). The deceleration over velocity data, $\dot{D}/D$, measured from the experiments are provided in Tables 2 and 3 for both mixtures.

To investigate the effect of the second term in Eq. (2), the curvature of the Mach shock in the first two frames immediately following the reflection was measured. For the hydrogen mixture, the curvature was estimated to be $28 \pm 5\,m^{-1}$ in the detonation and ignition regimes, and $19 \pm 5\,m^{-1}$ in the no ignition regime. For methane mixtures, the curvature was $51 \pm 14\,m^{-1}$ in the detonation and ignition regimes, and $28 \pm 9\,m^{-1}$ in the no ignition regime. The values following "±" represent the standard deviation across all the experiments considered in each regime. Under these experimental conditions, the contribution of the curvature to Eq. (2) is therefore negligible. Consequently, the influence of the curvature was not further included in the model prediction. Fig. 10 provides a summary of the experimentally inferred decay rate coefficients $\zeta$ of the Mach shock and comparison to Eckett's criterion given by Eq. (1). As can be verified, the criterion serves as a good indicator for the boundary between the experiments where ignition was observed behind the lead shock, and experiments where ignition was not observed. We can thus conclude that the physical mechanism leading to the quenching of the gas and the absence of ignition is excessive cooling in the induction zone resulting from the volumetric expansion induced by the deceleration of the leading shock. More correctly said, it is due to the volumetric expansion that is also *responsible* for the shock decay — brought about by the diverging geometry controlling the incident shock, which the Mach shock inherits from its predecessor. We note however that the ignition criterion fails to predict the transition between detonation formation and no detonation (marked by the transition between green and yellow circles). For the hydrogen mixture, it can be seen that the criterion is more than an

**Table 3**
Summary of the experimental measurements and Mach shock calculation in the $CH_4/2O_2$ mixture.

| Regime | $p_0$ [kPa] | $\frac{D}{D}$ [$s^{-1}$] | $D_{incoming}$ [$m\,s^{-1}$] | $D_M$ [$m\,s^{-1}$] |
|---|---|---|---|---|
| Detonation formation | $19.3 \pm 1.3$ | $-2696 \pm 473$ | $1736 \pm 31$ | $2128 \pm 38$ |
| Decaying Mach shock followed by a flame | $16.9 \pm 2$ | $-2770 \pm 739$ | $1698 \pm 47$ | $2082 \pm 56$ |
| No re-ignition | $14.2 \pm 3.5$ | $-3464 \pm 655$ | $1201 \pm 43$ | $1485 \pm 52$ |

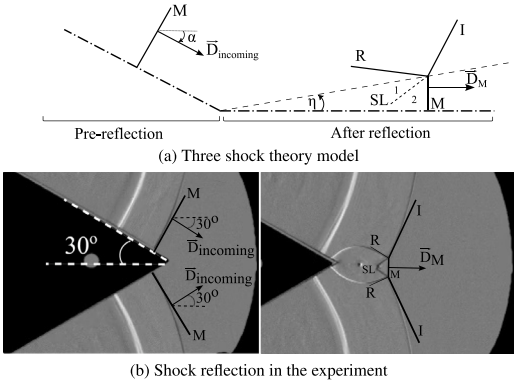


(a) Three shock theory model

(b) Shock reflection in the experiment

**Fig. 8.** Schematic of the shock reflection prior to and after the reflection. $D$: velocity, $R$: reflected shock, $M$: Mach shock, $SL$: slip line, $I$: incident shock and $\eta$: angle of the triple point trajectory with the horizontal line.

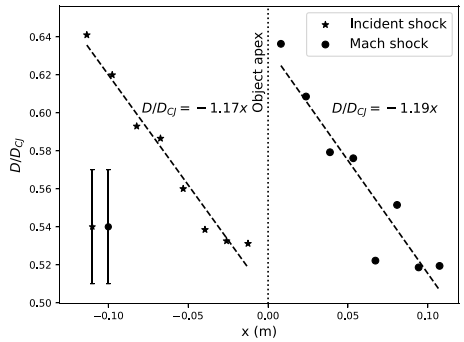


**Fig. 9.** Evolution of the non-dimensional shock velocity on the object before reflection and along the center line after reflection as a function of distance. The error bars represent the velocity uncertainty derived from video analysis.

order of magnitude different from the experimental results. The ignition quenching criterion is not adequate. This discrepancy cannot be attributed to experimental or data reduction error, estimated at a factor of 2, since the hydrogen experiments were sufficiently well resolved to accurately infer the shock speed, its decay rate and ignition behind it using available chemical kinetic models for hydrogen.

### *3.2. Model for critical conditions for detonation initiation*

As discussed in the literature, it is believed that self-sustaining detonations require gas-dynamic choking for sustenance and amplification, as conceptualized by Detonation Shock Dynamics theoretical framework for weakly curved, weakly non-steady detonations [12–14,25]. Curvature and non-steadiness in the quasi-steady model account for losses that bring about substantial detonation speed deficits. The quasi-steady relation between detonation deficit and curvature acts as an attractor for critically forming detonations [13,14]. Previous studies of propagating detonations suggested that the early parts of the shock decay inside the cell can be described by this DSD framework [26].

To explore the usefulness of this concept [13,14] in predicting the criticality observed in our experiments for detonations formed or not formed, we extracted the detonation speed evolution as a function of its local radius of curvature, $R = 1/\kappa$. The curvatures data were obtained by curve-fitting the entire shock shape of the Mach shock obtained experimentally, as shown in Fig. 11. The velocity of the Mach shock was measured by tracking its position at each frame along the axis of symmetry between the two triple points. For the newly formed Mach shock, the measurement uncertainty can be as high as ±185 m/s.

Figs. 12 and 13 present the data from 10 experiments for each mixture, showcasing the three different regimes observed. The initial pressures vary across these experiments. Each data point represents the average between two consecutive frames, recorded from the first frame after the formation of the Mach shock, at which the extraction of radius data became feasible. To make the comparison with the quasi-steady curvature response, we also plot the prediction using ZND theory and the experimentally measured speed–curvature data obtained in our previous studies using the exponential horn technique [27,28].

Our experiment reveals that following the shock reflection and reaching the critical curvature, the Mach shock will either move towards a quasi-steady solution if the velocity at that point exceeds the critical velocity or decay if it falls below it. The results obtained for the hydrogen mixture shown in Fig. 12 are striking. The critical experiment leading to detonation formation (green circles) suggests that the reflection gives rise to a near CJ detonation that rapidly decays to its weakly curved evolution given by the ZND model and experimentally determined curvature response. On the other hand, the decaying Mach shock experiment (yellow circles) indicates that the Mach shock evolves below the bottom branch of the $D(R)$ curve, which implies decoupling dynamics in DSD theory [14,21]. Our results are thus in perfect agreement with DSD theory.

The results obtained for the methane–oxygen system shown in Fig. 13 indicate similar dynamics, albeit less clearly. The case of the Mach shock followed by a decoupled reaction zone decays below the critical turning point in the experimentally determined speed–curvature curve (black points). The dynamics of the detonation forming show significant oscillations while approaching the top portion of the curve. Nevertheless, the bifurcation between the initiating case and failure case appears to occur for the smaller radius of curvature on the order of a few millimeters. This approaches the experimental limit at which we can estimate the curvature of the front. Clearly, experiments with higher resolution and better control of the incident wave structure are required in this case to achieve more definitive results. Nevertheless, what we can conclude with certainty is the inability of the curved ZND model to make a useful prediction in this case, since the bifurcation in the experiments occurs at a radius of curvature an order of magnitude smaller than anticipated from laminar theory. This again stresses the inability of the laminar model to capture the dynamics of the nascent detonations in very irregular mixtures. The reason for this discrepancy is believed to be the role of the fine-scale structure developing very fast on the surface of these detonations, invalidating the one-dimensional laminar assumption.

## 4. Conclusion

The current study introduced a novel technique to effectively isolate the process of reactive Mach shock formation from the reflection of two incident shocks. Three distinct regimes were successfully identified: detonation formation, ignition occurring behind the decaying Mach shock, and Mach shock with no ignition. Utilizing high-speed schlieren videos, measurements were taken to quantify the strength, decay rate, and curvatures of both incident and Mach shocks.

29

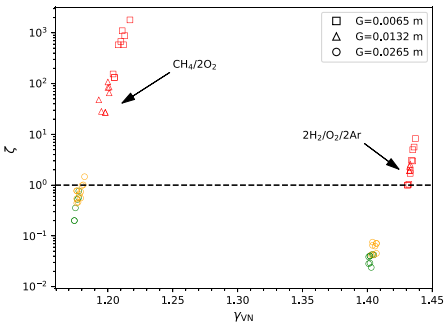


**Fig. 10.** The decay rate coefficient versus specific heat ratio. The initial pressure in the $CH_4/2O_2$ mixture ranges from 10 to 21 kPa, and in the $2H_2/O_2/2Ar$ mixture, it ranges from 7 to 11 kPa. The color green, yellow and red represent detonation formation, ignition, and no re-ignition regimes, respectively. (For interpretation of the references to color in this figure legend, the reader is referred to the web version of this article.)

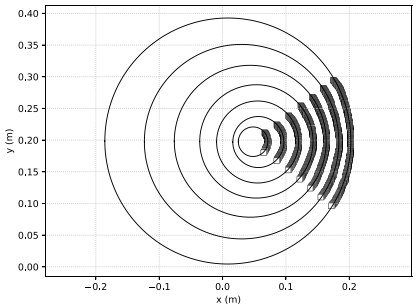


**Fig. 11.** Positions of all pixels on the curvature front of the Mach shock across several frames, with a fitted circle for each curvature. Point 0 indicates the apex of the object.

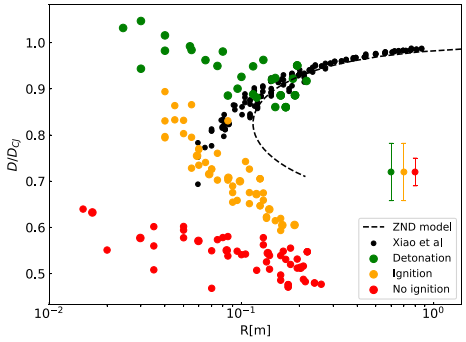


**Fig. 12.** The non-dimensional velocity versus radius data obtained from this study, quasi-steady-state detonation experiments [27], and predictions derived from the generalized ZND model. The test gas is mixture of $2H_2/O_2/2Ar$, with initial pressures varying as indicated in Table 2. The error bars represent the velocity uncertainty derived from video analysis in this study. (For interpretation of the references to color in this figure legend, the reader is referred to the web version of this article.)

We demonstrated that the decay rate model, incorporating the expansion behind the decaying shock, effectively predicts the critical conditions that differentiate between ignition and no-ignition regimes in both mixtures. Critical conditions that differentiate between the regimes of detonation initiation and failure are compatible with the theory of weakly non-steady curved detonations. The formation of a quasi-steady detonation wave can be explained by the establishment of a sonic surface within the structure of detonation waves as it reaches the critical curvature point. While the critical curvature was well predicted by laminar ZND theory for weakly curved detonations for the regular structure hydrogen–oxygen–argon mixture, this was not the case for the much more irregular detonations in the methane–oxygen mixture. For this mixture, agreement was much better with the mean

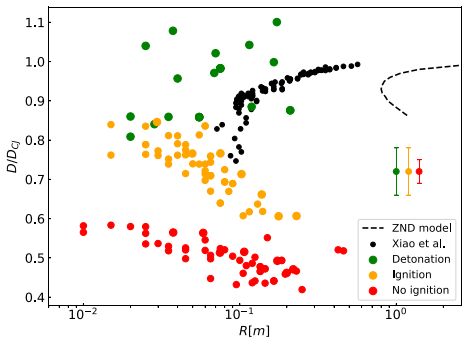


**Fig. 13.** The non-dimensional velocity versus radius data obtained from this study, quasi-steady-state detonation experiments [28], and predictions derived from the generalized ZND model. The test gas is mixture of $CH_4/2O_2$, with initial pressures varying as indicated in Table 3. The error bars represent the velocity uncertainty derived from video analysis in this study.

detonation–curvature relation obtained for cellular detonations. It can be speculated that the fine sub-scale cellular structure promotes the propagation of these detonations.

## Novelty and significance statement

1. We have isolated the reactive Mach reflection configuration relevant to the cellular structure of detonations in a novel experiment with unprecedented clarity. The model permits to establish the physics controlling the outcome of the reflection.
2. We have established the three regimes of Mach reflections: detonations, shock with a de-coupled reaction zone and shock with a quenched reaction.
3. We conclusively saw the physical mechanism controlling the boundary between each regime.
4. Expansion wave quenching controls the difference between shock reflection with or without ignition.
5. The establishment of quasi-steady curved detonation controls the difference between establishing detonation and shock with a decoupled reaction zone.

## CRediT authorship contribution statement

**Farzane Zangene:** Performed research and manuscript preparation, reviewed the results and approved the final version of the manuscript. **Matei I. Radulescu:** Supervised every phase of the research, reviewed the results and approved the final version of the manuscript.

## Declaration of competing interest

The authors declare that they have no known competing financial interests or personal relationships that could have appeared to influence the work reported in this paper.

## Acknowledgments

This work was supported by AFOSR, United states grant FA9550-23-1-0214, with Dr. Chiping Li as program monitor and the NSERC, Canada Discovery Grant "Predictability of detonation wave dynamics in gases: experiment and model development".

## Appendix A. Supplementary data

Supplementary material related to this article can be found online at https://doi.org/10.1016/j.proci.2024.105774.

30

## References


[1] J. Lee, Dynamic parameters of gaseous detonations, Annu. Rev. Fluid Mech. 16 (1) (1984) 311–336.

[2] W. Fickett, W. Davis, Detonation : theory and experiment, University of California Press, 1979.

[3] M. Radulescu, The propagation and failure mechanism of gaseous detonations: experiments in porous-walled tubes (Ph.D. thesis), McGill University, 2003.

[4] M.I. Radulescu, G.J. Sharpe, C.K. Law, J.H. Lee, The hydrodynamic structure of unstable cellular detonations, J. Fluid Mech. 580 (2007) 31–81.

[5] R. Bhattacharjee, S. Lau-Chapdelaine, G. Maines, L. Maley, M. Radulescu, Detonation re-initiation mechanism following the mach reflection of a quenched detonation, Proc. Combust. Inst. 34 (2) (2013) 1893–1901.

[6] D. White, K. Cary, Structure of gaseous detonation. Generation of laminar detonation, Phys. Fluids 6 (5) (1963) 749–750.

[7] E. Lundstrom, A. Oppenheim, On the influence of non-steadiness on the thickness of the detonation wave, Proc. R. Soc. A 310 (1503) (1969) 463–478.

[8] C. Eckett, J. Quirk, J. Shepherd, The role of unsteadiness in direct initiation of gaseous detonations, J. Fluid Mech. 421 (2000) 147–183.

[9] J. Austin, The role of instability in gaseous detonation (Ph.D. thesis), California Institute of Technology, Pasadena, California, 2003.

[10] M. Radulescu, B. Maxwell, Critical ignition in rapidly expanding self-similar flows, Phys. Fluids 22 (6) (2010) 066101.

[11] K. Cheevers, M. Radulescu, Ignition behind decaying shock waves: Detonation cells, 2022, arXiv preprint arXiv:2211.05216.

[12] J. Yao, D.S. Stewart, On the dynamics of multi-dimensional detonation, J. Fluid Mech. 309 (1996) 225–275.

[13] P. Vidal, Critical slow dynamics of detonation in a gas with non-uniform initial temperature and composition: A large-activation-energy analysis, Int. J. Spray Combust. Dyn. 1 (4) (2009) 435–471.

[14] A. Kasimov, D. Stewart, Asymptotic theory of evolution and failure of self-sustained detonations, J. Fluid Mech. 525 (2005) 161–192.

[15] R. Bhattacharjee, Experimental investigation of detonation re-initiation mechanisms following a Mach reflection of a quenched detonation (Master thesis), University of Ottawa, 2013.

[16] R. Akbar, Mach reflection of gaseous detonations (Ph.D. thesis), Rensselaer Polytechnic Institute, 1997.

[17] F. Zangene, M. Radulescu, Modelling and experiments of triple point reflection in detonations, in: The 34th International Symposium on Shock Waves, Korea, 2023.

[18] M. Short, C. Chiquete, S. Voelkel, Effect of a spatially distributed reaction zone on regular and mach reflection of a detonation, in: Proceedings of the 29th International Colloquium on the Dynamics of Explosions and Reactive Systems, 2023.

[19] Q. Xiao, A. Sow, B. Maxwell, M. Radulescu, Effect of boundary layer losses on 2D detonation cellular structures, Proc. Combust. Inst. 38 (2021) 3641–3649.

[20] F. Zangene, Q. Xiao, M. Radulescu, Critical diffraction of irregular structure detonations and their predictability from experimentally obtained D- $\kappa$ data, Proc. Combust. Inst. 39 (3) (2023) 2935–2944.

[21] P. Vidal, B. Khasainov, Analysis of critical dynamics for shock-induced adiabatic explosions by means of the Cauchy problem for the shock transformation, Shock Waves 9 (1999) 273–290.

[22] H. Hornung, Regular and Mach reflection of shock waves, Annu. Rev. Fluid Mech. 18 (1) (1986) 33–58.

[23] D. Goodwin, R. Speth, H. Moffat, B. Weber, Cantera: An object-oriented software toolkit for chemical kinetics, thermodynamics, and transport processes, 2021, Version 2.5.1.

[24] P. Virtanen, R. Gommers, T.E. Oliphant, et al., SciPy 1.0: Fundamental algorithms for scientific computing in python, Nat. Methods 17 (2020) 261–272.

[25] J.B. Bdzil, D.S. Stewart, The dynamics of detonation in explosive systems, Annu. Rev. Fluid Mech. 39 (1) (2007) 263–292.

[26] S.I. Jackson, C. Chiquete, M. Short, An intrinsic velocity–curvature–acceleration relationship for weakly unstable gaseous detonations, Proc. Combust. Inst. 37 (3) (2019) 3601–3607.

[27] Q. Xiao, M. Radulescu, Dynamics of hydrogen–oxygen–argon cellular detonations with a constant mean lateral strain rate, Combust. Flame 215 (2020) 437–457.

[28] Q. Xiao, M. Radulescu, Role of instability on the limits of laterally strained detonation waves, Combust. Flame 220 (2020) 410–428.

# Chapter 4

# Role of the argon and helium bath gases on the detonation structure of $H_2/O_2$ mixture

A more suitable set-up to test the relationship between small-scale and large-scale structures is a narrow channel in which the loss comes from the global divergence of the flow due to the presence of the boundary layer. This permits us to investigate the coupling between cellular dynamics and lateral flow divergence in a steady detonation propagation. The lateral divergence is experimentally controlled by the proximity of the detonations to their propagation limits. Furthermore, the effects of two inert monoatomic diluents, argon and helium, on the detonation structure are examined to evaluate the significance of wall losses and vibrational non-equilibrium.

This study has been submitted to the *Journal of Combustion and Flame* and the revision is requested. The author conducted the experiments, simulations, and analyses, and wrote the paper. The conceptual planning and paper review was done in collaboration with the PhD supervisor, Prof. M. I. Radulescu.

# Role of the argon and helium bath gases on the structure of $H_2/O_2$ detonations

Farzane Zangene, Matei I. Radulescu

*Department of Mechanical Engineering, University of Ottawa, Ottawa, ON K1N6N5, Canada*

**Abstract**

This study investigates the role of two inert mono-atomic diluents, argon and helium, on the detonation structure in order to assess the importance of vibrational non-equilibrium and wall losses. When relaxation effects and wall losses are neglected, the detonation waves in mixtures diluted with either of these gases have the same kinetics, Mach number, and specific heat ratio and hence are expected to lead to the same cellular dynamics. Differences in transport properties and species relaxation rates thus permit to establish the importance of these effects. The experiments were conducted in $2H_2 + O_2 + 7Ar$ and $2H_2 + O_2 + 7He$ mixtures in a narrow channel, where boundary layer losses can be controlled by the proximity of the detonations to their propagation limits. The initial pressure was adjusted in such a way that the induction zone length (therefore cell sizes) calculated from the ideal ZND model remained constant. The experiments revealed differences in velocity deficits and cell sizes despite maintaining a constant induction zone length across the mixtures. These differences were minimal in sensitive mixtures but became more pronounced as velocity deficits increased and cell sizes approached the channel dimensions. Near the detonation limits, the disparity in cell sizes between the two mixtures nearly doubled. These observations were reconciled by accounting for the wall losses. We incorporated the boundary layer flow divergence in a perturbation analysis based on the square wave detonation assumption. This permitted to establish the controlling loss parameter as the product of the induction to channel size and the inverse of the square root of the Reynolds number. The very good collapse of the scaled results with the two bath gases with the loss parameter, and further comparison with 2D numerical simulations with account for flow divergence to the third dimension, confirmed the viscous loss mechanism to be dominating. Calculations suggest that the slower relaxation of $H_2$ becomes comparable with the ignition delay anticipated from the ZND model and is slower by 70% in the argon diluted system. Differences possibly highlighting the role of non-equilibrium were not observed. This suggests the vibrational non-equilibrium effect may be less apparent in cellular detonations due to the

*Email address:* fzang055@uottawa.ca (Farzane Zangene)

lengthening of the ignition delays owing to the non-steady detonation structure. The study establishes that the large differences between the enlarged cells observed in our experiments and numerical predictions of lossless systems can be entirely attributed to wall losses.

*Keywords:* `Detonation cellular structure, Vibrational relaxation, Boundary layer losses, Inert diluent`

---

## 1. Introduction

The cellular structure of gaseous detonation waves has been known for over 60 years [1, 2]. Qualitatively, the physico-chemical processes occurring in the detonation structure are well understood, particularly for systems displaying regular cells [3]. Nevertheless, recent attempts to quantitatively model the detonation structure have led to large discrepancies between the numerical predictions and experimentally determined cell sizes [4]. These differences suggest the importance of other effects neglected in the modelling. Taylor et al. attribute these effects to possible influence of vibrational non-equilibrium [4]. They suggest that the excess translational energy in the induction zone may promote the rate processes in the induction zone chemical kinetics and account for the smaller cells. On the other hand, another possible explanation was provided by Xiao et al. [5]. They suggest that wall losses may have a strong influence on the detonation cells: with larger velocity deficits, the kinetics are slowed down and may yield much larger cells than detonations propagating without wall losses, as calculated by Taylor et al [4]. Indeed, experimental measurements of cell sizes reported in the literature are never corrected for the velocity deficit effects, hence do not permit direct comparison with lossless calculations. To this date, limited attempts have been made to answer this question. The preliminary experiments of this work were presented at the International Conference on Hydrogen Safety in 2021 [6] and the modelling in 2022 at the International Colloquium on the Dynamics of Explosions and Reactive Systems [7]. Subsequently, Shi et al. reported experiments and analysis of the possible speed-up in the induction zone owing to the vibrational non-equilibrium, but found the effect to be negligible [8]. Other changes in cellular dynamics have also been suggested by analysing the changes in the ZND rate processes in a simplified toy model [9]. On the other hand, Smith et al. conducted numerical simulations of $2H_2 + O_2 + 7Ar$ detonations in thin channels, accounting for the losses in an improved model over that of Xiao et al. [5] with a higher fidelity chemical model, but neglecting vibrational non-equilibrium, and found good agreement with experiment [10]. In the current communication, we wish to establish the relative role of these two effects experimentally. The strategy we use is the dilution of the $2H_2 + O_2$ system with either argon gas or helium gas. The diluents being chemically inert and mono-atomic, when relaxation effects and wall losses are neglected, the detonation waves in mixtures diluted with either of these gases have the same kinetics, Mach number, and specific heat ratio and hence are expected to lead

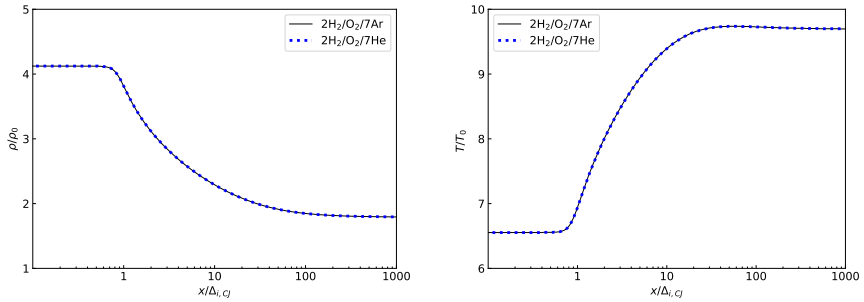


Figure 1: ZND profiles of (a) density and (b) temperature obtained by using the San Diego detailed chemical mechanism [11] at $p_0$= 10 kPa and $T_0$= 293 K. $\Delta_{i,CJ}$ is the induction zone length calculated from the ideal ZND model, $\rho_0$ is the initial density of the mixture.

to the same cellular dynamics. Differences in transport properties and species relaxation rates hence permit to establish the importance of these effects in a non-ambiguous manner. The experiments are conducted in a narrow channel, such that the magnitude of wall losses can be controlled by the proximity of the operating conditions to the minimum channel thickness permitting propagation.

For the same amount of dilution, initial pressure, and temperature, the diluent does not alter the ignition delay time since the shock Mach number and temperature ($T_{VN}$:Von-Neumann state) remain constant. Additionally, the effective activation energy ($E_a/RT_{VN}$) and the time scale ratio of induction to reaction ($t_i/t_r$) are unaffected. Consequently, no significant differences in the instability parameter, $\chi = (t_i/t_r)\,(E_a/RT_{VN})$, are expected [12]. Thermodynamically, the choice of diluent does not influence the specific heat ratio ($\gamma$) or heat release, resulting in the same ZND structure, as shown in Fig. 1. However, the relaxation rate of the reactants $H_2$ and $O_2$ will be affected by the type of diluent due to their significant difference in molecular weight. This will permit us to isolate their effect on the detonation structure.

Previous studies on the nature of the inert diluent are limited. Experiments in propane mixtures using both of these diluents as bath gases [13] in thin tubes demonstrated that galloping detonations were established near the propagation limits more readily in argon diluted mixtures than in helium diluted mixtures. This observation has not been resolved, but points to the importance of either the differences in transport coefficients in the helium mixture (due to increased thermal conductivity and sound speed), which may enhance dissipation and suppress the fine-scale instabilities necessary for the galloping phenomenon, or the vibrational non-equilibrium effects. The latter would act in the same direction, with non-equilibria being more important in the argon based system. Kumar et al. measured the cell widths experimentally in hydrogen-oxygen-helium and hydrogen-oxygen-argon mixtures at the same initial pressures and temperatures and showed that the cells in argon-diluted mixtures are smaller than those in helium-diluted mixtures [14, 15]. This difference was attributed to the variations in molecular weights (or post-shock velocities) between the helium and argon

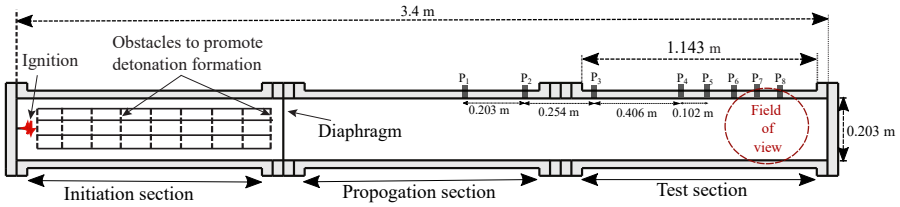


Figure 2: Schematic of the shock tube used in the experiment.

mixtures. Indeed, while ZND structure is the same in terms of time, length scales with the acoustic speed, will change due to the difference in molecular weights. For a meaningful comparison, our experiments fix the induction zone length by adjusting the initial pressure.

The paper is organized as follows: Section 2 outlines the experimental procedure and presents the results. Section 3 estimates the vibrational non-equilibrium time in the two mixtures with different bath gases, comparing it to the ignition delay time of each mixture. Section 4 discusses the modifications made to the existing boundary layer model, presents the numerical simulation results for detonation propagation, and compares these outcomes with experimental data. In the same section, the results of the ZND model with and without the losses are provided, followed by a discussion. Finally, section 5 provides a general discussion, followed by the study's conclusions. The appendix provides a closed model for detonations with boundary layer losses assuming the structure as a square wave. Through a perturbation analysis in the limit of high activation energy, we derive the dependence of the detonation speed on a newly derived loss parameter involving the ratio of induction to channel size and the Reynolds number.

## 2. Experiments

### *2.1. Experimental details*

Experiments were conducted in a rectangular shock tube with dimensions of 3.4 m in length, 0.203 m in height, and 0.019 m in width. The channel, consisting of initiation, propagation, and test sections, with identical dimesnions was made of aluminum. The schematic illustrating the experimental set-up is presented in Fig. 2, with additional details available in a previous work [16]. The test section of the shock tube features glass walls for visualization. A Z-type schlieren set-up, comprising a slit, a vertical knife-edge, an incandescent 360 Watt lamp, and two concave mirrors, was employed to visualize the propagation of the detonation at the end of the test section by capturing the refraction of light rays. The recording was done at 77481 frames per second, with an exposure time of 0.47 µs and a resolution of 384 $\times$ 288 px$^2$ using a Phantom v1210 camera. Additionally, to visualize the detonation evolution process along the entire test section, 1 m long, a large-scale shadow-graph system was used. This system featured a 2 m $\times$ 2 m retro-reflective screen and a 1000 W Xenon arc lamp. The high-speed camera

Table 1: Experiments test gases with their ideal ZND prediction.

| Test gases | $p_0$ [kPa] | $\Delta_{i,CJ}$ [mm] | $D_{CJ}$ [m s$^{-1}$] |
|---|---|---|---|
| $2H_2/O_2/7Ar$ | 4.1 | 2.8 | 1602 |
| | 7.2 | 1.6 | 1618 |
| $2H_2/O_2/7He$ | 6.6 | 4 | 3588 |
| | 9.3 | 2.8 | 3609 |
| | 15 | 1.6 | 3693 |

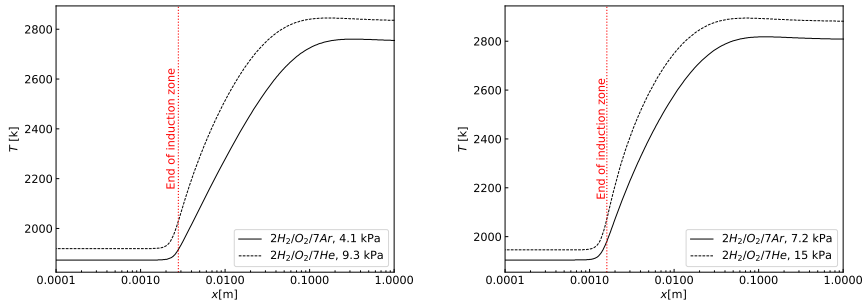


Figure 3: ZND profiles of temperature obtained as a function of distance using the San Diego detailed chemical mechanism [11] at $T_0 = 293$ K.

had a resolution of $1024 \times 272$ px$^2$, a frame rate of 44000, and an exposure time of 0.47 µs.

The two mixtures studied were a stoichiometric mixture of hydrogen-oxygen diluted with argon ($2H_2/O_2/7Ar$) and a stoichiometric mixture of hydrogen-oxygen diluted with helium ($2H_2/O_2/7He$). The initial pressure, $p_0$, of the test gases was adjusted such that the induction zone length, $\Delta_{i,CJ}$, calculated from the ideal Zel'dovich–Von-Neumann–Doering (ZND) model [17, 18, 19], is kept constant between the two different mixtures. Considering the classical correlation between cell width, $\lambda$, and induction zone length [20, 21], ideally, we expect to observe the same cellular structure between the two mixtures. Table 1 shows the experimental test gases, their corresponding induction zone length and Chapman-Jouguet (CJ) detonation speed, $D_{CJ}$, at each initial pressure. Furthermore, Fig. 3 shows the corresponding ZND structures of the two mixtures at different initial pressures. The ideal ZND model prediction is calculated using a Python code working under the framework of SDToolbox [11] and Cantera [22]. The point in the post-shock region in which thermicity is maximum is considered as the end of the induction zone. In the lower pressure cases (4.1 kPa for argon diluted and 9.3 kPa for helium diluted) for each mixture, the measured induction zone length is 2.8-mm, and it is 1.6-mm in the higher pressure cases (7.2 kPa for argon diluted and 15 kPa for helium diluted mixture). Additional experiments were conducted at a lower pressure of 6.6 kPa in the hydrogen-oxygen-helium mixture to reduce the mixture's sensitivity and improve visualization of the detonation propagation.

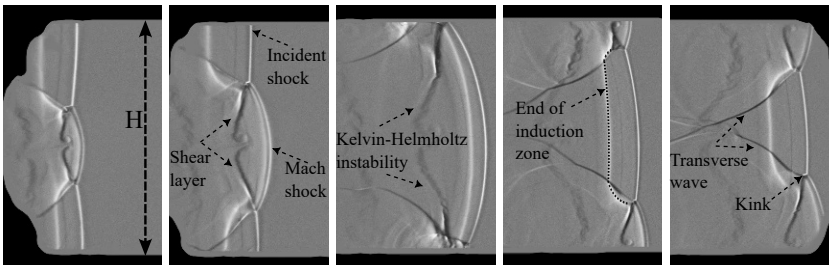


(a) Schlieren imaging of detonation in the mixture of $2H_2/O_2/7Ar$ at $p_0$= 4.1 kPa.

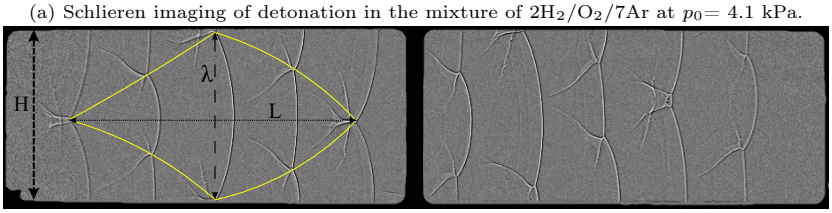


(b) Shadowgraph imaging of detonation in the mixture of $2H_2/O_2/7Ar$ at $p_0$= 4.1 kPa.

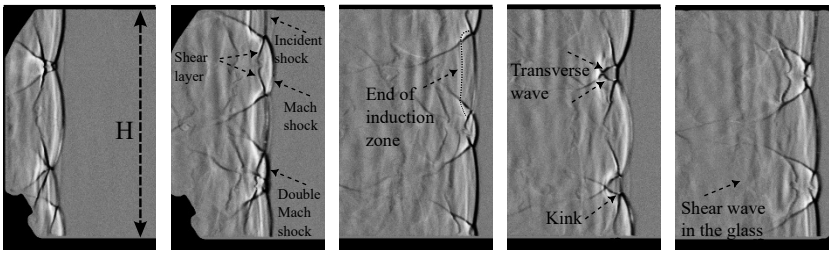


(c) Schlieren imaging of detonation in the mixture of $2H_2/O_2/7He$ at $p_0$= 9.3 kPa.

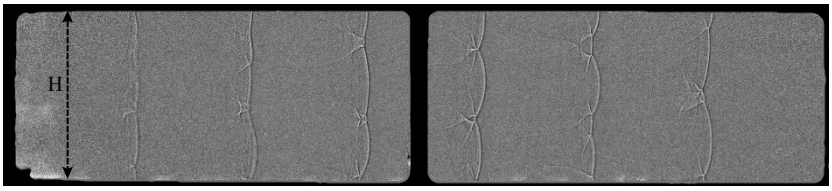


(d) Shadowgraph imaging of detonation in the mixture of $2H_2/O_2/7He$ at $p_0$= 9.3 kPa.

Figure 4: Detonation propagating from left to right in mixtures with a fix induction zone length of $\Delta_i = 2.8$ mm at $T_0 = 293$ K. The visualization length is 300 mm using the Schlieren technique and 1000 mm using the shadowgraph technique. The channel height $H$ is 203 mm, $L$ is the cell length and $\lambda$ is the cell width.

Each mixture was prepared in a separate mixing tank using the method of partial pressures and was left to mix for more than 24 hours. Before filling with driver and test gases, the shock tube was evacuated to a pressure below 80 Pa. Initial ignition of the premixed combustible mixture was achieved using a custom-designed and built high voltage igniter (HVI) [16], which can store up to 1000 J of energy with a deposition time of 2 µs. In all experiments, a stoichiometric mixture of ethylene-oxygen ($C_2H_4/O_2$) was used as the driver gas to initiate detonation. To avoid an over-driven detonation wave in the test section due to the high-pressure driver gas, numerous pilot tests were conducted

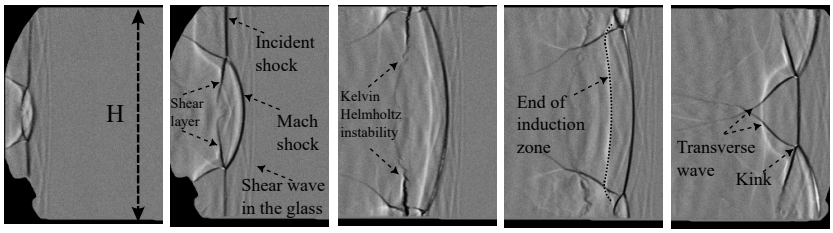


(a) Schlieren imaging of detonation in the mixture of $2H_2/O_2/7He$ at $p_0$= 6.6 kPa.

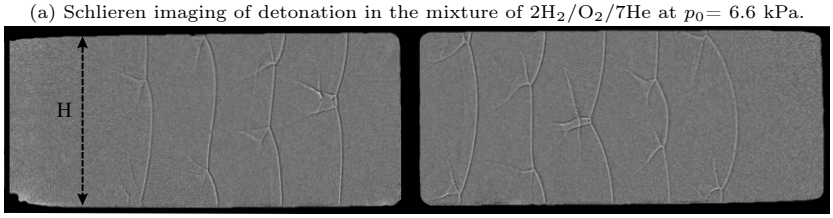


(b) Shadowgraph imaging of detonation in the mixture of $2H_2/O_2/7He$ at $p_0$= 6.6 kPa.

Figure 5: Detonation propagating from left to right in mixture with an induction zone length of $\Delta_i = 4$ mm at $T_0 = 293$ K. The visualization length is 300 mm using the Schlieren technique and 1000 mm using the shadowgraph technique. The channel height $H$ is 203 mm.

to determine the lowest pressure of the driver gas capable of initiating detonation waves. The driver gas filling pressure was consistently maintained at 2.5 times that of the test gas, $p_{\text{driver}} = 2.5 \times p_{\text{test gas}}$, across all experiments as the reference for filling the shock tube. Experiments in the hydrogen-oxygen-argon mixture were repeated five times, and in the hydrogen-oxygen-helium mixture ten times, given the reduction in data obtained from a single experiment due to the higher propagation speed in this system.

Eight high-frequency piezoelectric PCB pressure sensors (models 113B24 and 113B27) were installed on the top wall of the shock tube to record pressure signals and determine propagation speeds using the time-of-arrival method. The sensors resonate at 500 kHz, and the pressure signals during the experiments were recorded at a rate of 1.5 MHz. All pressure gauges used in the experiments have a diameter of 5.5 mm and a maximum error of 1.3%, as determined from the calibration data.

### *2.2. Experimental results*

Figure 4(a) presents the results of schlieren and shadowgraph methods for both argon- and helium-diluted mixtures, with a fixed $\Delta_{i,CJ}$ of 2.8 mm. The schlieren images depict a sequence of frames capturing the detonation wave as it propagates from left to right across a 30 cm distance (matching the diameter of the mirror) at the end of the test section. The superimposed shadowgraph images illustrate the evolution of detonation fronts along the entire 1-meter test section. For the argon-diluted mixture shown in Fig. 4(a), a typical regular cellular structure of the detonation is observed. Detonation exhibits significantly enlarged cellular structure, with the cell height constrained by the channel dimensions, indicating mode locking. At the low initial pressure of 4.1

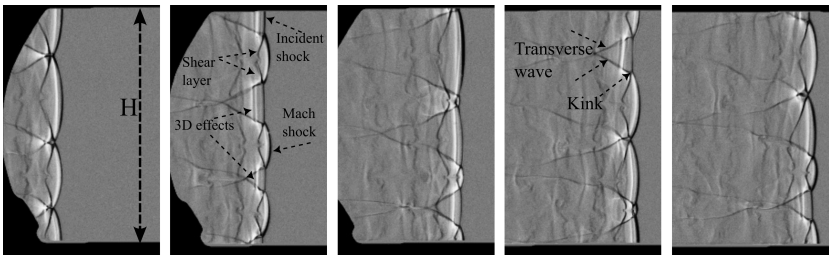


(a) Schlieren imaging of detonation in the mixture of $2H_2/O_2/7Ar$ at $p_0$= 7.2 kPa.

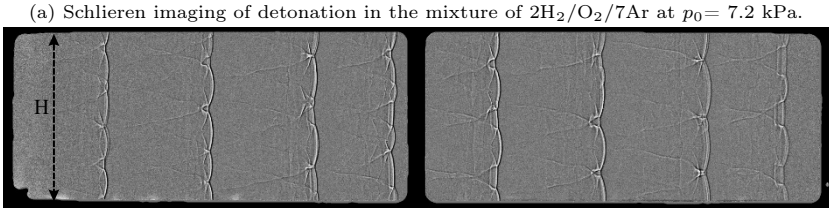


(b) Shadowgraph imaging of detonation in the mixture of $2H_2/O_2/7Ar$ at $p_0$= 7.2 kPa.

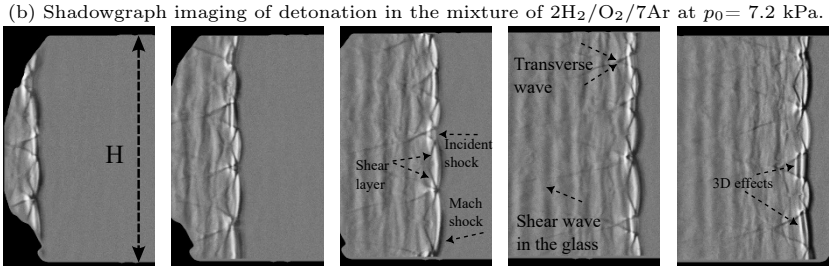


(c) Schlieren imaging of detonation in the mixture of $2H_2/O_2/7He$ at $p_0$= 15 kPa.

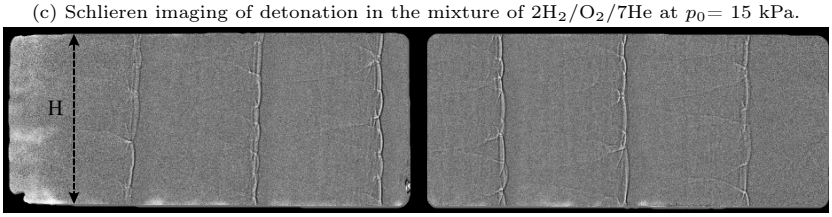


(d) Shadowgraph imaging of detonation in the mixture of $2H_2/O_2/7He$ at $p_0$= 15 kPa.

Figure 6: Detonation propagating from left to right in mixtures with a fix induction zone length of $\Delta_i = 1.6$ mm at $T_0 = 293$ K. The visualization length is 300 mm using the Schlieren technique and 1000 mm using the shadowgraph technique. The channel height $H$ is 203 mm.

kPa, the detonation has relatively large unburned induction zones, visible behind the incident shock. The end of the induction zone is readily established by the marked density gradient in the schlieren photographs associated with the density drop upon exothermicity. The induction zone terminates within a close distance behind the transverse shocks. Vortex structures characteristic of Kelvin–Helmholtz instability are also clearly visible along the shear layer emanating from the triple points. The structure of the triple point is characteristic of the reactive transverse wave configuration previously observed in these regular systems - see Fickett and Davis for review [3].

Figure 4(b) displays the shadowgraph result obtained over a much larger

Table 2: Detonation global propagation speed and cell width measured from the experiments; cell sizes marked with * are mode locked in a single cell configuration in our channel having the same dimension.

| Mixture | $p_0$ [kPa] | $D/D_{CJ}$ | $\lambda$ [mm] |
|---|---|---|---|
| $2H_2/O_2/7Ar$ | 4.1 | $0.84 \pm 0.016$ | 203* |
| | 7.2 | $0.9 \pm 0.01$ | $59 \pm 5$ |
| $2H_2/O_2/7He$ | 6.6 | $0.84 \pm 0.014$ | 203* |
| | 9.3 | $0.88 \pm 0.016$ | $87 \pm 11$ |
| | 15 | $0.92 \pm 0.015$ | $53 \pm 4$ |

length scale. The same dynamics are observed, but some details are not as apparent, such that the location of the end of the induction zone. The results confirm that the single-cell structure is maintained throughout the entire propagation in the test section.

Figure 4(c) shows the detonation structure observed in $2H_2/O_2/7He$ mixture at the same nominal induction length. Although the induction zone length is fixed, the cell sizes are approximately half as large compared to those in the argon-diluted mixtures. The local dynamics appear similar on a length scale of a cell. The induction zone behind the leading shock has the same configuration, terminating at the same scaled distance behind the lead shock and transverse waves.

The results obtained with helium dilution are nevertheless characterized by a system of vertical striations, absent in the argon experiments, as seen in Fig. 4(c). In some cases, this pattern outruns the detonation front (Fig. 5(a)). We believe these are shear waves propagating in glass walls confining the detonation. In the helium mixture, the detonation speed (nominally $D_{CJ} \sim 3600$ m/s) is very close to the shear wave in glass (3764 m/s [23]).

To better visualize the structural details in the helium-diluted mixture, the initial pressure was reduced to 6.6 kPa, resulting in one large detonation cell, as shown in Fig. 5. The structure's details, including the presence of Kelvin-Helmholtz instabilities along the shear layer, are similar to those observed in the single large cell of the argon-diluted mixture, although the instabilities appear less prominent in the helium-diluted mixture.

The global propagation speed, $D$, of the detonation wave over the 0.8 m distance between the first and last pressure sensors in the test section was determined using the time-of-arrival method, as outlined in Table 2. The reported global velocity and its standard deviation represent the average values from repeated experiments under the same conditions (5 trials for argon-diluted mixtures and 10 trials for helium-diluted mixtures). The cell width, $\lambda$, is the average measured from all frames of the schlieren and shadowgraph images across the repeated experiments, along with their standard deviation. For $\Delta_{i,CJ} = 2.8$ mm, the argon-diluted mixture exhibits a 16% velocity deficit and a cell size of 0.203 m, while the helium-diluted mixture shows an 12% velocity deficit with a cell size approximately half as large.

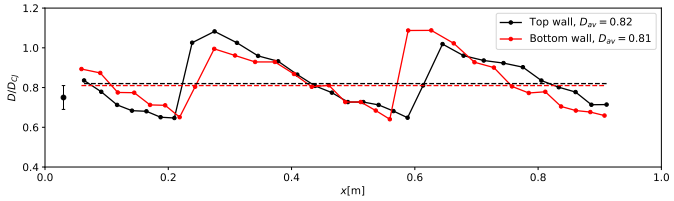


(a) $2H_2/O_2/7Ar$ at $p_0 = 4.1$ kPa

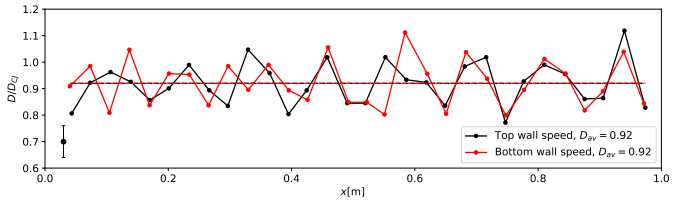


(b) $2H_2/O_2/7Ar$ at $p_0 = 7.2$ kPa

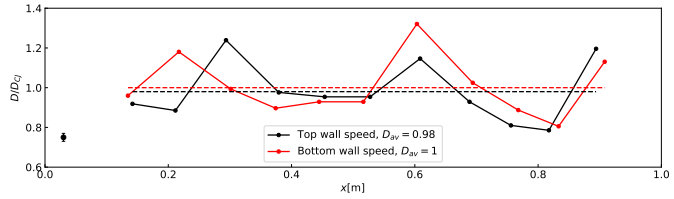


(c) $2H_2/O_2/7He$ at $p_0 = 6.6$ kPa

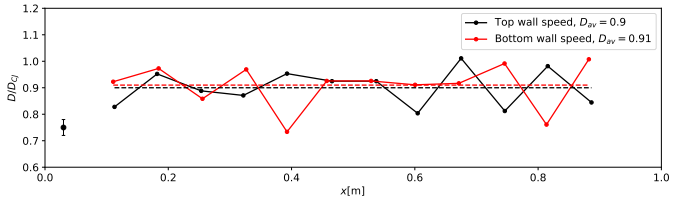


(d) $2H_2/O_2/7He$ at $p_0 = 9.3$ kPa

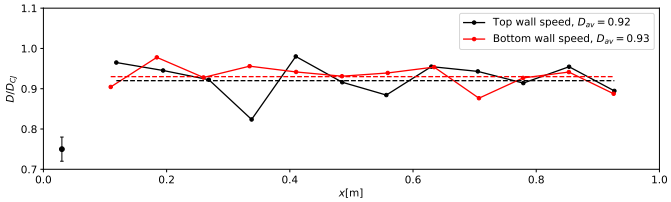


(e) $2H_2/O_2/7He$ at $p_0 = 15$ kPa

Figure 7: Shock speed evolution over the length of the test section, extracted from shadowgraph images.

Figure 6 displays schlieren images of the detonation reaction zone structures at higher initial pressures for both mixtures, with the induction zone length kept constant at $\Delta_i = 1.6$ mm. By increasing the initial pressure, thereby enhanc-

ing the kinetic sensitivity of the mixture, the detonations exhibit considerably smaller cellular structures, with velocity deficits reduced to 10% for the argon-diluted mixture and 8% for the helium-diluted mixture. Although the cell size is slightly smaller in the helium-diluted case, the overall regular cellular structure of the detonations appears similar between the two mixtures. Additionally, possible 3D-like effects in the detonation structure can be observed in both mixtures, as indicated by the presence of duplicate features that do not overlap in the schlieren images.

The locally averaged speeds along both the top and bottom walls were calculated from the shadowgraph images in each experiment, with the distance between every two consecutive frames divided by their time interval, $\Delta t$. The resulting speed profiles are shown in Fig. 7, normalized by the ideal CJ detonation velocity. For the argon-diluted mixture at $p_0 = 4.1$ kPa (Fig. 7(a)), the velocity decays within a single cell from 1.1 to 0.6 and repeats throughout the test section. When the pressure is increased to 7.2 kPa (Fig. 7(b)), the average velocity becomes 0.92 $D_{CJ}$. The overall trends suggest that the detonation propagation speed remains nearly steady at a macro scale within the test section. A similar quasi-steady propagation is observed in the helium-diluted mixture; however, due to the higher propagation speed in this mixture and limitations in the frame rate of the shadowgraph imaging, fewer data points are available (Fig. 7(c), 7(d), 7(e)). We further reconstructed the velocity profile within a single cellular cycle for experiments with sufficiently large cells, following the methodology detailed in Cheevers' thesis [24]. For the $2H_2/O_2/7Ar$ mixture at $p_0 = 4.1$ kPa, data were obtained from a single cell across five repeated experiments. For the $2H_2/O_2/7He$ mixture, data were collected from ten repeated experiments at each pressure (6.6 kPa and 9.3 kPa). An exponential curve was fitted to the data using the equation $\frac{D}{D_{CJ}} = \frac{D_0}{D_{CJ}} \exp\left(-\frac{bx}{L}\right)$, where $D_0$ represents the velocity at the start of the cell, $L$ is the cell length, and $b$ is the decay rate. These results are illustrated in Fig. 8. The highest decay rate within a single cell was observed in the $2H_2/O_2/7Ar$ mixture, where the velocity starts at 1.13 at the beginning of the cell and decays to 0.5 by the end. In the $2H_2/O_2/7He$ mixture, the velocity decreases from 1.05 to 0.65 at $p_0 = 6.6$ kPa and from 1.04 to 0.7 at $p_0 = 9.3$ kPa.

Overall, the experimental measurements of cell width reveal a significant discrepancy in cell size between the two mixtures diluted with argon and helium, despite having the same induction zone length at lower pressures. This raises the question: Is the discrepancy a result of differences in non-equilibrium effects, or is it due to boundary layer losses present in the experiments? In the following sections, we will explore this question by estimating the characteristic vibrational relaxation times and conducting boundary layer loss calculations.

## 3. Vibrational non-equilibrium effect

Recent modelling efforts on non-equilibrium effects in detonations suggest that hydrogen-based detonations may be significantly influenced by the vibrational non-equilibrium of molecules, as vibrational modes are the last to reach

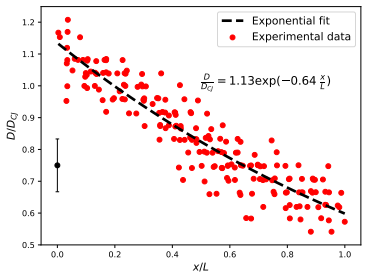


(a) $2H_2/O_2/7Ar$ at $p_0 = 4.1$ kPa

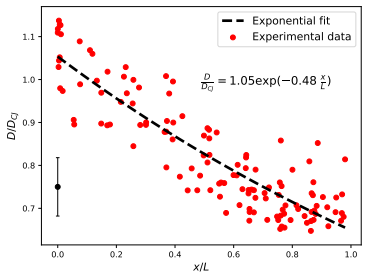


(b) $2H_2/O_2/7He$ at $p_0 = 6.6$ kPa

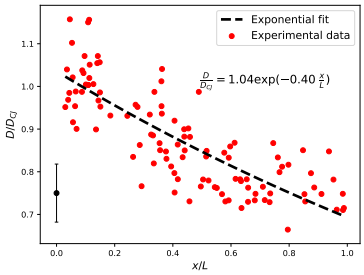


(c) $2H_2/O_2/7He$ at $p_0 = 9.3$ kPa

Figure 8: Shock speed evolution over a detonation cell, with the exponential curve fit shown in black. The experimental data were obtained from repeated experiments conducted 8(a)) 5 times, 8(b)) and 8(c)) 10 times.

equilibrium [25, 4]. This phenomenon could help explain the discrepancies observed in experimentally measured cell sizes, as differences in molecular weight and reduced mass of the bath gases impact molecular collisions and alter relaxation rates [26]. In this section, we aim to estimate the vibrational relaxation time of the $H_2$ and $O_2$ molecules in the two mixtures studied. By using available empirical data, we will calculate the vibrational relaxation time and compare it to the ignition delay times. This comparison will help determine if the discrepancies in the cellular structure of detonation observed in the previous section are due to differences in vibrational non-equilibrium effects of diluents. The vibrational relaxation time of each species, $\tau_i$, in a mixture of $N$ gases can be computed using Eq. (1). This equation takes into account the contributions of collisions with the species itself and other species, based on fitting experimental data using a least squares method [27].

$$\frac{1}{p\tau_i} = \sum_{j=1}^{N} \frac{X_j}{p\tau_{i-j}} \tag{1}$$

where $p$ is the pressure, $\tau_i$ is the vibrational relaxation time of species $i$, $X_j$ is the mole fraction of species $j$ in the mixture and $\tau_{i-j}$ is the vibrational relaxation time of the interaction between species $i$ and $j$. Therefore, the vibrational

Table 3: Vibrational relaxation time and ignition delay time calculations.

| Mixture | $p_0$ [kPa] | $\tau_{H_2}$ [s] | $\tau_{O_2}$ [s] | $\tau_{\text{ignition}}$ [s] | $\frac{\tau_{\text{ignition}}}{\tau_{H_2}}$ | $\frac{\tau_{\text{ignition}}}{\tau_{O_2}}$ |
|---|---|---|---|---|---|---|
| $2H_2/O_2/7Ar$ | 4.1 | $3.05 \times 10^{-6}$ | $8.4 \times 10^{-7}$ | $7.03 \times 10^{-6}$ | 2.3 | 8.4 |
| | 7.2 | $1.63 \times 10^{-6}$ | $4.6 \times 10^{-7}$ | $4 \times 10^{-6}$ | 2.4 | 8.7 |
| $2H_2/O_2/7He$ | 9.3 | $8.1 \times 10^{-7}$ | $1.6 \times 10^{-7}$ | $3.04 \times 10^{-6}$ | 3.7 | 18.5 |
| | 15 | $4.8 \times 10^{-7}$ | $9.7 \times 10^{-8}$ | $1.8 \times 10^{-6}$ | 3.7 | 18.2 |

relaxation time of the hydrogen and oxygen can be estimated as follows:

$$\frac{1}{p\tau_{H_2}} = \frac{X_{H_2}}{p\tau_{H_2-H_2}} + \frac{X_{O_2}}{p\tau_{H_2-O_2}} + \frac{X_{\text{diluent}}}{p\tau_{H_2-\text{diluent}}} \tag{2}$$

$$\frac{1}{p\tau_{O_2}} = \frac{X_{H_2}}{p\tau_{O_2-H_2}} + \frac{X_{O_2}}{p\tau_{O_2-O_2}} + \frac{X_{\text{diluent}}}{p\tau_{O_2-\text{diluent}}} \tag{3}$$

In this study, $X_{H_2} = 0.2$, $X_{O_2} = 0.1$, and $X_{\text{diluent}} = 0.7$. To calculate $p\tau_{H_2-j}$, we use the following empirical relations [27]:

$$\log p\tau_{H_2-j} = AT^{-1/3} - B \tag{4}$$

where $T$ and $p$ represent the post-shock temperature and pressure, respectively. The parameter $A$ takes the values 34.74, 41.35, and 45.09, while the parameter $B$ is 8.686, 8.984, and 8.956 for $H_2$-$H_2$, $H_2$-He, and $H_2$-Ar interactions, respectively. Due to the unavailability of experimental data for the relaxation time of $H_2$-$O_2$, we employed the relaxation time of $H_2$-Ar as a substitute. This approach is justified by the similarity in molecular weights between argon (40 AMU) and oxygen ($O_2$: 32 AMU), as suggested by Taylor et al.[25]. For the relaxation time of the oxygen $p\tau_{O_2-j}$, we use the following equation in which parameters $C$ and $D$ are found empirically [28, 25].

$$p\tau_{O_2-j} = \exp\left[C\left(T^{-1/3} - D\right) - 18.42\right] \tag{5}$$

where $C = 133$ and $D = 0.03$ for $O_2$-$O_2$, and $C = 36$ and $D = 0.000067$ for $O_2$-$H_2$. For the relaxation time of oxygen with diluents ($O_2$-Ar and $O_2$-He), we use the experimental values provided by Millikan and White, where $p\tau_{\text{O}_2-\text{Ar}} = 0.000038$ atm.s and $p\tau_{\text{O}_2-\text{Ar}} = 0.000000509$ atm.s respectively [28].

Table 3 presents the results of the vibrational relaxation time scales for the mixtures of $2H_2/O_2/7Ar$ and $2H_2/O_2/7He$ at initial pressures of the experiments computed at the Von Neumann state of the detonations. Additionally, the ignition delay time, computed using a realistic chemistry ZND calculation for detonation waves in the two mixtures, is also shown to provide a qualitative comparison.

The results show that helium as a diluent reduces the relaxation times of hydrogen and oxygen by approximately 70% as compared to argon. The ratios between ignition delay time and vibrational relaxation time show that in all

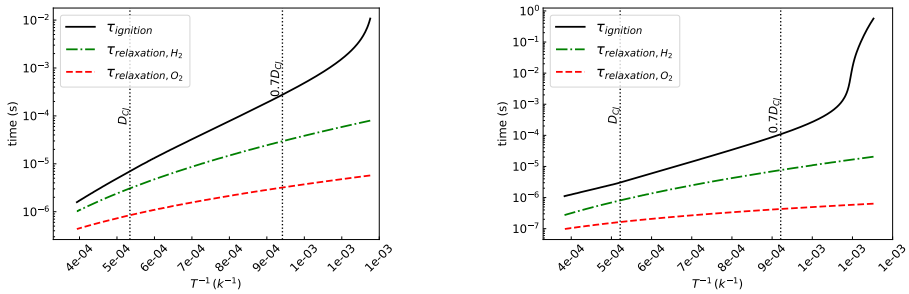


(a) $2H_2/O_2/7Ar$ at $p_0 = 4.1$ kPa

(b) $2H_2/O_2/7He$ at $p_0 = 9.3$kPa

Figure 9: Comparisons of the ignition delay time and vibrational relaxation time versus the post-shock temperature.

cases, relaxation is faster than the induction kinetics. The slowest relaxation is that of $H_2$ in the argon diluted system, which is approximately half the induction time predicted by the ZND model. This may suggest the non-negligible effect of vibrational relaxation, as argued by Taylor et al. [4].

We further calculated how these time scales vary for different shock speeds, since the cellular dynamics are transient. The ignition delay time in the post-shock region was calculated using constant-volume homogeneous reactor of Cantera thermochemical tools [22] and the San Diego mechanism [11]. The results are shown in Figure 9. The temperature dependence of induction kinetics being different, the relaxation rates become an order of magnitude faster than the induction kinetics at the low speed stages of the detonation structure. Owing to the lower sensitivity of relaxation rates, calculations of induction delays along particle paths accounting for the expansion associated with shock non-steadiness would further exacerbate this discrepancy [24]. It can thus be argued that induction time becomes much larger than relaxation times once their sensitivity to flow non-steadiness prevalent in cellular dynamics is incorporated.

For the same induction zone length, we find that the helium diluted system is more reactive. It has a lower velocity deficit and smaller cells than in the argon system. This trend cannot be reconciled by the vibrational relaxation explanation. The relaxation is slower with argon, and hence one would expect at larger translational temperature in the induction zone and a speed up in reactivity. This is not the case in the experiments, where the opposite trend is observed.

## 4. Numerical modelling of boundary layer losses

### *4.1. Model formulation*

We proceeded by establishing if the results of our experiments, namely anomalous differences in cell sizes and velocity deficits for the same induction zone length, are compatible with boundary layer losses. To investigate this hypothesis, we employ the method proposed by Xiao et al. [5], who introduced a

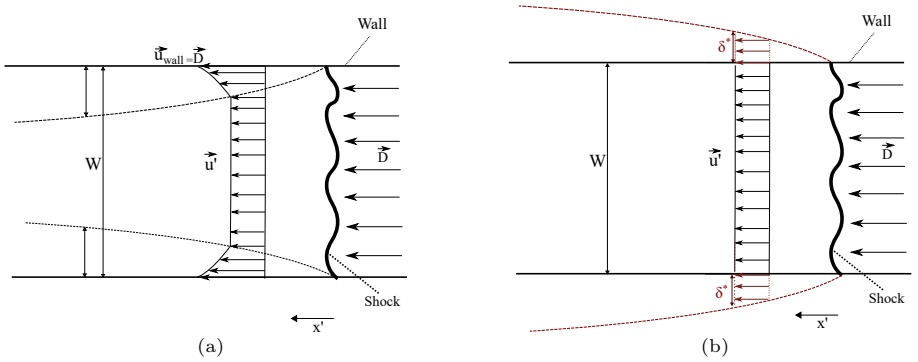


Figure 10: The steady flow in the post-shock region of a detonation wave in the shock-attached reference frame. The dashed lines inside the walls (a) indicate the outer edges of the boundary layer ($\delta$) and the dashed lines outside of the walls (b) indicate the outer edges of the displaced boundary layer ($\delta^\star$). $W$ is the channel thickness in the z-direction, $D$ is the detonation speed, $x'$ is the distance in the post-shock region in the shock-attached frame and $u'$ is the post-shock region velocity.

quasi-2D model to reconstruct the three-dimensional cellular structures of detonation waves in narrow channels. Their model incorporates an area divergence term into the reactive Euler equations to account for boundary layer losses in the third dimension, as illustrated in Fig. 10. Figure 10(a) shows the velocity gradients near the walls caused by the presence of a boundary layer in contrast to the uniform flow observed in the core region. Figure 10(b) depicts an equivalent approach in which the effect of the boundary layer losses are accounted for by incorporating the flow divergence in the third dimension due to the negative boundary layer displacement thickness, $\delta^*$. The area divergence term is evaluated based on Mirels' laminar boundary layer solution [29]. An improvement on the account for flow acceleration is the only difference from the treatment used by [5]. This was first proposed by the authors in our preliminary work [7] and very recently further validated by Smith et al. [10] using a higher fidelity chemical model.

We briefly review the model formulation - for details, see [5]. The governing equations are the reactive two-dimensional Euler equations supplemented by a source term to model the boundary layer effects, outlined as follows:

$$\frac{\partial \rho}{\partial t} + \frac{\partial (\rho u)}{\partial x} + \frac{\partial (\rho v)}{\partial y} = -\rho \frac{1}{A}\frac{DA}{Dt} \tag{6}$$

$$\frac{\partial \rho u}{\partial t} + \frac{\partial (\rho u^2 + p)}{\partial x} + \frac{\partial (\rho uv)}{\partial y} = -\rho u \frac{1}{A}\frac{DA}{Dt} \tag{7}$$

$$\frac{\partial \rho v}{\partial t} + \frac{\partial (\rho uv)}{\partial x} + \frac{\partial (\rho v^2 + p)}{\partial y} = -\rho v \frac{1}{A}\frac{DA}{Dt} \tag{8}$$

$$\frac{\partial (\rho e)}{\partial t} + \frac{\partial (\rho eu + pu)}{\partial x} + \frac{\partial (\rho ev + pv)}{\partial y} = -(\rho e + p)\frac{1}{A}\frac{DA}{Dt} - Q\dot{\omega}_R \tag{9}$$

$$\frac{\partial(\rho Y)}{\partial t} + \frac{\partial(\rho u Y)}{\partial x} + \frac{\partial(\rho v Y)}{\partial y} = -\rho Y \frac{1}{A}\frac{DA}{Dt} + \dot{\omega}_R \tag{10}$$

where $\rho$, u, v, A, p, Q, Y, and $\dot{\omega}_R$ represent the density of the mixture, velocity in the x-direction, velocity in the y-direction, cross-sectional area, pressure, heat release, mass fraction, and the rate of mass production of the individual reactant R. The total energy is defined as the sum of the sensible energy plus the kinetic energy, $e = \frac{p/\rho}{\gamma-1} + \frac{1}{2}(u^2+v^2)$ where $\gamma$ is the ratio of specific heats.

The viscous boundary layer developing behind a detonation wave leads to an apparent cross-sectional increase to $A = W + 2\delta^*$ due to the negative mass displacement thickness $\delta^*$, as illustrated in Fig. 10. The rate of lateral strain of a fluid element is thus

$$\frac{D(\ln A)}{Dt} \cong \frac{2}{W}\frac{D\delta^*}{Dt} \tag{11}$$

A special treatment is required for accounting for the boundary layer growth and its negative displacement thickness in non-uniform flow. In the absolute frame of reference of the calculations, the flow in the reaction zone decelerates strongly while it expands during the exothermic events. To address this, we model the boundary layer growth in terms of the time elapsed since having crossed the shock, since $\delta \sim \sqrt{t_{elapsed}}$ will continue to offer a good approximation for boundary layer growth even for non steady or steady accelerating flow. We also assume the displacement thickness proportional to the boundary layer thickness, a reasonable assumption. This amounts to generalizing the expression for the negative displacement thickness found by Mirels [29] for laminar flow from

$$\delta^* = K_M \sqrt{\nu \frac{x'}{u'}} \tag{12}$$

to

$$\delta^* = K_M \sqrt{\nu \int_0^{x'} \frac{dx'}{u'(x')}} = K_M \sqrt{\nu t_{elapsed}} \tag{13}$$

in which Mirels' constant $K_M$ can be calculated separately, as for steady flow, and depends on the mixture composition and post shock state. The detailed computation of this constant is available in the work of Xiao and Radulescu [30]. In the case of $2H_2/O_2/7Ar$ mixture, the determined value of $K_M$ is approximately 4, while for the mixture of $2H_2/O_2/7He$, the value of $K_M$ is found to be 3.8.

Using (13), the lateral strain rate required in the computations is

$$\frac{D(\ln A)}{Dt} \cong \frac{K_M}{W}\sqrt{\frac{\nu}{t_{elapsed}}} \tag{14}$$

This simple correction recovers approximately the boundary layer growth in steady flow with non-zero pressure gradients. An observer following an accelerating flow due to a local favourable pressure gradient sees a smaller boundary layer than an observer having reached the same position having propagated at

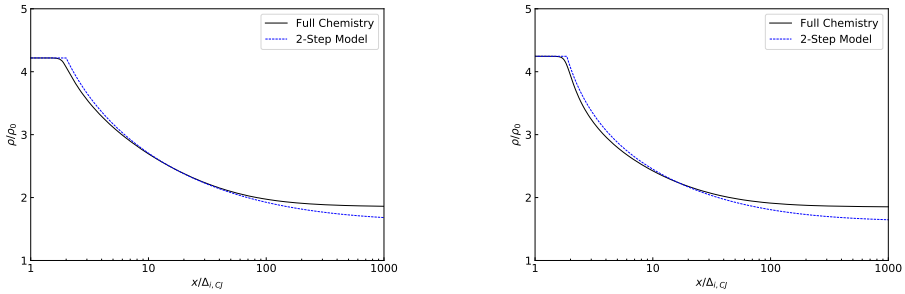


(a) $2H_2/O_2/7Ar$ at $p_0 = 4.1$ kPa

(b) $2H_2/O_2/7Ar$ at $p_0 = 9.3$ kPa

Figure 11: Calibration of the two-step model based on detailed chemistry. $\rho$ represents the post-shock density, $\rho_0$ is the initial density, $x$ denotes the distance, and $\Delta_{i,CJ}$ is the induction zone length.

Table 4: Calibrated non-dimensional parameters for the two-step model from the detailed chemistry.

| Mixture | $p_0$ [kPa] | $\gamma$ | $E_a/RT_0$ | $Q/RT_0$ | $k_i$ | $k_r$ | $\alpha$ | $\beta$ | $\nu$ |
|---|---|---|---|---|---|---|---|---|---|
| $2H_2/O_2/7Ar$ | 4.1 | 1.5 | 31.1 | 11.5 | 45.5 | 0.08 | 1.2 | 1 | 1.6 |
| $2H_2/O_2/7He$ | 9.3 | 1.5 | 23.9 | 11.9 | 12.2 | 0.13 | 1.2 | 1 | 1.5 |

a constant speed. This is due to the time elapsed since crossing the shock being smaller for the observer that reached that location faster.

Since the flow is non-steady, the time elapsed is a property of a given fluid particle, i.e., the time elapsed since the wall started pulling away from that particle, as in Rayleigh's suddenly accelerating plate problem. The only information required in the calculation is thus the time at which a fluid particle has crossed the shock $t_s$, since $t_{elapsed} = t - t_s$. Since each particle retains its value of $t_s$, this is updated only once, when passing a shock, and then evolved as a passive scalar advected with the flow, satisfying:

$$\frac{\partial t_s}{\partial t} + u\frac{\partial t_s}{\partial x} = 0 \tag{15}$$

The same model was suggested first by Xiao et al. [5] in their write-up. Unfortunately, their calculations used a non-advected evolution of $t_s$. The incorrect write-up was not noted at the time. As we will show below, the presently suggested advected form does not require the artificial re-tuning of the Mirels' constant, as performed by Xiao et al. [5] in order to match experiment. This was also communicated subsequent to our first dissemination of our finding [7] by Smith et al. [10], who also found it to be better approximation.

To model the chemical kinetics, the two-step chain-branching reaction model (the thermally neutral induction zone followed by the exothermic reaction zone) was employed and the non-dimensional parameters for the two-step model were calibrated from the detailed chemistry by using the San Diego chemical reaction mechanism [11] and Shock and Detonation Toolbox (SDToolbox) [31], shown in

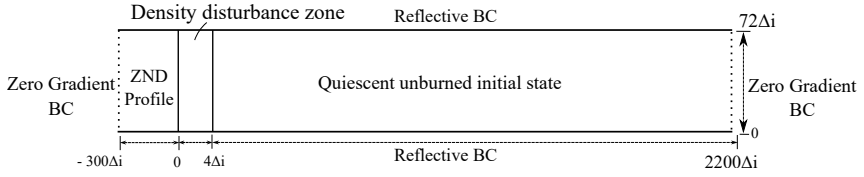


Figure 12: Initial and boundary conditions for the 2D detonation propagation simulation, where $72\Delta_{i,CJ}$ corresponds to the actual channel height of 203 mm in the experiment.

Fig. 11. The induction and reaction transport equations can be formulated as Eq. (16) and (17).

$$\frac{\partial(\rho\lambda_i)}{\partial t} + \frac{\partial(\rho u\lambda_i)}{\partial x} + \frac{\partial(\rho v\lambda_i)}{\partial y} = -\rho\lambda_i \frac{1}{A}\frac{DA}{Dt} - \mathcal{H}(\lambda_i)k_i\rho^{\alpha+1}exp(-\frac{Ea}{RT}) \quad (16)$$

$$\frac{\partial(\rho\lambda_r)}{\partial t} + \frac{\partial(\rho u\lambda_r)}{\partial x} + \frac{\partial(\rho v\lambda_r)}{\partial y} = -\rho\lambda_r \frac{1}{A}\frac{DA}{Dt}[1 - \mathcal{H}(\lambda_i)]k_r\rho^{\beta+1}\lambda_r^{\nu} \quad (17)$$

The progress variable for the induction zone, $\lambda_i$, has a value of 1 ($\mathcal{H}(\lambda_i) = 1$) at the reactants and 0 ($\mathcal{H}(\lambda_i) = 0$) at the induction zone's termination. Correspondingly, the reaction progress variable, $\lambda_r$, holds a value of 1 in the unburned zone and 0 in the burned products. $k_i$ and $k_r$ represent rate constants, $\nu$ represents the reaction order, and $\alpha$ and $\beta$ stand as additional empirical reaction order parameters. The values of $\beta$, $\alpha$ and $\nu$ were chosen to align with the detailed chemistry ZND structure, which is readily discernible from the density profile illustrated in Fig. 11.

Table 4 shows the non-dimensional parameters for the two-step chemistry model for the two different mixtures. The post-shock isentropic exponent of the CJ detonation was represented by $\gamma$, and the heat release $Q$ was obtained using the perfect gas relation to ensure accurate recovery of the Mach number [3]. The symbol $E_a$ represents the activation energy that impacts the temperature-dependent behaviour of the induction zone duration. It was calculated using the logarithmic derivative of the ignition delay time with respect to the inverse of post-shock temperature.

In this investigation, the normalization scales for the analysis include the initial state variables ($p_0$, $\rho_0$) and the ideal ZND induction zone length, $\Delta_{i,CJ}$. A second-order-accurate exact Godunov solver [32] with adaptive mesh refinement [5] is used to solve the governing equations. The induction zone length is kept constant for both helium and argon experiments. For reference, the induction zone length is 0.0028 m. The channel height is non-dimensionalized by the induction zone length. To make sure that we cover the length of the shock tube, 3.4 m, a domain length of $2500\Delta_{i,CJ}$ is considered for the simulations. In these simulations, the detonation propagates from left to right, with reflective boundary conditions imposed on the top and bottom sides, and zero-gradient boundary conditions applied to the left and right ends, illustrated in Fig. 12.

For the numerical resolution, the coarsest grid size was set to $1/2\,\Delta_{i,CJ}$, and the finest grid size was set to $1/16\,\Delta_{i,CJ}$. Since we use a two-step chemistry

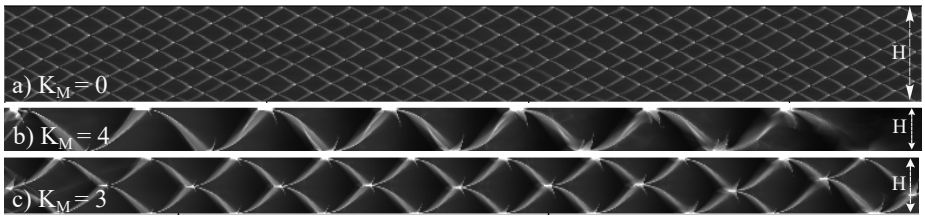


Figure 13: The recorded maximum energy release rates of detonations in the mixture of $2H_2/O2/7Ar$ at $p_0 = 4.1$ kPa and $T_0 = 293$ K. The cell size and mean propagation speeds are: (a) $D/D_{\mathrm{CJ}} = 1$, $\lambda = 37\,\mathrm{mm}$, (b) $D/D_{\mathrm{CJ}} = 0.77$, $\lambda = 406\,\mathrm{mm}$, (c) $D/D_{\mathrm{CJ}} = 0.83$, $\lambda = 203\,\mathrm{mm}$. The channel height $H$ is 72 $\Delta_{i,CJ}$, corresponding to a shock tube channel height of 203 mm.

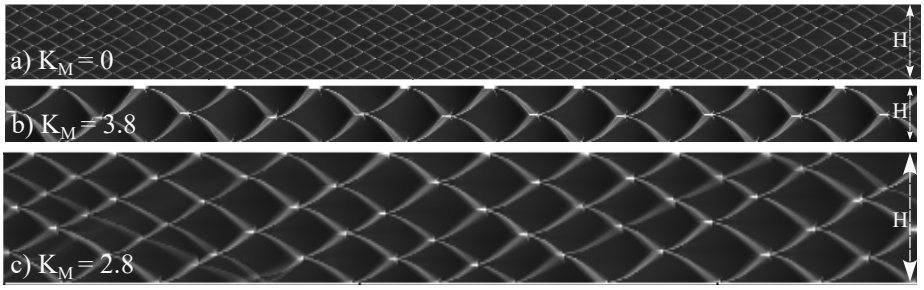


Figure 14: The recorded maximum energy release rates of detonations in the mixture of $2H_2/O2/7He$ at $p_0 = 9.3$ kPa and $T_0 = 293$ K. The cell size and mean propagation speeds are: (a) $D/D_{\mathrm{CJ}} = 1$, $\lambda = 37\,\mathrm{mm}$, (b) $D/D_{\mathrm{CJ}} = 0.81$, $\lambda = 203\,\mathrm{mm}$, (c) $D/D_{\mathrm{CJ}} = 0.88$, $\lambda = 81\,\mathrm{mm}$. The channel height $H$ is 72 $\Delta_{i,CJ}$, corresponding to a shock tube channel height of 203 mm.

model similar to that employed by Xiao [33] the 5 levels of mesh refinement chosen in this study have been verified as sufficient.

### *4.2. Comparison with experiment*

Figure 13 shows the numerically tracked maximum energy release rates for detonations in the mixtures of $2H_2/O_2/7Ar$ at $p_0 = 4.1$ kPa. This corresponds to the open shutter photograph in experiments. The simulation results indicate that in the absence of losses ($K_M = 0$), the ideal CJ detonation exhibits five stable cells across the channel, corresponding to $\lambda_{CJ} = 37$ mm. However, when boundary layer losses are included, using the nominal Mirels constant, $K_M \approx 4.0$, only a single-head detonation propagates in the channel, with a higher velocity deficit than measured in the experiments. The present simulations, however, show the reduction in $K_M$ by 25%, to a value of $K_M = 3$ can accurately replicate the experimental results in terms of cell size and velocity deficit. Recent work by Smith et al. [10] found that using more realistic chemical model yielded good agreement with the experiment. We conclude that viscous losses capture the experiment well, within the accuracy of the known chemical kinetics and modelling assumptions.

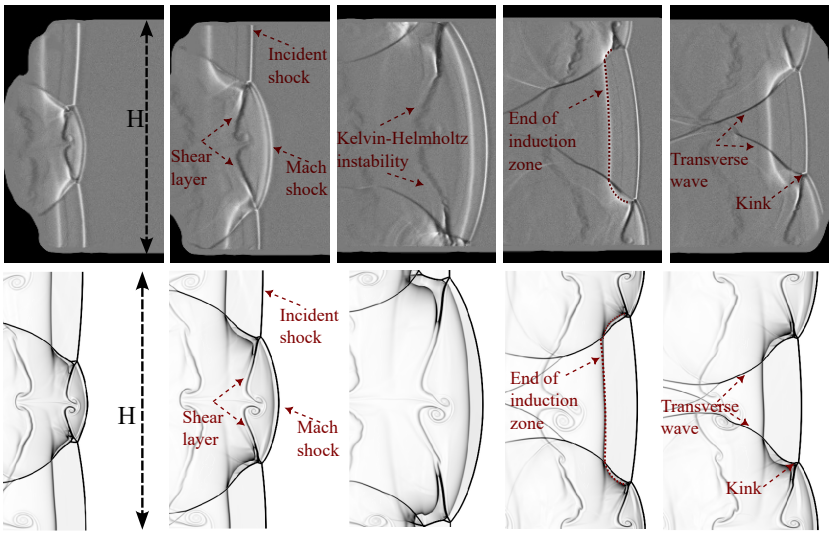


(a) $2H_2/O_2/7Ar$ at $p_0 = 4.1$ kPa

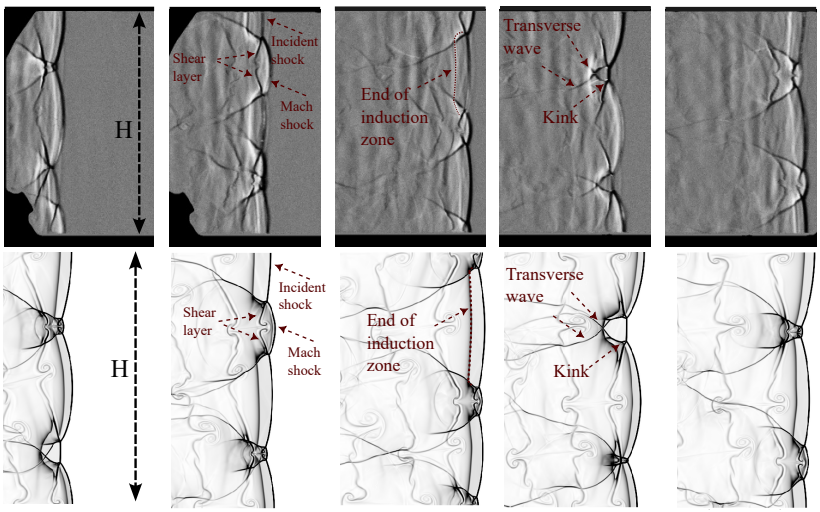


(b) $2H_2/O_2/7He$ at $p_0 = 9.3$kPa

Figure 15: Comparisons of the gradient of the density for experiments and simulations with $\Delta_{i,CJ} = 2.8$ mm. The first and third rows show the schlieren photographs from the experiment, while the second and fourth rows depict the quasi-2D simulation. $H$ is the channel height of 203 mm.

A similar conclusion can be made from the calculations of the helium dilution case at $p_0 = 9.3$ kPa, as shown in Fig. 14. The nominal $K_M = 3.8$ results in a larger cell size and velocity deficit, while a $K_M = 2.8$ better matches the experimental observations.

It is worthwhile making a more direct comparison between the cellular struc-

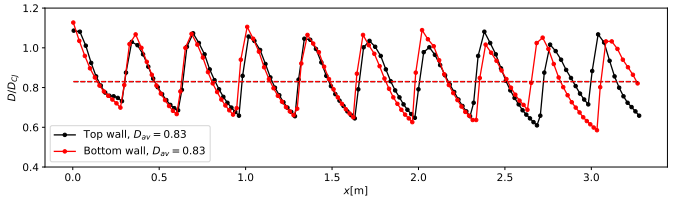


(a) $2H_2/O_2/7Ar$ at $p_0 = 4.1$ kPa

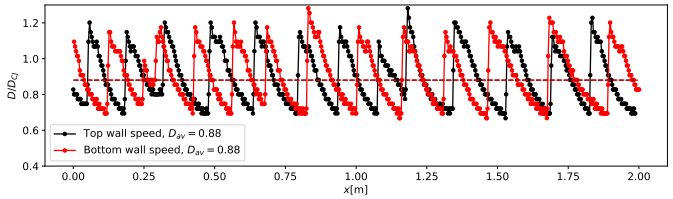


(b) $2H_2/O_2/7He$ at $p_0 = 9.3$ kPa

Figure 16: Shock speed evolution over the length of the ten repeated cells, extracted from the top and bottom walls of the numerical simulation.

ture obtained numerically and experimentally. Figure 15 shows evolution of the density gradients obtained in the experiments and in the simulations for the argon and helium mixtures. The numerical simulations use the adjusted values of $K_M$. The intricate dynamics of cellular patterns, such as unburned gas trailing the incident shock, the shear layer behind the Mach shock, and the kinks in transverse waves, are accurately reproduced when compared to experimental observations in both mixtures with the same fidelity. This suggests the robustness of the proposed quasi-2D formulation as well as the two-step chemistry model in simulating the real detonations in experiments.

The average detonation speed measured in ten repeated cells on the top and bottom walls of the numerical simulation is $D/D_{CJ}$=0.83 for argon diluted and 0.88 for helium diluted mixtures; these are in very good agreement with global velocity measured in the experiments (0.84 for argon diluted and 0.88 for helium diluted). Figure 16 further illustrates the velocity evolution within the ten repeated cells from the top and bottom walls of the simulation, showing that steady detonation waves were achieved at the macro-scale in both mixtures, consistent with the experimental velocity profile.

We further present the temporal velocity evolution within a single cell from the 2D simulation, overlaid on the experimental data for a corresponding cell, as shown in Fig. 17. These results show good quantitative agreement between the experiment and simulation, with the maximum velocity is predicted to be 1.2 at the beginning of the cell, decreasing to 0.6 at the end for the argon-diluted mixture, and from 1.15 to 0.7 within a single detonation cell for the helium-diluted mixtures.

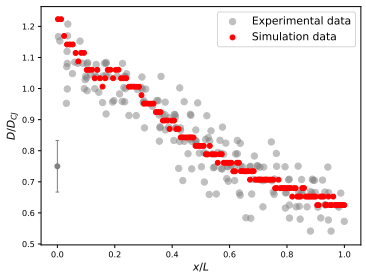


(a) $2H_2/O_2/7Ar$ at $p_0 = 4.1$ kPa

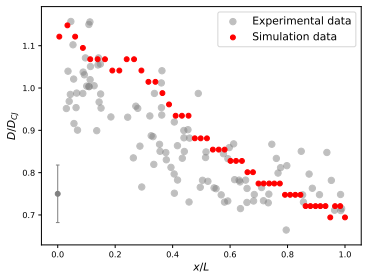


(b) $2H_2/O_2/7He$ at $p_0 = 9.3$ kPa

Figure 17: Comparison of shock speed evolution over a detonation cell between simulation (red circles) and experimental data (gray circles). The error bars represent the experimental uncertainty.

### *4.3. The steady ZND structure and viscous scaling*

We have also compared our numerical and experimental results with the predictions made from the steady ZND model supplemented by the lateral flow losses described above. This model permitted us to determine the loss parameter that can permit scaling the results with the different diluents.

The steady wave structure is evaluated in the framework of one-dimensional ZND detonations with flow divergence to the boundary layers [6, 34]. The Euler governing equations for the steady, inviscid, reactive quasi-1D flow in the shock-attached reference frame are:

$$\frac{dp}{dt'} = -\rho u'^2 \frac{\dot{\sigma} - \dot{\sigma}_A}{1 - M^2} \tag{18}$$

$$\frac{du'}{dt'} = u' \frac{\dot{\sigma} - \dot{\sigma}_A}{1 - M^2} \tag{19}$$

$$\frac{d\rho}{dt'} = -\rho \frac{\dot{\sigma} - M^2 \dot{\sigma}_A}{1 - M^2} \tag{20}$$

$$\frac{dx'}{dt'} = u' \tag{21}$$

where $p$, $\rho$, and $u'$ are the mixture pressure, density, and the post-shock flow velocity in the shock-attached frame of reference, respectively, and $M$ is the Mach number of the flow. For a mixture of ideal gases, the thermicity reduces to the equation:

$$\dot{\sigma} = \sum_{i=1}^{N_s} \left( \frac{W}{W_i} - \frac{h_i}{c_p T} \right) \frac{dY_i}{dt'} \tag{22}$$

in this equation, $W_i$, $Y_i$, and $h_i$ are the molecular weight, mass fraction, and enthalpy of the $i^{th}$ species, respectively; $W$ is the mean molecular weight, $c_p$ is

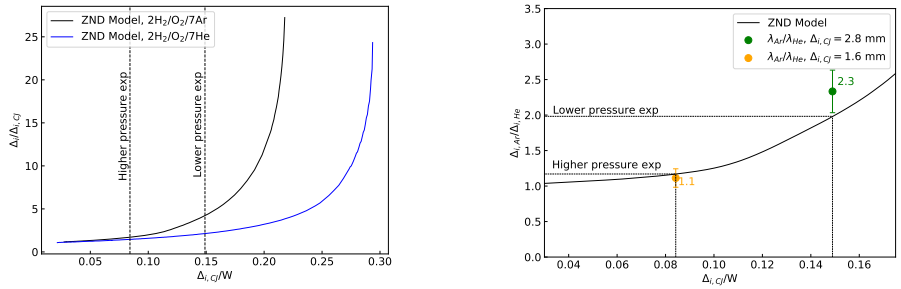


(a) (b)

Figure 18: a) The evolution of the non-dimensional induction zone length from the ZND model with losses versus the inverse of the channel width, $W$. b) The ratio of the induction zone length for argon-diluted and helium-diluted mixtures from the ZND model with losses versus the inverse of the channel width. $\lambda$ represents the cell width ratio obtained from experiments (Table 2) and $\Delta_{i,CJ}$ is the channel width, measuring 19 mm.

the specific heat, and $T$ is the temperature of the mixture. The kinetics for the evolution of the mass fractions, $Y_i$, of each species is given by:

$$\frac{dY_i}{dt'} = \frac{W_i \dot{\omega}_i}{\rho} \tag{23}$$

where $\dot{\omega}_i$ is the molar production rate of species $i$. The lateral strain rate of the flow in the channel is calculated by:

$$\dot{\sigma}_A = u' \frac{1}{A} \frac{dA}{dx'} \tag{24}$$

the term $\frac{1}{A}\frac{dA}{dx'}$ was previously defined in Eq. (14) A custom Python code was developed for the real gas calculations, utilizing Cantera's framework to compute the thermo-chemical data [22] and the Shock and Detonation Toolbox [31] to evaluate the shock jump conditions. The system of ODEs was then solved using SciPy's variable-coefficient ODE solver (VODE). For each mixture and initial state, the detonation speed and reaction zone structure were obtained by a shooting method for the speed eigenvalue. The correct speed was such that the generalized CJ condition was satisfied inside the reaction zone, where the flow becomes sonic as the rate of energy release ($\dot{\sigma}$) balances the rate of the loss ($\dot{\sigma}_A$). We measured the induction zone length using the ZND model with boundary layer losses ($\Delta_i$) and without them ($\Delta_{i,CJ}$), as shown in Fig. 18. In Fig. 18(a), the black line represents the argon-diluted mixture, while the blue line corresponds to the helium-diluted mixture. The divergence between the two lines increases as the channel thickness decreases, consistent with the observed differences in cell sizes between the two mixtures, particularly in lower pressure experiments. For a clearer comparison, Fig. 18(b) presents the ratio of the induction zone length of the argon-diluted mixture to that of the helium-diluted mixture, as calculated by the ZND model with losses, alongside the

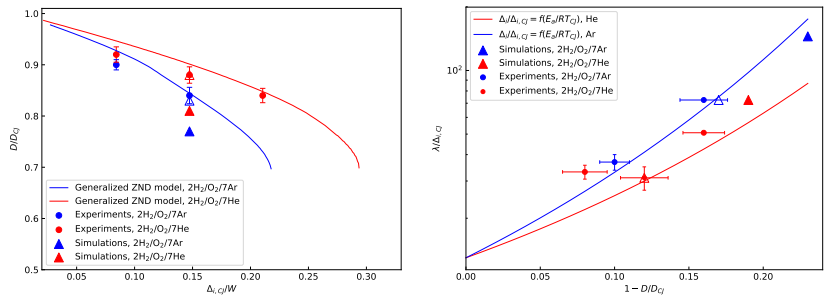


(a) (b)

Figure 19: a) The mean propagation velocity in argon and helium mixtures measured experimentally (symbols) and calculated from the ZND model with losses (lines); the abscissa is the inverse channel thickness normalized by the induction zone length at CJ condition. b) Comparisons of the measured velocity deficit and cell sizes from quasi-2D simulation with experiments. The solid line is the sensitivity of induction kinetics with temperature. Closed triangles represent the simulation results using the nominal $K_M$ values (4 for the argon mixture and 3.8 for the helium mixture), while open triangles indicate the results with adjusted values (3 for the argon mixture and 2.8 for the helium mixture).

experimentally measured cell widths. The orange circle is the cell width ratio in both argon and helium dilution in the higher-pressure experiment and the green circle is related to the same ratio in the lower-pressure experiments. The error bars indicate the standard deviation calculated from repeated experiments conducted in the same mixture under the same initial pressure conditions. This graph shows that the ZND model with losses can predict the experimental result with good accuracy. This result explains why the cell width in the lower-pressure experiments is not precisely the same, and it is because of the higher losses near the limit.

Figure 19(a) presents the numerically calculated velocity deficits for both mixtures as a function of the non-dimensionalized CJ induction zone length, alongside velocity deficits measured from experiments and 2D simulations. Overall, considering the experimental, simulation, and ZND model data, the velocity deficits in the lower-pressure experiments ($\Delta_{i,CJ}/W = 0.15$) are consistently higher compared to those in the higher-pressure experiments ($\Delta_{i,CJ}/W = 0.084$). As shown in the figure, the adjusted values closely match the experimental data, while the nominal values alter the velocity deficit prediction by 8%. Although the ZND model does not predict the experimental results as accurately as the 2D simulations, its predictions still fall within the experimental uncertainty. The discrepancy between the 2D simulations and the ZND model may be attributed to the influence of the cellular structure.

Figure 19(b) illustrates the dimensionless relationships, represented by the solid line, that describe the velocity deficit in relation to the detonation cell size ($\lambda$) and the CJ induction zone length ($\Delta_{i,CJ}$). From the 2D simulation results, we found that $\frac{\lambda_{CJ}}{\Delta_{i,CJ}} = 13$ in the lower-pressure experiments where $\Delta_{i,CJ} = 2.8$ mm and $\lambda_{CJ} = 37$ mm. Using Eq. 12 from [5], $\frac{\Delta_i}{\Delta_{i,CJ}} \approx \frac{\lambda}{\lambda_{CJ}} \approx$

$\exp\left(\frac{2E_a}{RT_{CJ}}(1-\frac{D}{D_{CJ}})\right)$, we compute $\frac{\lambda}{\lambda_{CJ}} \times \frac{\lambda_{CJ}}{\Delta_{i,CJ}} = \frac{\lambda}{\Delta_{i,CJ}}$, which are displayed as solid lines in the figure. The adjusted 2D simulation accurately predicts both the cell size and velocity deficit observed in the both mixtures. However, using the nominal values of $K_M$ results in an overestimation of the cell sizes by a factor of two.

To summarize, the overall comparison between experiment and simulations suggest that velocity deficits, cell size and overall reaction structure can be well captured by a quasi-2D CFD model with incorporation of viscous losses. Perfect agreement can be obtained by modifying one of the model closed parameters by 25 %. This margin of error has been claimed to be reduced by Smith et al. [10], by using a higher fidelity thermo-chemical model. This success is quite remarkable, and suggests the viscous losses dominate the observed effects.

### *4.4. Theoretical viscous scaling law*

A detailed analysis of the response of detonations to lateral flow divergence due to laminar boundary layers is presented in the appendix. We conducted a perturbation analysis in the limit of a high activation energy, assuming a square wave detonation, following the main ideas of He and Clavin [35]. The result of this analysis shows that the velocity deficit parameter

$$\phi = \frac{D_{CJ} - D}{\epsilon D_{CJ}} \tag{25}$$

depends on the loss parameter

$$\zeta = \frac{4\gamma^2}{\gamma+1}\frac{1}{\epsilon}\frac{\Delta_{i,CJ}}{W}K_M\sqrt{\frac{\mu}{\rho_0 D_{CJ}\Delta_{i,CJ}}} \tag{26}$$

by

$$\phi e^{-\phi} = \zeta \tag{27}$$

where $\epsilon$ denotes the inverse of the non-dimensional activation energy. This has the characteristic inverted C shape with a maximum loss parameter permitting self-sustained propagation given by $\zeta^* = e^{-1}$. The results of Eq. (27) using $\gamma = 1.5$ and $\frac{1}{\epsilon} = 4.4$ for the mixtures of this study is the C-shaped black line in Fig. 20, which illustrates the relationship between the velocity deficit and the loss term. The results of the analysis and the identification of the loss parameter now permits us to collapse the experimental and numerical data for the two mixtures. The successful scaling relies on the square root of the inverse Reynolds number $\sqrt{\frac{\mu}{\rho_0 D_{CJ}\Delta_{i,CJ}}}$ in the loss parameter $\zeta$. Fig. 20 shows that the results of the experiments collapse on the same curve under viscous loss scaling. This is perhaps the most convincing argument reconciling the results in argon and helium under viscous scaling. This good scaling suggests that possible modifications due to non-equilibrium effects are negligible, as they would otherwise break this scaling.

While experiments in helium and argon collapse within the accuracy of the speed measurement, the helium data appears to indicate slightly higher speeds,

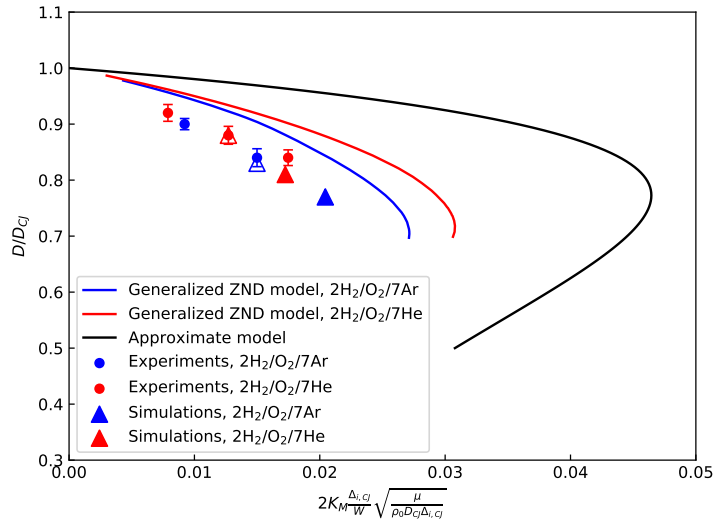


Figure 20: The evolution of non-dimensional detonation speeds as a function of the loss term, compared with experimental data, 2D simulations, and the generalized ZND model. Closed triangles represent the simulation results using the nominal $K_M$ values (4 for the argon mixture and 3.8 for the helium mixture), while open triangles indicate the results with adjusted values (3 for the argon mixture and 2.8 for the helium mixture).

hence more sensitive mixtures. This again is not compatible with the vibration relaxation explanation, as the reactants in the presence of helium relax faster and the kinetics would not rely on the speed up due the excess translational temperature in the induction zone. While empirically, we show that the vibrational effect is negligible, this is further supported by the time scale analysis of section 3.

One can note, however, that the ideal model is not in quantitative agreement with the ZND model obtained numerically using the full chemistry. In the approximate model, due to the assumption of a square wave detonation, the turning point is larger by a factor of two compared to the generalized ZND model. This behaviour is consistent with the analysis of Short and Bdzil for a closely analogous problem, who have found that the rate of energy release in the reaction zone progressively shifts the turning point at smaller losses and larger velocity deficits as the rate of energy release is lowered [36]. A more detailed model incorporating a finite reaction zone will be communicated in a sequel.

In closing, while we did not find that vibrational relaxation to play an important role in the $H_2/O_2$ system, it does not imply its effect as being negligible in other fuels or other operating conditions. For example, the empirical evidence of substantial differences between argon and helium dilution in the experiments of Haloua et al. in propane calls for a closer scrutiny in hydrocarbons [13].

## 5. Conclusion

The reaction zone cellular structure of $2H_2/O_2$ detonation was found to be affected by the type of mono-atomic diluent when propagating in thin channels. At the same nominal induction length and nearly identical chemical kinetics, the experiments of detonation propagation with 70% argon dilution were found to yield cell sizes larger by a factor of 2 than those with 70% helium dilution, while the velocity deficits were also larger for the argon mixture in lower pressure experiments. These large differences permitted us to establish the importance of viscous losses and non-equilibrium effects. Non-equilibrium effects alone cannot reconcile these effects and would predict the opposite trend. We found that viscous losses can entirely account for the observed effects. Vibrational non-equilibrium effects suggested in the past to play a large role on the cellular dynamics were found to be negligible in the system studied.

## Acknowledgments

M. I. Radulescu acknowledges the financial support provided by the Natural Sciences and Engineering Research Council of Canada (NSERC) through the Discovery Grant "Predictability of detonation wave dynamics in gases: experiment and model development". This work was also supported by AFOSR grant FA9550-23-1-0214, with Dr. Chiping Li as program monitor. The authors wish to thank Dr. Q. Xiao, Dr. Z. Hong, for their valuable discussions, and Dr. A. Sow for his support with the computational code.

## Supplementary material

Supplementary material associated with this article can be found in the online version.

## References

[1] D. White, Turbulent structure of gaseous detonation, Phys. Fluids. 4 (1961) 465–480.

[2] Y. Denisov, Y. Troshin, Pulsating and spinning detonation of gaseous mixtures in tubes, Dokl. Akad. Nauk. SSSR. 125 (1959) 110–113.

[3] W. Fickett, W. Davis, Detonation: theory and experiment, Courier Corporation, 2000.

[4] B. Taylor, D. Kessler, V. Gamezo, E. Oran, Numerical simulations of hydrogen detonations with detailed chemical kinetics, Proc. Combust. Inst. 34 (2013) 2009–2016.

[5] Q. Xiao, A. Sow, B. Maxwell, M. Radulescu, Effect of boundary layer losses on 2D detonation cellular structures, Proc. Combust. Inst. 38 (2021) 3641–3649.

[6] F. Zangene, Z. Hong, Q. Xiao, M. Radulescu, The role of the argon and helium bath gases on the detonation structure of $H_2/O_2$ mixture, in: Proceedings of the $9^{th}$ International Conference on Hydrogen Safety, 2021.

[7] F. Zangene, A. Sow, M. Radulescu, Predictability of hydrogen-based mixtures detonations in thin channels: new experiments and improvements in the quasi-two-dimensional model, in: $28^{th}$ International Colloquium on the Dynamics of Explosive and Reactive Systems.

[8] X. Shi, A. Jayaraman, H. Wang, Probing vibrational nonequilibrium in detonations with ozone, Proc. Combust. Inst. 40 (2024) 105695.

[9] K. Uy, L. Shi, C. Wen, Chemical reaction mechanism related vibrational nonequilibrium effect on the Zel'dovich- von neumann- Döring (ZND) detonation model, Combust. Flame 196 (2018) 174–181.

[10] J. Smith, C. Schmitt, Q. Xiao, B. Maxwell, On the nature of transverse waves in marginal hydrogen detonation simulations using boundary layer loss modeling and detailed chemistry, Combust. Flame 268 (2024) 113598.

[11] U. of California at San Diego, Chemical-kinetic mechanisms for combustion applications, http://combustion.ucsd.edu (2016).

[12] M. Radulescu, The propagation and failure mechanism of gaseous detonations: experiments in porous-walled tubes, Ph.D. thesis, McGill University (2003).

[13] F. Haloua, M. Brouillette, V. Lienhart, G. Dupré, Characteristics of unstable detonations near extinction limits, Combust. Flame 122 (2000) 422–438.

[14] R. Kumar, Detonation cell widths in hydrogen-oxygen-diluent mixtures, Combust. Flame 80 (1990) 157–169.

[15] R. Kumar, W. Dewit, Detonation cell widths in hydrogen/oxygen/diluent mixtures at low initial pressures, J. Energy. Resour. Technol. 117 (1995) 13–17.

[16] R. Bhattacharjee, Experimental investigation of detonation reinitiation mechanisms following a mach reflection of a quenched detonation, Master's thesis, University of ottawa (2013).

[17] Y. Zeldovich, On the theory of the propagation of detonation in gaseous systems, Zh. Éksper. Teoret. Fiz. 10 (1940) 542–568.

[18] J. Von Neumann, Theory of shock waves, Technical report, Army Air Forces Headquarters, Wright Field, Ohio (1943).

[19] W. Döring, On detonation processes in gases, Annalen der Physik 43 (1943) 421–436.

[20] C. Westbrook, P. Urtiew, Chemical kinetic prediction of critical parameters in gaseous detonations, Vol. 19, Elsevier, 1982.

[21] J. Lee, The detonation phenomenon, Cambridge University Press, 2008.

[22] D. Goodwin, R. Speth, H. Moffat, B. Weber, Cantera: an object-oriented software toolkit for chemical kinetics, thermodynamics, and transport processes, version 2.5.1 (2021).

[23] D. Lide, CRC handbook of chemistry and physics, Vol. 85, CRC Press, 2004.

[24] K. Cheevers, Optical fibre-based hydrophone and critical ignition in detonation cells, Master's thesis, University of ottawa (2021).

[25] B. Taylor, D. Kessler, E. Oran, Estimates of vibrational nonequilibrium time scales in hydrogen-air detonation waves, in: $24^{\text{th}}$ International Colloquium on the Dynamics of Explosive and Reactive Systems, Vol. 23, 2013, p. 44.

[26] L. Shi, H. Shen, P. Zhang, D. Zhang, C. Wen, Assessment of vibrational non-equilibrium effect on detonation cell size, Combust. Sci. Technol. 189 (2017) 841–853.

[27] J. Dove, H. Teitelbaum, The vibrational relaxation of h2: Experimental measurements of the rate of relaxation by h2, he, ne, ar, and kr, Chem. Phys. 6 (1974) 431–444.

[28] R. Millikan, D. White, Systematics of vibrational relaxation, J. Chem. Phys. 39 (1963) 3209–3213.

[29] H. Mirels, Boundary layer behind shock or thin expansion wave moving into stationary fluid, Tech. rep., NACA (1956).

[30] Q. Xiao, M. Radulescu, Dynamics of hydrogen–oxygen–argon cellular detonations with a constant mean lateral strain rate, Combust. Flame 215 (2020) 437–457.

[31] S. Kao, J. Shepherd, Numerical solution methods for control volume explosions and znd detonation structure, Tech. rep., Galcit (2008).

[32] S. Falle, Self similar jets, Mon. Not. R. Astron. Soc. 250(3) (1991) 581–596.

[33] Q. Xiao, Dynamics of gaseous detonations under lateral strain rates, Ph.D. thesis, University of ottawa (2020).

[34] M. Radulescu, B. Borzou, Dynamics of detonations with a constant mean flow divergence, J. Fluid. Mech. 845 (2018) 346–377.

[35] L. He, P. Clavin, On the direct initiation of gaseous detonations by an energy source, J. Fluid. Mech. 277 (1994) 227–248.

[36] M. Short, J. Bdzil, Propagation laws for steady curved detonations with chain-branching kinetics, J. Fluid. Mech. 479 (2003) 39–64.

# Appendix: Detonations with Boundary Layer Losses: Square Wave Detonation

We analysed the structure and propagation of a detonation wave in the presence of boundary layer losses, following the analysis of He and Clavin for cylindrical quasi-steady detonations [35]. We perturb the ZND solution by a small perturbation in shock speed, which in turns entails small perturbations in the post shock state in the induction zone. The analysis reveals that the perturbations are of the order of the inverse activation energy.

In the shock-attached reference frame, the conservation laws for quasi-1D flow are:

$$\frac{d}{dx}(\rho u) = -\rho u \frac{1}{A}\frac{dA}{dx} \tag{1}$$

$$\frac{d}{dx}(\rho u^2 + p) = -\rho u^2 \frac{1}{A}\frac{dA}{dx} \tag{2}$$

$$\frac{d}{dx}\left(h + \lambda Q + \frac{1}{2}\rho u^2\right) = 0 \tag{3}$$

here, $p$, $\rho$, $u$, $h$, $A$ and $Q$ denote pressure, density, flow velocity in the x-direction, enthalpy, cross-section area and the chemical energy release. In the induction zone:

$$u\frac{d\xi}{dx} = K_i \exp\left(-\frac{E_a}{RT}\right) \tag{4}$$

with $\xi = 0$ at the shock and $\xi = 1$ marking the end of induction zone. In the reaction zone:

$$u\frac{d\lambda}{dx} = -\frac{\omega}{\rho} = -K_r\lambda \tag{5}$$

here we take $\lambda = 1$ in the reactants and $\lambda = 0$ in the products. We will assume $K_r$ to be very large, such that the structure is a square wave [36]. In the limit of $K_r \to \infty$, $\lambda \to 0$ in the burned gases.

The right hand side of the governing equations contain the nozzling term involving the lateral strain rate. These terms are higher order, and hence only their leading forms must be retained. We will assume a rectangular channel with effective area of $A = (W + 2\delta^*)(H + 2\delta^*)$ as shown in Fig. 21, where $\delta^*$ is the negative displacement thickness due to laminar boundary layers obtained by Mirels [29], $\delta^* = K_M\sqrt{\frac{\mu x}{\rho u}}$. The nozzling term can thus be written as:

$$\alpha = \frac{1}{A}\frac{dA}{dx} \simeq K_M\left(\frac{1}{W} + \frac{1}{H}\right)\sqrt{\frac{\mu}{\rho u x}} \tag{6}$$

We can then dispense with integrating the equations in the very thin reactive zones, and simply use the boundary condition at the sonic surface ($u_b = c_b$, $\lambda_b = 0$), shown in Fig. 22.

$$\rho_b u_b = \rho_0 D - \int_0^{\Delta_i} \rho u\left(\frac{1}{W} + \frac{1}{H}\right) K_M\sqrt{\frac{\mu}{\rho u}}x^{-\frac{1}{2}}\,dx \tag{7}$$

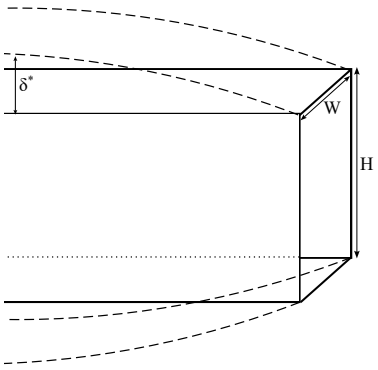


Figure 21: Boundary layer displacement thickness in a rectangular channel.

$$\rho_b u_b^2 + p_b = \rho_0 D^2 + p_0 - \int_0^{\Delta_i} \rho u^2 \left(\frac{1}{W} + \frac{1}{H}\right) K_M \sqrt{\frac{\mu}{\rho u}} x^{-\frac{1}{2}}\, dx \tag{8}$$

$$\frac{\gamma}{\gamma - 1}\frac{p_b}{\rho_b} + \frac{1}{2}u_b^2 = \frac{\gamma}{\gamma - 1}\frac{p_0}{\rho_0} + Q + \frac{1}{2}D^2 \tag{9}$$

For simplicity, we will deal with strong detonations, such that terms including $p_0$ in momentum equation and $\frac{\gamma}{\gamma-1}\frac{p_0}{\rho_0}$ in energy equation will be negligible. To integrate the integrals in Eq. (7) and Eq. (8), we will assume that the variables in the induction zone can be written as:

$$\rho = \rho_s + \rho', \quad u = u_s + u', \quad \ldots$$

with $\rho'$, $u'$ being small perturbations. Re-write Eq. (7) by only retaining leading order terms in the right-hand side and integrate:

$$\rho_b u_b = \rho_0 D \left(1 - 2\left(\frac{1}{W} + \frac{1}{H}\right) K_M \sqrt{\frac{\mu \Delta_i}{\rho_0 D}}\right) \tag{10}$$

where we used $\rho_s u_s = \rho_0 D$ from mass conservation across the shock. The momentum equation, Eq. (8), can be written in a similar way for the leading order perturbations

$$\rho_b u_b^2 + p_b = \rho_0 D^2 \left(1 - 2\frac{\gamma - 1}{\gamma + 1}\left(\frac{1}{W} + \frac{1}{H}\right) K_M \sqrt{\frac{\mu \Delta_i}{\rho_0 D}}\right) \tag{11}$$

in obtaining Eq. (11), we have used the strong shock relation of $\frac{u_s}{D} = \frac{\rho_0}{\rho_s} = \frac{\gamma-1}{\gamma+1}$. The momentum, Eq. (11), and energy, Eq. (9), equations can be re-written by eliminating $p_b$ using the sonic condition ($c_b^2 = \frac{\gamma p_b}{\rho_b} = u_b^2$). Re-write the mass, momentum, and energy equations:

$$\rho_b u_b = \rho_0 D \left(1 - \beta \left(\frac{\Delta_i}{\Delta_{i,CJ}}\right)^{\frac{1}{2}} \left(\frac{D}{D_{CJ}}\right)^{-\frac{1}{2}}\right) \tag{12}$$

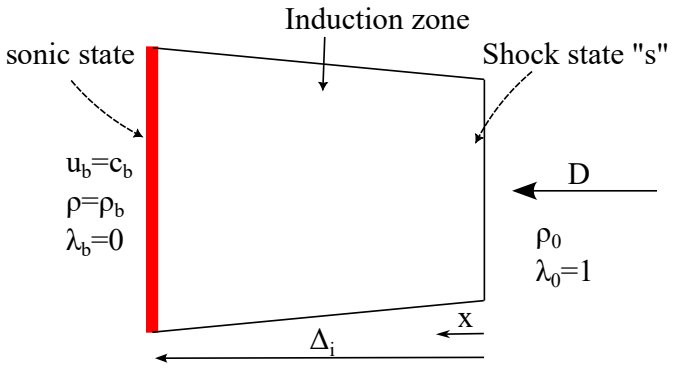


Figure 22: Sketch illustrating the square wave detonation model.

$$\frac{\gamma+1}{\gamma}\rho_b u_b^2 = \rho_0 D^2\left(1-\frac{\gamma-1}{\gamma+1}\beta\left(\frac{\Delta_i}{\Delta_{i,CJ}}\right)^{\frac{1}{2}}\left(\frac{D}{D_{CJ}}\right)^{-\frac{1}{2}}\right) \tag{13}$$

$$\frac{\gamma+1}{2(\gamma-1)}u_b^2 = Q+\frac{1}{2}D^2 \tag{14}$$

with

$$\beta = 2\left(\frac{1}{W}+\frac{1}{H}\right)\Delta_{i,CJ}K_M\sqrt{\frac{\mu}{\rho_0 D_{CJ}\Delta_{i,CJ}}}$$

note that $\beta$ is the constant parameter denoting the magnitude of the losses. We can now proceed to eliminate $\rho_b$ and $u_b$ from the system of equations Eq. (12)-(14), for $\beta \ll 1$ the following expression can be obtained:

$$\frac{\gamma^2}{\gamma^2-1}\left(\frac{D}{D_{CJ}}\right)^2\left[1+\frac{4}{\gamma+1}\beta\left(\frac{\Delta_i}{\Delta_{i,CJ}}\right)^{\frac{1}{2}}\left(\frac{D}{D_{CJ}}\right)^{-\frac{1}{2}}\right] = 2\frac{Q}{D_{CJ}^2}+\left(\frac{D}{D_{CJ}}\right)^2 \tag{15}$$

To close the system, we need an expression for $\frac{\Delta_i}{\Delta_{i,CJ}}$ in terms of $\frac{D}{D_{CJ}}$. The induction zone length is obtained by integrating Eq. (4), to the leading order:

$$\Delta_i = \frac{u_s}{k_i}\exp\left(\frac{E_a}{R(T_s)}\right)$$

where $T_s$ is the post-shock temperature. Similarly, for the nominal case without losses:

$$\Delta_{i,CJ} = \frac{u_{s,CJ}}{k_i}\exp\left(\frac{E_a}{R(T_{s,CJ})}\right)$$

For strong shocks, post-shock velocity $u_s \sim D$ and $T_s \sim D^2$, therefore:

$$\frac{\Delta_i}{\Delta_{i,CJ}} = \frac{D}{D_{CJ}}\exp\left(\frac{E_a}{R(T_{s,CJ})}\left(\frac{1}{(D/D_{CJ})^2}-1\right)\right) \tag{16}$$

replacing Eq. (16) in the equation, Eq. (15) and assuming small perturbations of speed from the CJ state, a relation between velocity, $\Delta = 1-\frac{D}{D_{CJ}}$, and the losses is obtained:

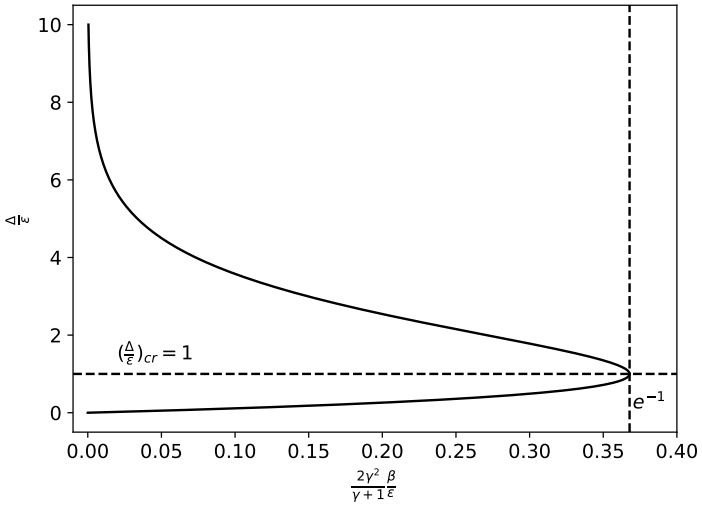


Figure 23: The dual solution C-curves for boundary layer induced detonation quenching.

$$\frac{\Delta}{\varepsilon}\exp\left(-\frac{\Delta}{\varepsilon}\right) = \frac{2\gamma^2}{\gamma+1}\frac{\beta}{\varepsilon}, \quad \varepsilon = \left(\frac{E_a}{RT_{s,CJ}}\right)^{-1} \tag{17}$$

where $\varepsilon = \frac{1}{E_a/RT_{s,CJ}}$. Figure 23 shows the dual-solution behaviour given by Eq. (17). The turning point will be at the zero slope of $\frac{2\gamma^2}{\gamma+1}\frac{\beta}{\varepsilon}$ in terms of the argument of the exponential. Differentiate the LHS of Eq. (17), the maximum loss term is:

$$\beta^* = \frac{\gamma+1}{2\gamma^2}\frac{\varepsilon}{e} \tag{18}$$

where $e^{-1} = \frac{\gamma^2}{\gamma+1}\frac{\beta^*}{\varepsilon}$. As expected, $\beta^*$ is a small quantity of order $\varepsilon$.

In summary, Eq. (17) provides the dependence of detonation speed on the loss parameter, with the maximum loss permitting propagation given by Eq. (18).

# Chapter 5

# Pressure dynamics resulting from head-on reflection of detonation

In this study, the reflection of a detonation wave from a wall is examined as a test case to demonstrate the interplay between small-scale and large-scale dynamics, where the pressure evolution will be shown to respond to global-scale effects. We examine the mean pressure evolution of detonations as they propagate and reflect from an end wall within a narrow channel shock tube, considering the impact of boundary layer losses. Additionally, we replicate the mean pressure evolution using a simple one-dimensional ZND model.

This work is in preparation for submission as a journal paper and was already presented at *the 15th International Symposium on Hazards, Prevention, and Mitigation of Industrial Explosions (ISHPMIE)* conference in June 2024. The author conducted the experiments and simulations of the detonation in the regular structure of the hydrogen-oxygen-argon mixture, performed the analyses, and wrote the paper. The second author, Hongxia Yang, conducted the modelling and 1D simulation in the irregular methane-oxygen mixture. The conceptual planning was done in collaboration with the Ph.D. supervisor, Prof. M. I. Radulescu.

# Pressure Dynamics Resulting from Head-On Reflection of Detonation

Farzane Zangene[a], Hongxia Yang[a] & Matei Radulescu[a]

[a] Department of Mechanical Engineering, University of Ottawa , Ottawa, ON K1N6N5, Canada

E-mail: *fzang055@uottawa.ca*

**Abstract**

In this study, the pressure evolution resulting from the head-on reflection of detonation waves as the reflected shock travels through the reaction zone is investigated. Detailed experiments on detonation reflection were conducted, and the transient dynamics were monitored using pressure transducers and high-speed schlieren videos. This allowed us to resolve the inner structure of the reflection dynamics and the sequence of events controlling the overall pressure evolution within the reaction time scale. The experiments were performed using mixtures of $CH_4/2O_2$ and $2H_2/O_2/7Ar$, spanning the degree of cellular regularity of detonations in reactive gases. It was found that for regular mixtures characterized by a long reaction zone structure, the simple one-dimensional ZND model is sufficiently accurate to predict the pressure evolution of the reflection. This was further confirmed through a comparison of experiments with both two-dimensional and one-dimensional simulations, employing a previously introduced model that accounts for boundary layer losses. For irregular detonation waves in which the reaction zone significantly departs from the steady ZND model, we propose a new model that accounts for the hydrodynamics thickness of the detonation. The hydrodynamic thickness was found to be approximately one cell width, $\lambda$, in both mixtures investigated. Using this knowledge, a simplified one-step combustion model tailored to the global structure of the reaction zone is introduced. This model employs one-dimensional reactive Euler equations, assuming constant volume combustion upon reflection, thus constructing the pressure evolution of the reflected detonation in irregular structure detonations. The results demonstrated that the end-wall pressure evolution resulting from the reflection of high-speed detonation can be reliably predicted using the simple proposed model.

**Keywords: detonation reflection experiments, reaction zone length, pressure evolution, numerical modelling**

## 1 Introduction

When a detonation wave propagates inside a closed vessel and reaches the end wall, it produces a reflected shock wave that travels back into the tube. This shock wave serves to bring the gas behind the detonation to a state of rest. The over-pressures produced by these waves depend significantly on the regularity of the incoming detonation, the configuration of the vessel and the angle of the reflection often resulting in very high pressure spikes (Shepherd et al., 1991). This increased pressure near the wave reflection region is of great interest in safety analyses, as it can have significant implications for operational safety. While extensive efforts have been made to study various aspects of the phenomena (Shepherd et al., 1991, Karnesky, 2010, Damazo, 2013, Damazo and Shepherd, 2017), there is a lack of detailed insights into the structure of detonation and its reflection with sufficient time resolution in the scales of the reaction zone time.

This paper presents an experimental and numerical investigation of detonation behavior prior to reflection and the subsequent reflected wave in $2H_2/O_2/7Ar$ and $CH_4/2O_2$ mixtures exhibiting both regular and irregular cellular structures. First, detailed experiments were conducted to visualize the detonation propagation inside a narrow channel and its reflection from the end wall. Then, the pressure dynamics were quantified using pressure transducers as the detonation wave traversed the channel and the reflected shocks passed through the reaction zone of the preceding detonation wave. For the regular mixture of $2H_2/O_2/7Ar$, a previously proposed model is employed to account for boundary layer losses to reproduce the reflection dynamics and wave structure through both 2D and 1D simulations (Xiao et al., 2021, Zangene et al., 2022). However, for irregular structure detonation waves in the

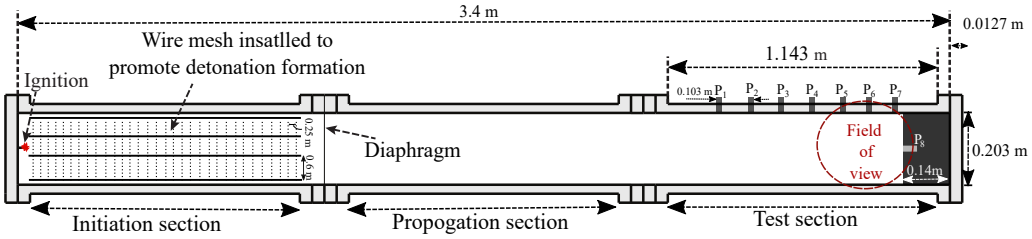


***Fig. 1**: Schematic of the shock tube used in the experiment.*

***Table 1**: The experimental test gases and their properties.*

| **Mixture** | $p_0$ [kPa] | $\chi$ | $D_{CJ}$ | $p_{CJ}$ [kPa] | $p_{CJ,Reflected}$ [kPa] |
|---|---|---|---|---|---|
| $2H_2/O_2/7Ar$ | 4 | 0.73 | 1602 | 64 | 155 |
| $CH_4/2O_2$ | 6 | 522 | 2267 | 162 | 405 |

$CH_4/2O_2$ mixture, a simplified one-step combustion model fitted to the overall structure of the detonation hydrodynamic thickness was introduced, where the reaction zone deviates significantly from steady ZND model predictions (Lee and Radulescu, 2005). This model utilizes one-dimensional reactive Euler equations, assuming constant volume combustion upon reflection, thereby calculating the pressure evolution of the reflected detonation in irregular structure detonations.

## 2 Experiments

### *2.1 Experimental set-up*

The experiments were performed in a 3.4-m-long shock tube, with 0.019-m-thickness and 0.203-m-height. The schematic illustrating the experimental set-up is shown in Fig. 1. Mesh wires were placed in the initial section of the shock tube to ensure the formation of detonation within this segment. Subsequently, the detonation propagated through the second section to reach a steady propagation speed before entering the third test section. A rectangular object, composed of polyvinyl chloride, was placed at the end of the test section to serve as a wall. Additional details regarding the experimental set-up can be found in a previous work (Bhattacharjee, 2013).

The two mixtures studied were a stoichiometric mixture of methane-oxygen ($CH_4/2O_2$) and a stoichiometric mixture of hydrogen-oxygen diluted with argon ($2H_2/O_2/7Ar$). The selection of these two mixtures was based on their significant differences in cellular regularity. As shown in Table 1, the detonation stability parameter $\chi$, (Radulescu, 2003), varies widely between the two selected mixtures. The Chapman-Jouguet (CJ) detonation speed, $D_{CJ}$, pressure, $p_{CJ}$ and reflected pressure, $p_{CJ,Reflected}$, are calculated using the Shock and Detonation Toolbox (SDToolbox) (Williams, 2014) and Sandiego mechanism (SanDiego, 2016). We varied the initial pressure, $p_0$, of the test gas to create a single large detonation cell, enhancing the visibility of the reflection process. Since the mixture of $2H_2/O_2/7Ar$ has low reactive sensitivity, a more reactive driver gas of stoichiometric ethylene-oxygen (i.e., $C_2H_4/3O_2$) was used in the initiation section, which was separated from the propagation section with a thin aluminum foil diaphragm. Preliminary tests were conducted to prevent an excessively driven detonation wave in the test section resulting from the high-pressure driver gas. The minimum pressure required to initiate detonation waves was identified. Throughout all experiments, a constant ratio of 2.4 between the driver gas and the test gas was maintained as a reference for filling the shock tube. All experiments reported were conducted at an initial temperature of 293 K. To guarantee the results reliability and reproducibility, the experiments were conducted twelve times under identical conditions in the $2H_2/O_2/7Ar$ mixture and thirteen times in the $CH_4/2O_2$ mixture.

Each mixture was prepared in a separate mixing tank by the method of partial pressures and was then

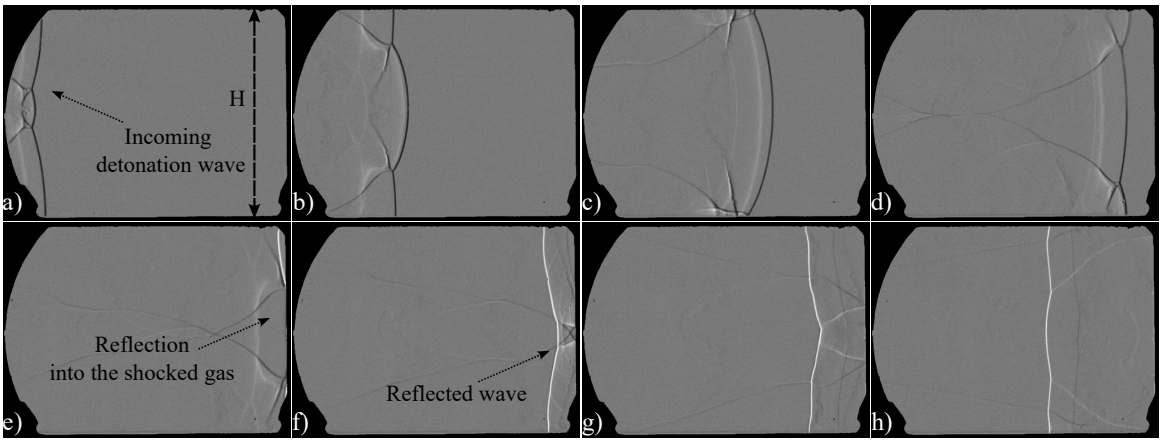


***Fig. 2**: Schlieren images of the incident detonation and the reflected shock wave in the mixture of $2H_2/O_2/7Ar$ at $p_0 = 4$ kPa. H is the channel height of 0.203 m.*

***Table 2**: Detonation average propagation speed and cell width measured from the experiments.*

| **Mixture** | $p_0$ [kPa] | $\lambda$ [m] | **D** [m/s] | $t_\Delta = \frac{\lambda}{D}$ [µs] |
|---|---|---|---|---|
| $2H_2/O_2/7Ar$ | 4 | 0.203 | 1285±40 | 158±5 |
| $CH_4/2O_2$ | 6 | 0.10±0.022 | 2096±91 | 47±10 |

left to mix for more than 24 hours. Monitoring of the mixing process was done using an Omega PX409-015AV pressure transducer with the accuracy of ± 0.08%. The shock tube was evacuated to a pressure below 80 Pa before filling it with the gas. The initial ignition of the premixed combustible mixture was achieved using a high voltage igniter (HVI) that was custom designed and built (Bhattacharjee, 2013). The HVI utilized a capacitor discharge method for ignition. In all experiments, the capacitor was charged to a voltage of around 25 kV.

A linear arrangement of two 113B24 piezoelectric PCB pressure sensors, followed by five 113B27 sensors, was evenly distributed along the top wall of the shock tube. This setup was used to capture pressure signals from the detonation before reflection. Additionally, for the investigation of detonation reflection, one 113B24 piezoelectric PCB pressure sensor was inserted into the center of the end wall to measure the over-pressure resulting from the reflection. The sensors resonate at 500kHz, while the pressure signals during the experiments were recorded at a rate of 1.5 MHz. All pressure gauges used in the experiments have a diameter of 5.5-mm and a maximum error of 1.3%, as determined from the calibration data. The signal conditioners used for these pressure sensors are the PCB Piezotronics model 482C05 and 482C16. To improve the quality of the pressure signals and minimize noise, a filtering process was applied to the raw data using a cut-off frequency of 250 kHz. This frequency selection aimed to preserve crucial information regarding the smallest spatial scales observed in the detonation structure during the experiments. Furthermore, the propagation process was visualized by utilizing the classical Z-type schlieren technique with the Phantom v1210 camera at 77108 frames per second (about 12.9 $\mu s$ for each interval). The schlieren visualization was implemented with a vertical knife-edge utilizing a light source of 360 W, with the exposure time set to 0.44 $\mu$s and the frame resolution kept at $384 \times 288$ $px^2$.

### *2.2 Experimental results*

The propagation of the incident detonation and its reflection from the end wall in the regular cellular structure mixture of hydrogen-oxygen-argon is shown in Fig. 2. The detonation propagates from left to right, as depicted in Fig. 2 (a, b, c and d). The detonation front has a single large cell, displaying

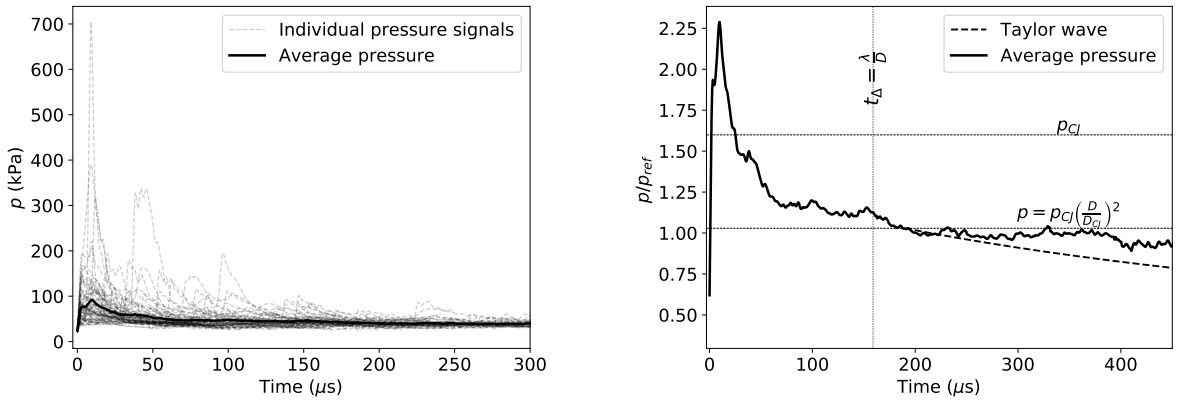


*(a) Experimental results from 72 pressure sensors.* *(b) Scaled average pressure.*

***Fig. 3**: Temporal evolution of the incoming detonation wave pressure measured on the top wall in the mixture of $2H_2/O_2/7Ar$ at $p_0 = 4$ kPa.*

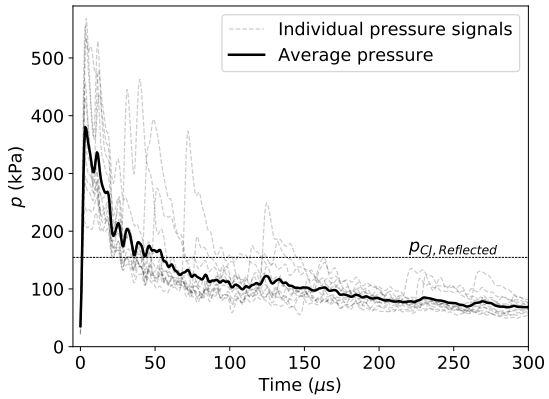


***Fig. 4**: Temporal evolution of the reflected wave pressure measured on the end wall in $2H_2/O_2/7Ar$ mixture at $p_0 = 4$ kPa.*

a notably regular pattern characteristic of this mixture with long reaction zone length. Immediately following the head on reflection of the detonation from the end wall, as shown in Fig. 2 (e, f, g and h), the shock rapidly consumes all the unburned gases. Subsequently, it continues to propagate from right to left, into the reaction zone of the preceding incoming detonation wave.

The global propagation speed, $D$, of the detonation wave across the entire test section was determined by pressure sensors using the time-of-arrival method, as detailed in Table 2. The reported cell width, $\lambda$, is the average obtained from schlieren images. The speed and cell size measurements are the average value of the repeated experiments. The value of the time corresponding to one cell behind the detonation, which indicates the potential location of the sonic surface, $t_\Delta = \frac{\lambda}{D}$, is also presented in Table 2. The standard deviation of the propagation speed and cell width measured in repeated experiments is included. Figure 3a depicts the 72 pressure signals recorded by pressure sensors on the top wall following the passage of the detonation wave, with the average pressure indicated by the solid line. The signal in the plot has been shifted so that zero time on the plot corresponds to the time of detonation arrival. While the peak of the average pressure reaches approximately 100 kPa, certain sensors recorded peaks as high as 700 kPa. The high peaks might arise from the stronger part of the detonation front passing or from a transverse wave detected by the sensor.

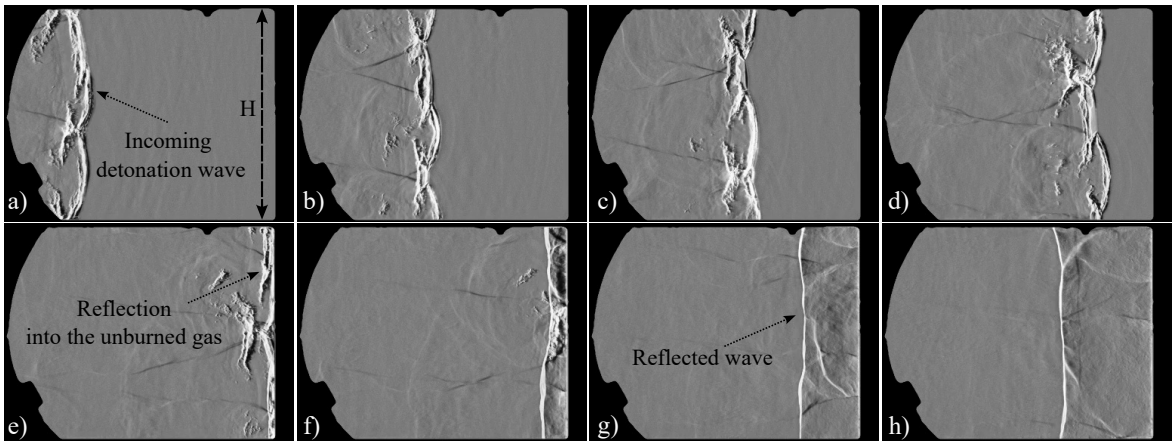


***Fig. 5**: Schlieren images of the incident detonation and the reflected shock wave in the mixture of $CH_4/2O_2$ at $p_0 = 6$ kPa. H is the channel height of 0.203 m.*

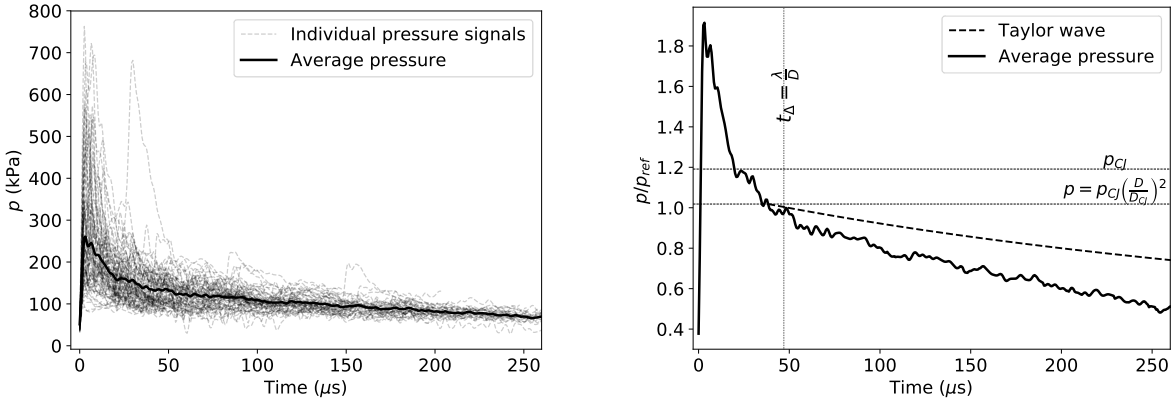


*(a) Experimental results from 78 pressure sensors.*

*(b) Scaled average pressure signal.*

***Fig. 6**: Temporal evolution of the incoming detonation wave pressure measured on the top wall in $CH_4/2O_2$ mixture at $p_0 = 6$ kPa.*

Using the strong detonation solution, the pressure at CJ state is given by $p = \frac{\rho_0 \cdot D^2}{\gamma+1}$ (Lee, 2008). In this equation, $D$, $\rho_0$ and $\gamma$ denote the experimentally measured detonation speed, the density at the initial state and the specific heat ratio at equilibrium state derived from the equilibrium sound speed, respectively. This pressure serves as the reference pressure, $p_{\text{ref}}$, in Fig. 3b for normalizing the pressure signals observed during the experiments. In scenarios with detonations experiencing heat losses, the equilibrium pressure tends to decrease compared to $p_{CJ}$. Utilizing conservation laws for mass and momentum in a strong detonation case, one can derive the pressure at the sonic surface as $p = p_{CJ} * (\frac{D}{D_{CJ}})^2$, with $D$ denoting the average velocity obtained from the experiments. Figure 3b illustrates a rapid pressure increase after the detonation passage and a subsequent decline within the hydrodynamic thickness, leading the signal towards a plateau pressure. The point where the line representing calculated equilibrium pressure with losses intersects with the pressure plot is around 190 μs, suggesting a potential time for the sonic surface. This time corresponds approximately to the time calculated from experimental values for one cell $t_\Delta = 158$ μs. The profile of the Taylor expansion wave following the detonation is calculated at the position where the detonation wave has traveled from the ignition point to the first pressure gauge ($x_{traveled} = 2.6$ m)(Law, 2006). The reduction in pressure observed in the experimental data is smaller than that calculated from the expansion wave. This difference can be caused by the presence of the driver gas in these experiments, which continues

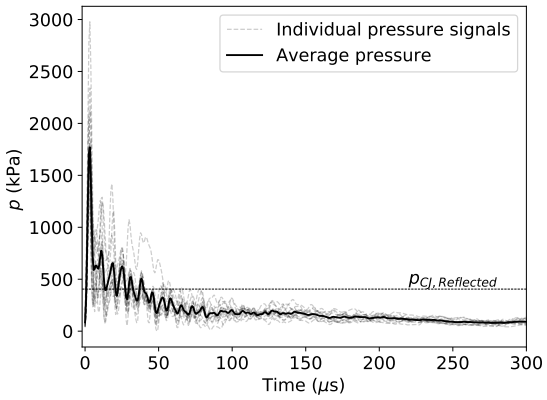


***Fig. 7**: Temporal evolution of the reflected wave pressure measured on the end wall in $CH_4/2O_2$ mixture at $p_0 = 6$ kPa.*

to affect the propagation of the detonation. Following the detonation reflection from the end wall, the rapid ignition of the gas within the induction zone causes the pressure to surge to three times the peak average pressure of the incoming detonation, as depicted in Fig. 4. Subsequently, as it traverses the long reaction zone, the pressure decreases below the reflected wave pressure $P_{CJ,Reflected}$. The plot captures the oscillation and envelope of these signals as they gradually decay over time across 12 repeated experiments.

The schlieren images in Fig. 5 illustrate the propagation of the detonation and its subsequent reflection in methane-oxygen mixture. In contrast to the laminar reaction front seen in hydrogen-oxygen-argon mixture, the reaction front here is turbulent, with unreacted gas pockets trailing behind.

Figure 6a displays the pressure dynamics of the incoming detonation from 78 sensors, alongside the average pressure. Notably, the peak pressure exceeds twice the average peak pressure seen in hydrogen-oxygen-argon mixture, reaching oscillations up to 750 kPa that swiftly decay toward a plateau. As shown in Fig. 6b, the time when the pressure crosses the sonic surface is about 47 µs, which closely matches the time of one cell measured in experiments, refer to Table 2. The decrease in pressure observed in the experiment exceeds that predicted by the Taylor wave calculation, which can be attributed to the presence of heat losses in the experiment.

The pressure dynamics as the reflected shocks traverse through the reaction zone of the detonation wave are depicted in Fig. 7. Various signals in the plot correspond to 13 repeated experiments conducted under identical conditions. The peak average pressure of the reflected detonation reaches up to 7 times higher than the average pressure of the incoming detonation and gradually decreases toward a plateau below the CJ pressure of the reflected wave.

## 3 Numerical Simulations

### *3.1 Modelling the reflection of the regular cellular structure detonation wave*

A quasi-2D model is employed to simulate boundary layer losses of a detonation in a thin channel, as discussed elsewhere (Xiao et al., 2021, Zangene et al., 2022). The governing equations, reactive inviscid Euler equations, were solved using a second-order-accurate exact Godunov solver with Adaptive Mesh Refinement (AMR). The code utilized is the MG code, developed by S. Falle at the University of Leeds (Falle, 1991). In line with a previous (Xiao et al., 2021) mesh study under similar conditions, the numerical resolution adopted 5 levels of mesh refinement, with coarsest and finest grid sizes of 1/2 $\Delta_i$ (induction zone length) and 1/16 $\Delta_i$, respectively.

The computational domain height remained constant at the experimental height of 0.203 m, equivalent to 72 $\Delta_i$ for $p_0$ = 4.1 kPa in the $2H_2/O_2/7Ar$ mixture. The domain length was set to 1500 $\Delta_i$. The

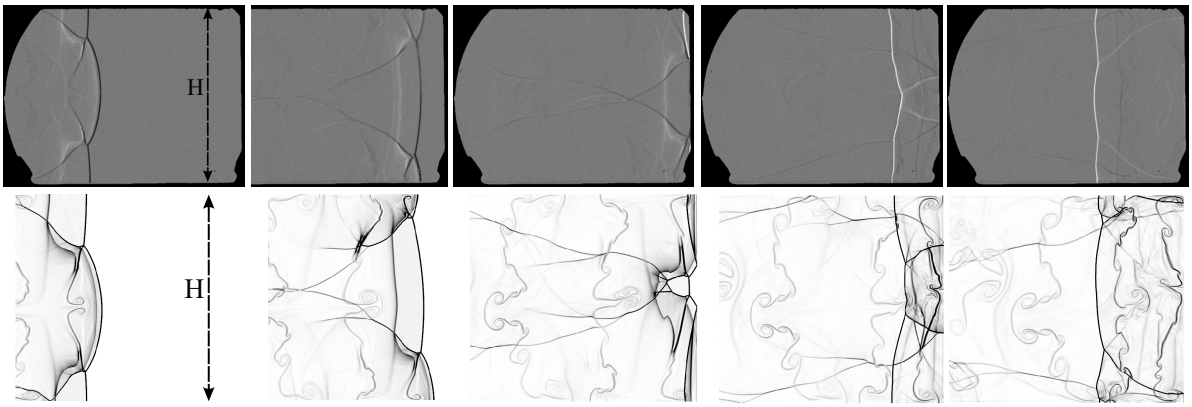


***Fig. 8**: Comparisons of the gradient of the density of the incoming detonation and reflected wave from the quasi-2D simulation (bottom row) with the schlieren photos from experiment (top row) in $2H2/O2/7Ar$ mixture at $p_0 = 4$ kPa. H is the channel height of 0.203 m.*

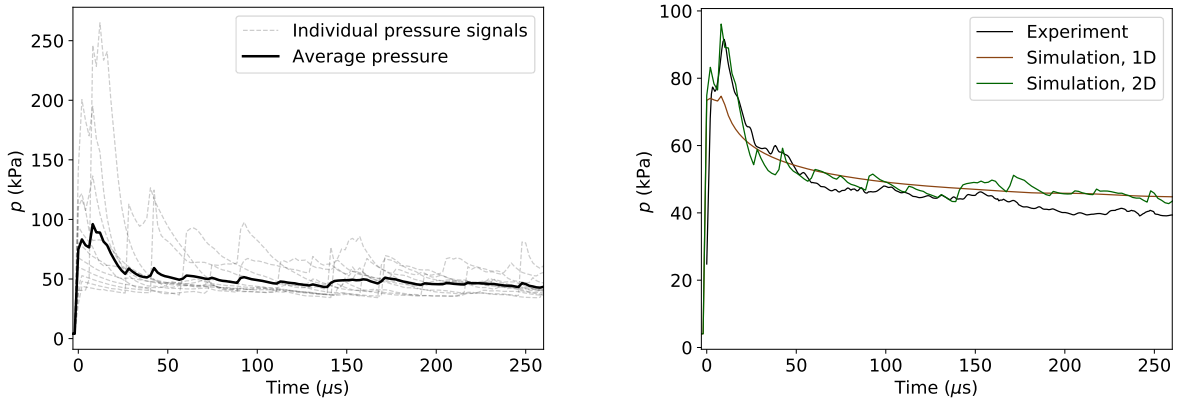


*(a) 2D Simulation results from 12 locations.*

*(b) Average pressure comparison.*

***Fig. 9**: Temporal evolution of the incoming detonation wave pressure measured on the top wall in $2H_2/O_2/7Ar$ mixture at $p_0 = 4$ kPa.*

detonation propagated from left to right, with reflective boundary conditions applied to the top, bottom, and right ends, and zero-gradient boundary conditions applied to the left end. The computations were initiated using a ZND profile positioned 300 $\Delta_i$ from the left boundary. We utilized a two-step chemistry model that includes a thermally neutral induction zone and an exothermic reaction zone to model the combustion.

Figure 8 illustrates that the simulations can effectively reproduce the qualitatively observed features of the detonation structure and its cellular dynamics before and after reflection from the end wall. This simulation effectively captures the cellular dynamics and cell size, indicating the reliability of the proposed quasi-2D formulation and the two-step chemistry model in simulating real detonations. Similar simulations are also conducted in one dimension.

The average velocity deficit of detonation propagation measured in one cell in the two-dimensional simulation ($D/D_{CJ} = 0.82$) and the one-dimensional simulation (0.83) is in good agreement with the global velocity measured from the experiments (0.8). To analyze the pressure dynamics before the detonation wave reflects, we extracted pressure signals from 12 locations across one cell in the 2D numerical simulation, recorded at a frequency of 500 kHz. Figure 9a presents these pressure signals alongside the average pressure across one detonation cell. Remarkably, the average pressure measured from the simulation closely matches the experimental data, capturing both peak pressure

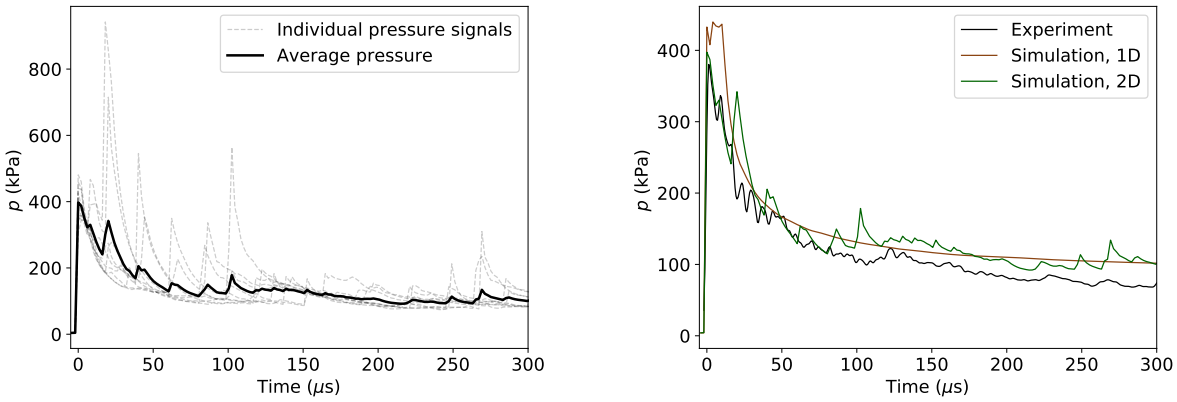


*(a) 2D Simulation results from 9 locations.*

*(b) Average pressure comparison.*

***Fig. 10**: Temporal evolution of the reflected wave pressure measured on the end wall in $2H_2/O_2/7Ar$ mixture at $p_0 = 4$ kPa*

and decay rate towards the plateau as shown in Fig. 9b. The 1D simulation also predicts a similar trend in pressure evolution. After 158 µs, which marks the end of one cell, the experimental signal drops slightly more. This decrease can be ascribed to heat losses and Taylor waves following the detonation.

In repeated experiments, we consistently observed that the detonation wave impacted the pressure sensor on the middle of the end wall every time, but with varying parts of the cell, such as the Mach shock or incident shock. This variability resulted in different overpressures. To ensure a meaningful comparison with experiments, we selected nine evenly distributed locations from the top to the bottom of the end wall. This approach allows us to capture the overpressure resulting from the reflection of the detonation from different parts of the cell in our simulation results. The pressure signals from these 9 locations on the end wall of the simulation are extracted over time, and all the signals, along with the average, are presented in Fig. 10a. As shown previously with the signals from the repeated experiments, all the oscillations decay over time, and the average tends towards a plateau. A similar good agreement between the numerics and experiments is observed when examining Fig. 10b. The 2D simulation closely predicts the oscillation and decay rate of the experiments, with the experimental pressure dropping more over time. Although the 1D simulation does not predict the oscillation due to the cellular structure of the detonation, it still predicts the overall decay rate of pressure very well.

### *3.2 Modelling the reflection of the irregular cellular structure detonation*

For irregular detonation waves where the reaction zone deviates significantly from the steady ZND model (Lee and Radulescu, 2005), we utilize a fitted 1D global structure to model the experimentally observed structure of the detonation. Based on our experiments, we found that the average hydrodynamic thickness in the methane-oxygen mixture aligns closely with one detonation cell width. Therefore, we modify the pressure profile of the detonation before reflection to reach the CJ state within this single cell thickness, as illustrated in Fig. 11a. After reflection, we consider constant volume combustion within the gas, using the conditions of the von Neumann state (vn) of the incoming detonation, as illustrated in Fig. 11b. The reflected shock will propagate back into the reaction zone of the preceding detonation. The governing equations utilized are the one-dimensional reactive Euler

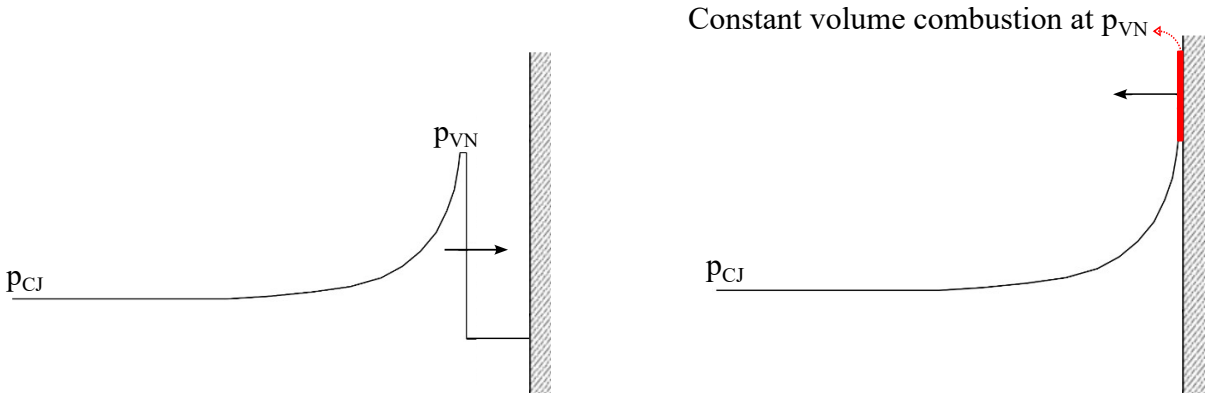


*(a) Pressure profile of the incoming detonation.* *(b) Pressure profile at the time of the reflection.*

***Fig. 11**: Sketch of the proposed one-dimensional model in $CH_4/2O_2$ mixture at $p_0 = 6$ kPa.*

***Table 3**: Thermo-chemical properties and model parameters for one-dimensional detonation reflection simulation at $T_0$=293 K.*

| **Mixture** | $p_0$ (kPa) | $\gamma_{VN}$ | $\frac{Q}{RT_0}$ | $k_r$ | $\nu$ | $\Delta_i$ (m) |
|---|---|---|---|---|---|---|
| $CH_4/2O_2$ | 6 | 1.17 | 62 | 3 | 1 | 0.0087 |

equations, outlined as follows:

$$\frac{\partial \rho}{\partial t} + \frac{\partial \rho u}{\partial x} = 0 \tag{1}$$

$$\frac{\partial \rho u}{\partial t} + \frac{\partial \rho uu}{\partial x} + \frac{\partial p}{\partial x} = 0 \tag{2}$$

$$\frac{\partial \rho E}{\partial t} + \frac{\partial (\rho E + p)u}{\partial x} = Q\frac{D\rho\lambda_r}{Dt} \tag{3}$$

Where $\rho$, $\mathbf{u}$, $p$, $Y$ and $\lambda_r$ represent density, velocity vector, pressure, mass fraction of the product and the reaction progress variable, respectively. The total energy is defined as $E = \frac{p}{\rho(\gamma-1)} + \frac{\mathbf{u}^2}{2}$ . The global heat release Q was determined to accurately reproduce the CJ Mach number, $M_{CJ}$, as specified for a perfect gas (Lee, 2008).

$$\frac{Q}{RT_0} = \frac{\gamma}{2(\gamma^2-1)}(M_{cj} - \frac{1}{M_{cj}})^2. \tag{4}$$

In the above equation, $R$ represents the universal gas constant and $\gamma$ denotes the isentropic index calculated in the post-shock state. The transport equation of the one-step reaction variable employed in the model can be written as:

$$\frac{\partial \rho\lambda_r}{\partial t} + \frac{\partial \rho u\lambda_r}{\partial x} = k_r\rho(1-\lambda_r)^\nu \tag{5}$$

In this context, $k_r$ is the rate constants and $\nu$ indicates the reaction order. Table 3 lists the values utilized in the simulation. In this table, $k_r$ is a dimensionless value obtained through non-dimensionalization with respect to the initial state.

Our experiments in the methane-oxygen mixture revealed that the reaction zone spans approximately one detonation cell length, $\lambda_{Experiemnt} = 0.10$ m. By adjusting the value of $k_r$, we can align the reaction zone thickness with the observed hydrodynamic thickness of $\lambda = 12\Delta_i$. Figure 12a shows the fitted pressure profile of the incoming detonation used in the simulation at the time of reflection. A two-

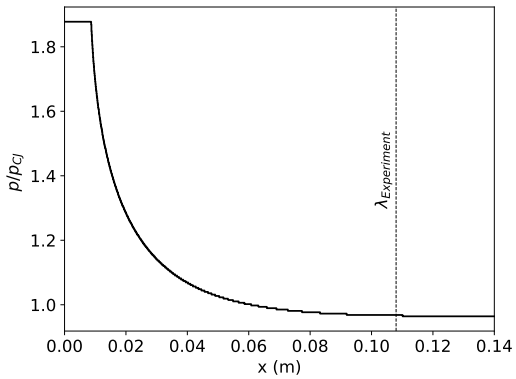


*(a) ZND pressure profile of the detonation.*

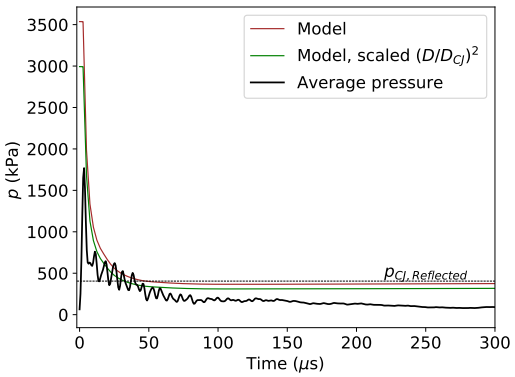


*(b) Reflected pressure from the end wall.*

***Fig. 12**: a) Fitted 1D global structure of the detonation and b) the reflected pressure evolution with time in comparison with experiment in $CH_4/2O_2$ mixture at $p_0 = 6$ kPa.*

step chain-branching reaction model is employed to describe the ZND profile of the detonation before reflection. The solver utilized for the numerical simulation is identical to the one described for the regular mixture simulations. The numerical resolution employed five levels of mesh refinement, with the coarsest grid size being $\frac{1}{4}\Delta_i$ and the finest grid size being $\frac{1}{64}\Delta_i$.

Figure 12b presents the outcome of the 1D simulation, showing pressure-time traces of the reflected wave from the simulation, captured at the end wall. The frequency of collecting data from the simulation is 500 kHz. The red line represents the prediction of the proposed model, while the green line shows the prediction of the model adjusted for losses as explained in the experimental results section. The model closely captures the decay rate observed in the experiments until reaching the sonic surface, 47 µs. Beyond this point, both signals converge toward a plateau. However, the experimental pressure continues to decline, due to Taylor expansion waves and heat dissipation.

## 4 Conclusions

The present work showed the detailed dynamics of the structure and pressure evolution resulting from head-on reflection of detonation waves on the time scales of the reaction zone structure in the two mixtures of $2H_2/O_2/7Ar$ and $CH_4/2O_2$. It was observed that for both mixtures, the location of the sonic surface is approximately one cell downstream from the front. Regarding the modeling aspect, for regular mixtures characterized by a long reaction zone structure, the simple one-dimensional ZND model effectively predicts the pressure evolution of the reflection. Additionally, for irregular mixture of methane-oxygen when the ZND model fails to predict the global reaction zone structure, we proposed a simplified one-step combustion model tailored to the global structure of the reaction zone. The model closely captures the decay rate observed in the experiments until reaching the sonic surface.

## Acknowledgements

The authors would like to express their appreciation to Z. Liang from the Canadian Nuclear Laboratories (CNL), and E. Studer and S. Koudriakov from Université Paris-Saclay, the French Alternative Energies and Atomic Energy Commission (CEA), for their sponsorship and valuable discussions.

## References

Bhattacharjee, R. (2013). *Experimental investigation of detonation reinitiation mechanisms following a Mach reflection of a quenched detonation*. University of Ottawa, Master Thesis.

Damazo, J. S. (2013). *Planar reflection of gaseous detonations*. California Institute of Technology.

Damazo, J., Shepherd, J. E. (2017). *Observations on the normal reflection of gaseous detonations*. Shock Waves, 27(5):795–810.

Falle, S. (1991). *Selfsimilar jets*. Monthly Notices of the Royal Astronomical Society.

Karnesky, J. A. (2010). *Detonation induced strain in tubes*. Ph.D. thesis, California Institute of Technology.

Law, C. (2006). *Law. combustion physics*. New York.

Lee, J. (2008). *The Detonation Phenomenon*. Cambridge University Press.

Lee, J., Radulescu, M. (2005). *On the hydrodynamic thickness of cellular detonations*. Combustion, Explosion and Shock Waves, 41:745–765.

Radulescu, M. (2003). *The propagation and failure mechanism of gaseous detonations: experiments in porous-walled tubes*. McGill University, Ph.D. thesis.

SanDiego, . (2016). *Chemical mechanism: Combustion research group at uc san diego*.

Shepherd, J., Teodorcyzk, A., Knystautas, R., Lee, J. (1991). *Shock waves produced by reflected detonations*. Progress in Astronautics and Aeronautics, 134:244–264.

Williams, F. (2014). *Chemical mechanism: combustion research group at uc san diego*.

Xiao, Q., Sow, A., Maxwell, B., Radulescu, M. (2021). *Effect of boundary layer losses on 2D detonation cellular structures*. Proceedings of the Combustion Institute, 38:3641–3649.

Zangene, F., Sow, A., Radulescu, M. (2022). *Predictability of hydrogen-based mixtures detonations in thin channels: new experiments and improvements in the quasi-two-dimensional model*. in: Proceedings of the Twenty-eighth, ICDERS, Naples.

# Chapter 6

# Modelling and experiments of triple-point reflection in detonations

The objective of this section is to develop a sub-cellular model. The first step in creating such a model is to predict the dynamics of a single cell, specifically determining the shock strength at the start of the detonation cell given its strength at the end of the cell. To achieve this, we reformulate the triple-point reflection model [44, 45], assuming that the Mach shock is reactive. The goal is to determine the strength of the lead shock after the triple-point collision. The model's predictions are then compared with experimental results from propagating detonations in narrow channels with an enlarged cell structure.

This study was presented at *the International Symposium on Shock Waves* conference in July 2023. The author developed the model, conducted the experiments, performed the analyses, and wrote the paper. The conceptual planning and review were done in collaboration with the PhD supervisor, Prof. M. I. Radulescu.

# Modelling and Experiments of the Triple Point Reflection in Detonations

**F. Zangene, M.I. Radulescu**
Department of Mechanical Engineering, University of Ottawa, Ottawa, ON K1N6N5, Canada

fzang055@uottawa.ca

**Abstract**

The objective of this study is to formulate a model to determine the strength of the newly formed reactive Mach shock after the triple point reflection within a detonation cell. Experimental evidence showed that this Mach shock is an overdriven reactive wave. However, in the available three shock theory, all the shocks are assumed to be inert. We attempt to modify this model by incorporating the assumptions of a reactive Mach shock and using the real gas calculations with 2-$\gamma$ assumption across the shock. The model is further tested using mixtures with different specific heat ratios (ranging from 1.1 to 1.5) and various angles of the incoming shock (ranging from 16° to 50°) to resemble different scenarios of the triple shock reflection. We show that regardless of the mixture, all the frozen composition calculations overlap with each other. However, the equilibrium composition calculations reveal that the most compressible gases exhibit the greatest deviation from the frozen calculations. To verify the accuracy of the model, detonation experiments with self-propagating enlarged cell structures are conducted. The triple point reflection process was monitored with high-speed schlieren videos permitting to measure the strength and angle of the incoming shock and newly formed Mach shock. The experiments were performed in mixtures of $2C_3H_8/5O_2$, $CH_4/2O_2$, $CH_4/2O_2/0.44CO_2$, $2H_2/O_2/7Ar$ and $2H_2/O_2/7He$, which span the degree of cellular regularity of detonations and compressibility of gas in reactive gases. The experimental data of the detonation dynamics are compared with the model predictions, and a high level of agreement between the two is observed.

## 1 Introduction

Experiments in reactive mixtures show that detonation waves exhibit a highly dynamic cellular structure comprised of the incident, Mach and transverse shocks [1]. These three shock waves and the slip line, which separates gas passing through the incident and reflected shocks with the gas passing through the Mach shock, are joined at the triple point. The periodic interaction of these three shock waves in reactive mixtures forms the cellular structure of the detonation. These interactions are believed to control the propagation mechanism, as they generate highly overdriven detonations well above the Chapman Jouguet (CJ) speed, $D_{CJ}$, which then decay through the cycle and reform from new triple point collisions. Therefore, the outcome of the triple point reflection off a wall or another triple point is important in predicting the detonation's propagation mechanism. In this regard, the most common method used in interpreting the experimental observation is the shock polar calculations which use the oblique shock jump relations and assume a perfect gas, with a constant ratio of specific heat [2,3]. In this theory given the Mach number and the inclination angle of the incoming oblique wave, the triple point configuration before and after reflection can be determined by matching the flow deflection angle and the pressure

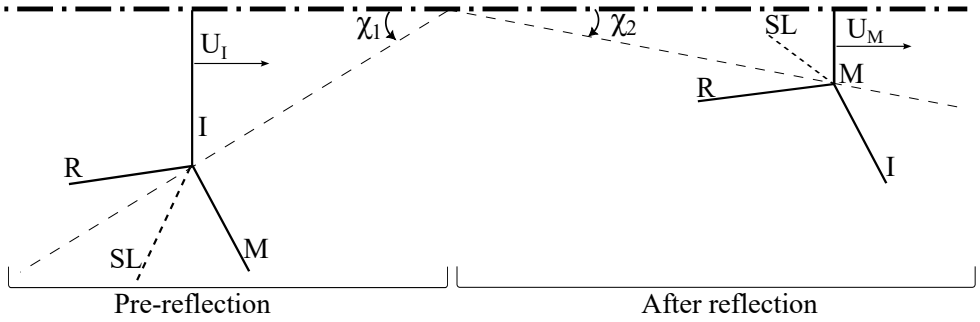


(a) Schematic of the triple point prior to and after the reflection from the top wall

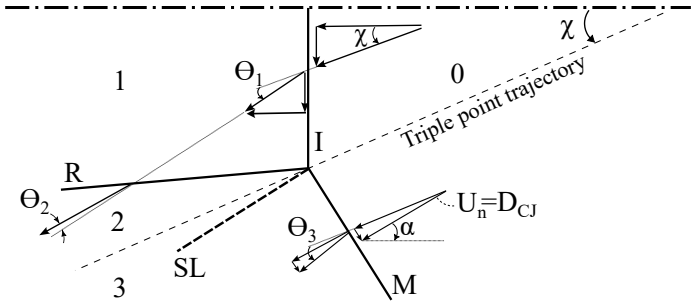


(b) Detailed velocity relationships and shock angles prior to reflection

Figure 1: Schematic of the triple point reflection from the wall. a) U: velocity, R: reflected shock, M: Mach shock, SL: slip line, I: incident shock and $\chi$: angle of the triple point trajectory with the horizontal line. b) $U_n$: normal velocity, $D_{CJ}$: CJ speed, $\theta$: deflection angle, $\alpha$: inclination angle and $\chi$: triple point angle, the incident shock (I), reflected shock (R) and Mach shock (M) respectively.

across the slip line. The pre-reflection region represents the end of a detonation cell and the region after the reflection shows the formation of a new cell with a new reactive Mach shock, as illustrated in Fig. 1. Due to the simplicity and usefulness of this method, many researchers in the past focused on employing this theory to the detonation cell case [2, 4]. However, simultaneous experimental observations around the same period revealed that the reaction occurs rapidly behind the newly formed Mach shock, and the leading shock is an overdriven detonation [5]. In this work, the dynamics of the decaying shocks and their reflection, which correspond to the end and beginning of a detonation cell, are predicted using the three-shock theory. To do so, we reformulate the triple point reflection model by assuming the Mach shock is reactive. The objective of the present work is to determine the strength of the lead shock following the triple-point collision. The predictions of the model are then validated with the experiments of propagating detonations in narrow channels with an enlarged cell size structure, such that the reflection dynamics can be resolved with high-speed schlieren images.

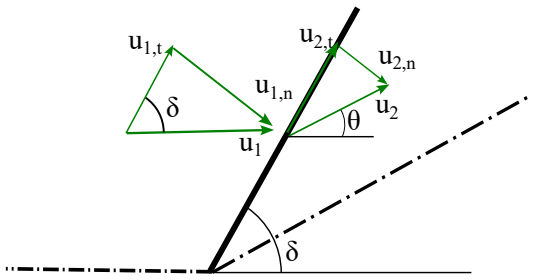


Figure 2: Oblique shock from a sharp corner

## 2 Modelling: Three shock theory

### 2.1 Methodology

Shock polar analysis is the most widely used calculation that involves shock matching at the triple point. In this theory, it is assumed that the flow is steady within a reference frame fixed to the triple point, allowing for the standard shock-polar analysis to be applied [6]. The triple point trajectory angles with respect to the top wall are $\chi_1$ and $\chi_2$ before and after the reflection, as was shown in Fig. 1a. All the waves in this problem are considered oblique shocks with respect to the triple point reference frame. This model only requires three inputs: the mixture composition, the incoming shock normal velocity ($U_n$) and the inclination angle of the shock ($\alpha$) in the pre-reflection region, shown in Fig. 1b. The correct value of $\chi$ will be calculated using the bisection method such that:

$$\theta_1 - \theta_2 = \theta_3 \qquad ; \qquad p_3 = p_2 \tag{1}$$

By extending this analysis to reactive gases, a triple shock model is developed to treat reactive collisions with detailed chemical thermodynamic properties. In this model, real gas calculations of the triple point reflection are performed using Cantera [7] for evaluation of the gas properties.

To illustrate, consider a simple oblique shock resulting from a sharp corner. From trigonometric relationships, the normal and tangential components of the velocities are expressed as:

$$u_{n,1} = u_1 \sin\delta, \quad u_{n,2} = u_2 \sin(\delta - \theta),$$
$$u_t = u_1 \cos\delta = u_2 \cos(\delta - \theta).$$

Using Cantera to obtain the thermodynamic properties of state 1, in combination with the Shepherd Shock and Detonation Toolbox (SDToolbox) [9], CJ velocity $u_{n,1}$ can be determined. Specifically, the *PostShock_fr* function in SDToolbox can be employed for calculating inert shock properties, while *PostShock_eq* function can be used for reactive oblique shocks. Knowing the gas properties in state 2 ($p_2, \rho_2$), the downstream normal velocity $u_{n,2}$ can be calculated using conservation of mass ($\rho_2 u_{n,2} = \rho_1 u_{n,1}$). For a fixed deflection angle $\theta$, the oblique shock angle $\theta$ can be determined from the relationship:

$$\frac{u_{n,1}}{u_{n,2}} = \frac{\tan\delta}{\tan(\delta - \theta)}.$$

Solving this problem will enable the anticipation of both the dynamic and thermodynamic properties of the incident and Mach shocks prior to and following the reflection.

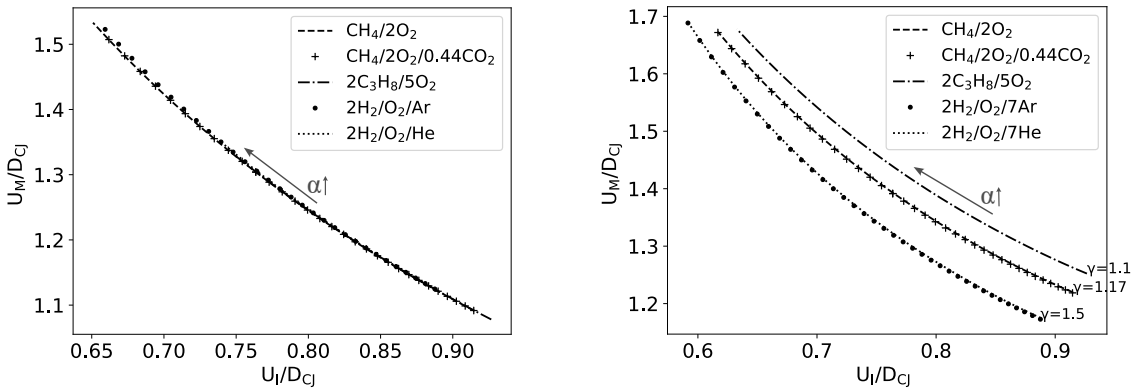


(a) Frozen composition calculation

(b) Equilibrium composition calculation

Figure 3: Prediction of the model for the inert and reactive calculations in different mixtures with varying incoming angles $\alpha$. All the velocities are non-dimensionalized by the CJ speed. $\gamma$ is the specific heat ratio of each mixture at initial condition.

### 2.2 Model's prediction

The outcomes of the Mach shock strength predictions against incoming velocity, denoting the end and onset of a new cell, are presented in Fig. 3. In this illustration, $U_I$ and $U_M$ represent the normal velocity at the end of the cell and the newly formed Mach shock velocity, as depicted in Fig.1a. To generalize the prediction of the model to different scenarios, we fixed the effects of the chemistry and the incoming shock velocity. This was achieved by assuming that the normal shock velocity of the incoming Mach shock is CJ speed for each given mixture. To alter the deflection angle of the shock, the incoming flow angle, $\alpha$, is adjusted within a range of 16° to 52°. Figure 3 (a) demonstrates the predictions in scenarios devoid of heat release, where all predictions exhibit overlap irrespective of mixture composition and initial pressure. The variations in results are solely attributed to changes in the incoming flow angle. An increase in $\alpha$ results in a weaker incident shock at the cell's end and a stronger Mach shock reflection. Conversely, lower $\alpha$ exhibits the opposite pattern, leading to a heightened incident shock at the cell's end and a weak formation of the Mach shock. Similar patterns are noted in equilibrium calculations when it comes to the impact of $\alpha$, Fig. 3 (b). Nevertheless, the inclusion of heat release introduces disparities in the prediction of $U_M$ as opposed to inert gas computations. The opposite ends of the spectrum, denoting the weakest and strongest predicted Mach shock, are associated with the least compressible composition of $2H_2/O_2/7Ar$ and the most compressible composition of $2C_3H_8/5O_2$. The results obtained are mainly influenced by the compressibility of the mixtures, which clarifies why mixtures with similar compressibility such as hydrogen-oxygen-argon and hydrogen-oxygen-helium exhibit similar outcomes when plotted together. The model's predictions show limited sensitivity to variations in initial pressure.

## 3 Experiment

### 3.1 Experimental set-up

To resolve the reflection dynamics of a triple point in an enlarged cell, experiments are conducted in a 3.4-m-long thin aluminum channel with an internal cross-section height

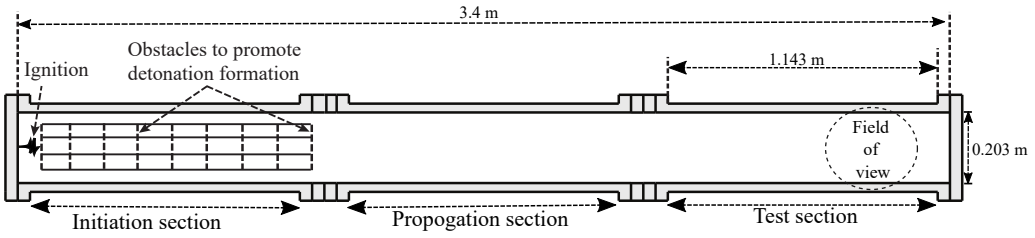


Figure 4: A schematic of the experimental apparatus to study the triple point reflection.

Table 1: The experimental test gases evaluated at $T_0 = 293$ K.

| Mixture | $p_0$ [kPa] | $\gamma$ | $D_{CJ}$ |
|---|---|---|---|
| $CH_4/2O_2$ | 6 | 1.17 | 2267 |
| $2C_3H_8/5O_2$ | 3.5 | 1.1 | 2474 |
| $2H_2/O_2/7Ar$ | 4.1 | 1.5 | 1602 |
| $2H_2/O_2/7He$ | 9.37 | 1.5 | 3611 |

of 0.203-m and width of 0.019-m. The detail of the experimental setup is shown in Fig. 4. The propagation process was visualized using the Z-type schlieren technique using 0.31-m diameter mirrors, a high-speed Phantom v1210 camera and a continuous white light source from an incandescent automotive light bulb. The inter-frame time was 12.9 $\mu s$ for a resolution of $384 * 288$ px$^2$.

Table 1 shows the experimental test gases along with their thermo-chemical properties calculated using the San Diego chemical mechanism [8]. In order to increase the size of the detonation cell, the test gas was initiated at the minimum pressure that would still allow a successful detonation initiation. Several test gases were selected to control the gas response to the compressibility effect, $\gamma$, as identified as a controlling parameter in the preceding modelling section. The chosen compositions span a spectrum from highly regular structure detonations (hydrogen-based mixtures highly diluted with argan or helium) to highly irregular cellular structures (methane and propane mixtures). Hydrogen-based mixtures exhibit significantly lower compressibility compared to their hydrocarbon counterparts. In the case of hydrogen mixtures with argon or helium, by adjusting the initial pressure and mixture composition, the impact of compressibility and kinetics sensitivity to the shock state remains constant, while transport properties like kinematic viscosity, speed of sound, and densities change.

### 3.2 Experimental results

The results of the schlieren images of the detonation front obtained in different mixtures are shown in Fig. 5. In all the mixtures displayed, the detonation wave is propagating from left to right and the first frame depicts the weak Mach shock before the reflection. Following the triple point reflection off the upper wall, a new reactive Mach shock forms and travels near the top wall. Figure 5a, shows the time evolution of the newly generated Mach shock overtaking the original front in the mixture of $CH_4/2O_2$. Behind the Mach shock after a short induction zone, the reaction front is burning all the shocked reactive gas. However, as a result of the buildup of unreacted gas along the shear layer before the reflection, the formation of the unburned pockets of gas that separate from the main front is observed (frames C and D). This phenomenon has been previously documented in existing literature [10] as one of the main features of detonations with irregular cellular structures.

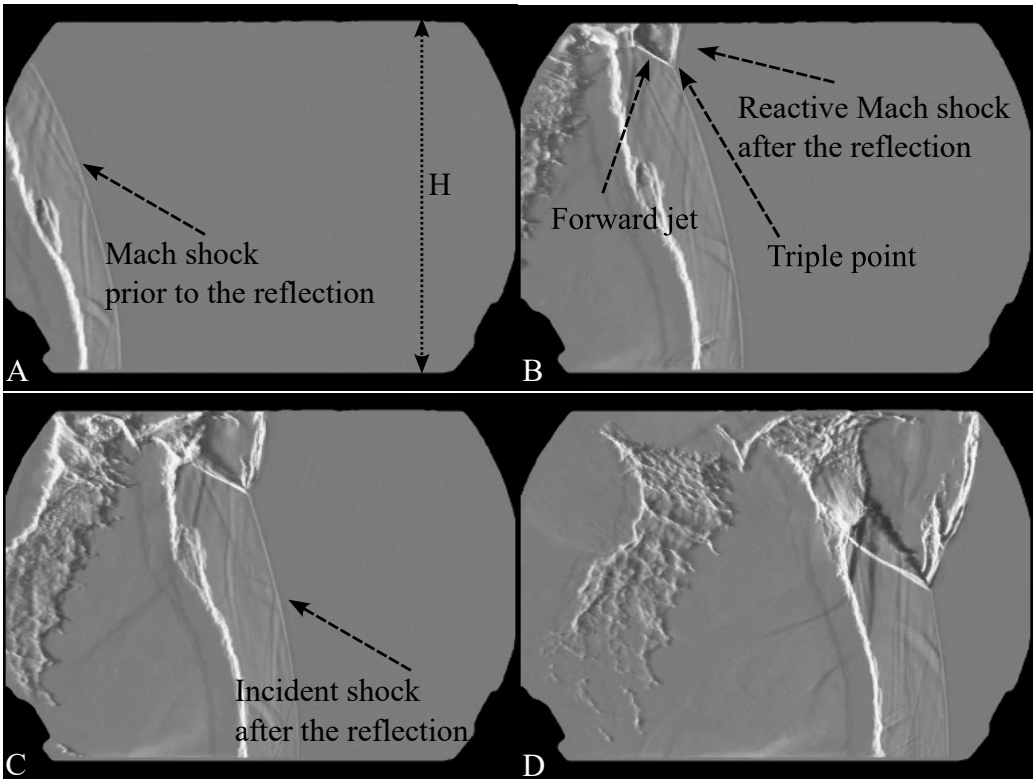


(a) $CH_4/2O_2$ at $p_0 = 6$ kPa

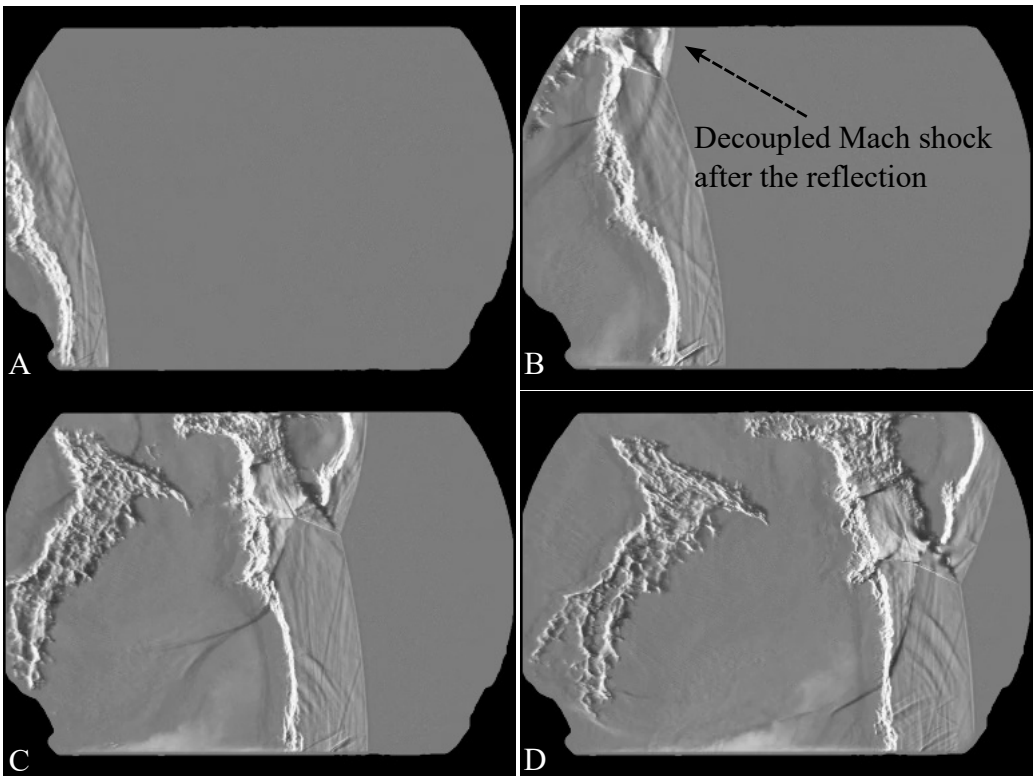


(b) $CH_4/2O_2/0.44CO_2$ at $p_0 = 9.3$ kPa

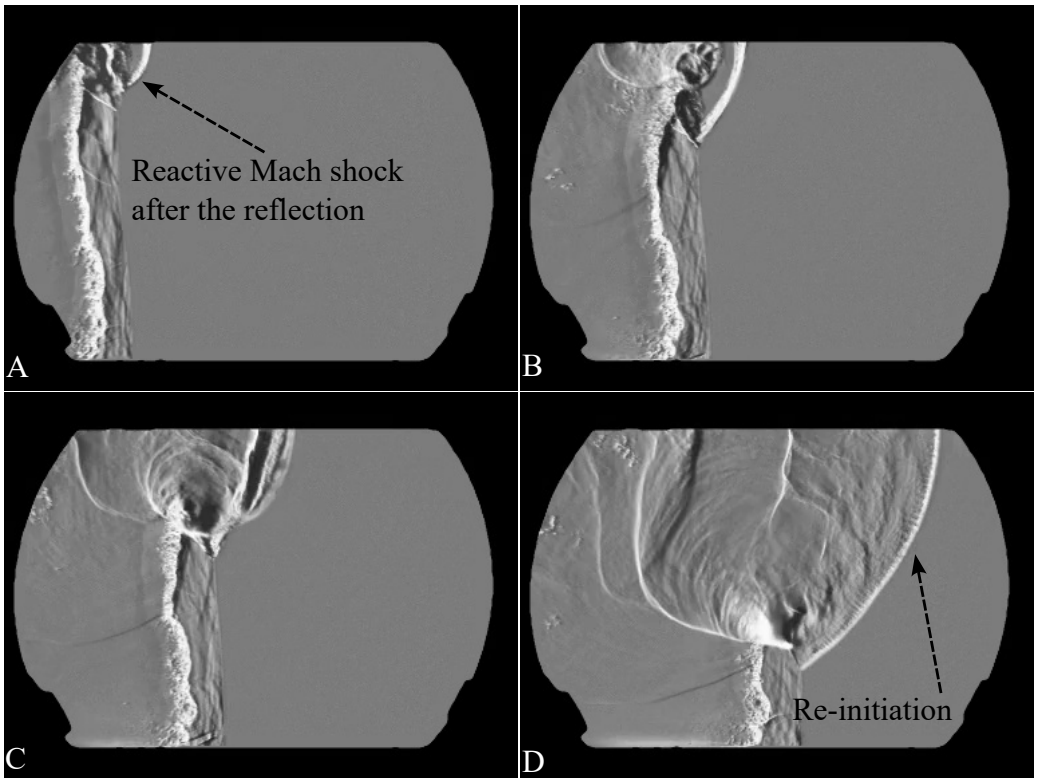


(c) $2C_3H_8/5O_2$ at $p_0 = 3.5$ kPa

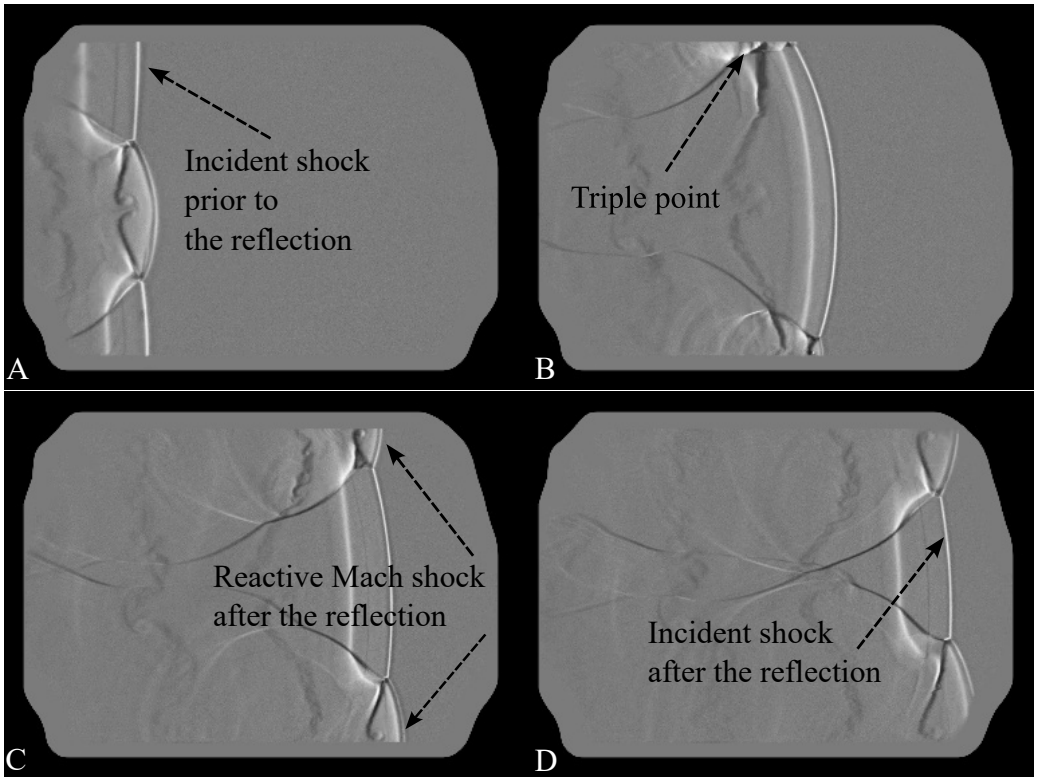


(d) $2H_2/O_2/7Ar$ at $p_0 = 4.1$ kPa

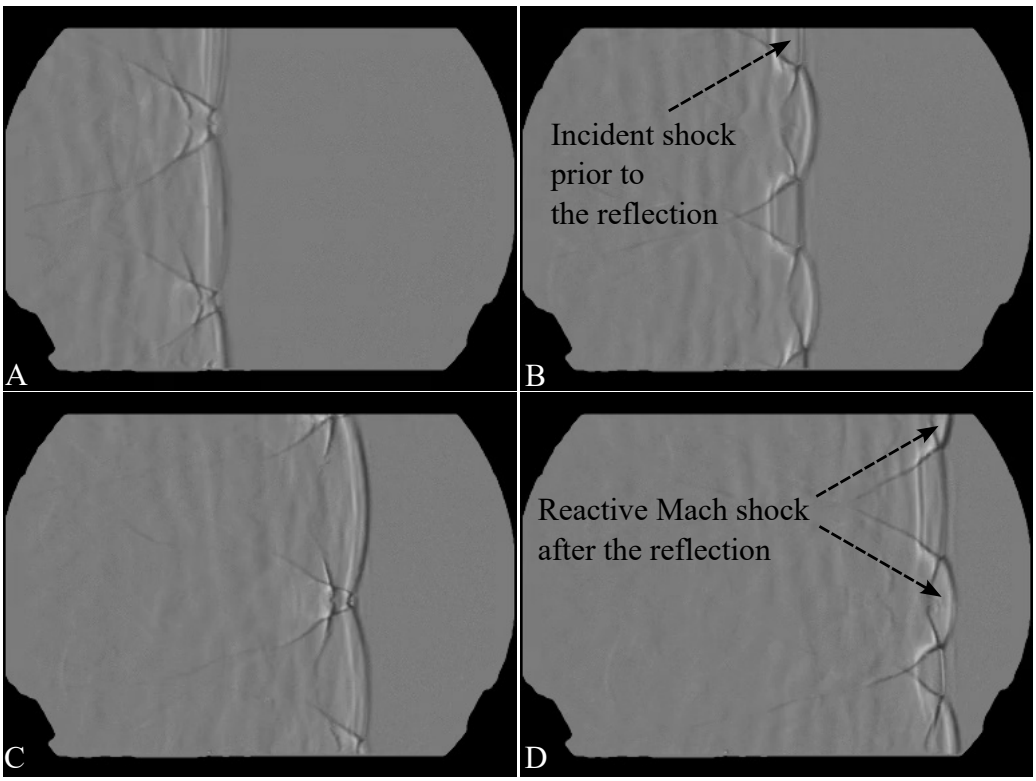


(e) $2H_2/O_2/7He$ at $p_0 = 9.37$ kPa

Figure 5: Sequential frames of the schlieren images of the triple point reflection in the different reactive mixtures tested at $T_0 = 293$ K. The channel height is H = 0.203 m.

This phenomenon is also observed in the mixture of $CH_4/2O_2/0.44CO_2$, presented in Fig. 5b. One can see that immediately after the shock reflection, the reaction and shock fronts are attached (frame B). However, after some time the region of the shocked unburned gas behind the front is enlarging and the Mach shock is degrading (frames C and D). In the mixture of $2C_3H_8/5O_2$, the initial observation entails a strong reactive Mach shock reflection. Additionally, due to an explosion near the upper wall, reinitiation occurs, as displayed in Fig. 5c. The existence of a turbulent reaction front, flow circulation, and local explosions vividly illustrates the stochastic nature of these irregular mixtures. Furthermore, in all hydrocarbon mixtures where adequate compression can occur behind the Mach stem, a forward jet materializes along the shear layer. In previous studies, it has been demonstrated that in mixtures with low specific heat ratios, the shock is driven by a strong internal jet during the initial stages following the reflection. This internal jet serves to locally enhance reactivity through turbulent mixing [11, 12].
The sequence depicting the reflection of triple points off the top and bottom walls in two highly regular structure mixtures, hydrogen diluted with either argon or helium, is illustrated in Fig. 5d and 5e. In contrast to previous hydrocarbon mixtures, no signature of unreacted gas pockets, explosions or strong forward jets were observed.

The velocity profiles of two selected mixture of $2H_2/O_2/7Ar$ with very regular cellular structure and $CH_4/2O_2$ with the irregular structure are shown in Fig. 6. In all the mixtures, the velocity of the incoming Mach shock before reflection is measured along the axis of symmetry, while the velocity of the Mach shock after the reflection is measured on the top wall. The incoming Mach shocks' velocities before reflection range from 25%

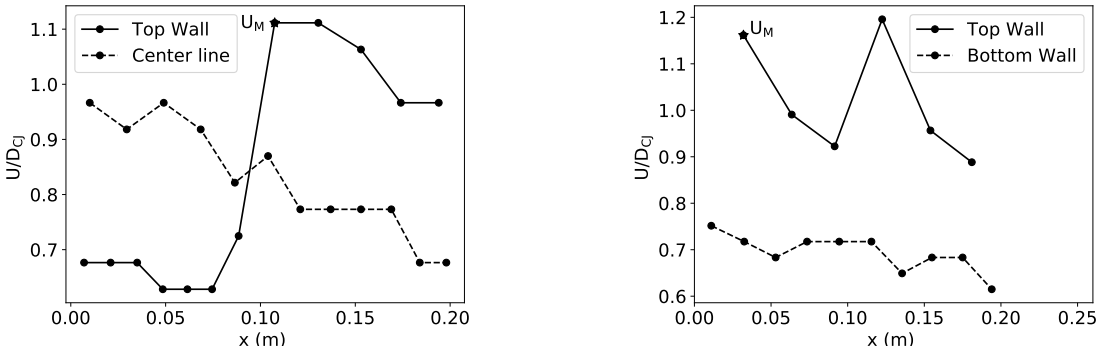


(a) $2H_2/O_2/7Ar$ (b) $CH_4/2O_2$

Figure 6: The local speed profile of the detonations occurring along the upper and lower walls of the shock tube. $U_M$: Mach shock velocity after the reflection.

to 45% below the CJ speed, with the shocks decaying as they propagate (indicated by dashed lines). However, upon reaching the top wall, the detonation becomes overdriven immediately after reflection in all cases (depicted by solid lines).

## 4 Model and experiment: predicted Mach shock velocity

By extracting shock velocities before and after reflection from the experiments, we compare these measurements with the model's predictions under the same mixture conditions and initial pressures as those in the experiments. Figure 7 illustrates the non-dimensionalized incoming incident shock velocity, $U_I$ (representing the end of a detonation cell), versus the newly formed Mach shock speed, $U_M$ (representing the beginning of a cell), with all velocities normalized by the CJ speed. In hydrogen-argon and hydrogen-helium mixtures, where the deviation between equilibrium and frozen calculations is minimal, the two lines intersect. This phenomenon is attributed to higher $U_M$ values, corresponding to very high post-shock temperatures, leading to the endothermic nature of the reaction in equilibrium calculations.

In Fig. 7, all the experimental velocities represented by symbols are normalized using the Mach shock velocity before reflection. The error bars in the plots indicate the uncertainty in velocity measurements obtained from the experiments. Across all cases, the disparity between the model and experiment ranges from as low as 3% to as high as 19%. In general, when the newly formed Mach shock is reactive, the model's equilibrium composition calculation closely matches the experimental findings. This alignment is especially pronounced in more compressible gases, where deviations between the predictions of inert and reactive calculations become more noticeable.

The discrepancies between the model and experimental results can be attributed to factors like the presence of hydrodynamic instabilities and the curved characteristics of the detonation front, which are not accounted for in the modeling process.

## 5 Conclusion

In this work, we focused on the prediction of the dynamics of the newly formed Mach shock after the triple point reflection within the cellular structure of the detonation. We modified

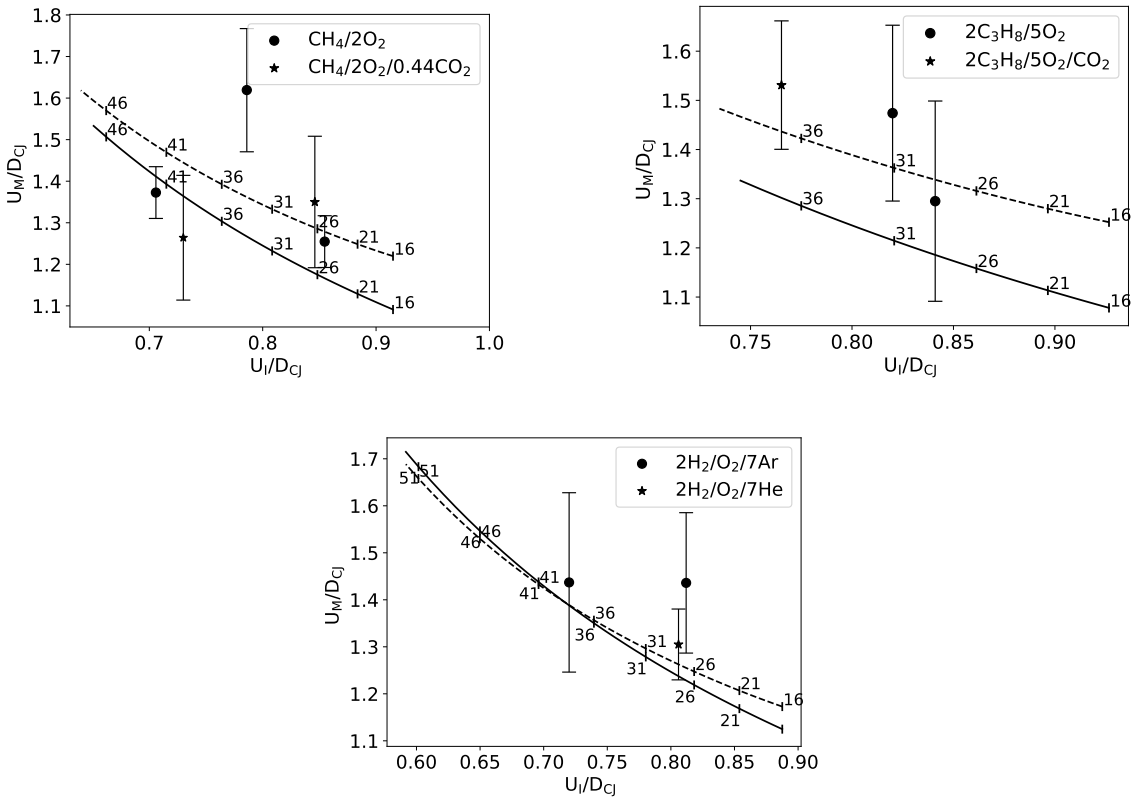


Figure 7: Validation of the model against experimental measurements. Solid lines: Frozen composition calculations and dashed lines: equilibrium composition calculations. The numbers on the curves are $\alpha$ which is varying between 16-52 °.

the available three shock theory by incorporating the assumptions of a reactive Mach shock and implementing real gas calculations with a 2-$\gamma$ assumption. Our study revealed that in the inert gas calculations, the predictions of the Mach stem velocity remained consistent irrespective of the composition of the mixture. However, in the equilibrium composition calculations, the outcomes are highly sensitive to the compressibility of the test gas.

To further validate the results obtained from our modelling approach, experiments were carried out using test gases with a wide range of mixture compressibility, providing a comprehensive assessment of the model's accuracy. Taking into account the uncertainties inherent in experimental measurements, the level of agreement observed between the experimental data and the model predictions demonstrates the effectiveness of the model in accurately capturing and predicting the dynamics of detonations.

## 6 Acknowledgments

This work was supported by AFOSR grant FA9550-23-1-0214, with Dr. Chiping Li as program monitor and the NSERC Discovery Grant "Predictability of detonation wave dynamics in gases: experiment and model development".

## References


[1] Fickett, W., Davis, W. Detonation: theory and experiment. University of California Press, 1979.

[2] Oppenheim, A., Smolen, J., Kwak, D., Urtiew, P. On the dynamics of shock intersections. pages 119–136, 1972.

[3] Oppenheim, A., Smolen, J., Zajac, L. Vector polar method for the analysis of wave intersections. Combustion and Flame, 12(1):63–76, 1968.

[4] Strehlow, R.A., Adamczyk, A.A., Stiles, R.J. Transient studies of detonation. Technical report, Illinois Univ Urbana Dept of Aerospace and Aeronautical Engineering, 1971.

[5] Strehlow, R.A., Crooker, A.J. The structure of marginal detonation waves. Acta Astronautica, 1(3-4):303–315, 1974.

[6] Courant, R., Friedrichs, K. Supersonic flow and shock waves, interscience pulishers. Inc., New York, 1948.

[7] Goodwin, D.G., Speth, R.L., Moffat, H.K., Weber, B.W. Cantera: An object-oriented software toolkit for chemical kinetics, thermodynamics, and transport processes, 2021.

[8] Williams, F. Chemical mechanism: Combustion research group at uc sandiego, 2014.

[9] Kao, S., Shepherd, J. Numerical solution methods for control volume explosions and znd detonation structure, 2008.

[10] Xiao, Q., Radulescu, M.I. Role of instability on the limits of laterally strained detonation waves. Combustion and Flame, 220:410–428, 2020.

[11] Bhattacharjee, R., Lau-Chapdelaine, S.S.M., Maines, G., Maley, L., Radulescu, M.I. Detonation re-initiation mechanism following the mach reflection of a quenched detonation. Proceedings of the Combustion Institute, 34(2):1893–1901, 2013.

[12] Maley, L. On shock reflections in fast flames. University of Ottawa, Master Thesis, 2015.

# Chapter 7

# Summary of the work

This thesis focuses on investigating detonation cellular structures at both large and sub-cellular scales. The goal is to gain a deeper understanding on how the dynamics of small scale structures relate to those on large scale in the presence of losses associated with curvature and friction losses. To achieve this, the research findings were presented across five articles.

In the first journal paper, we investigated the lateral diffraction of shock fronts in irregular cellular detonations with very fine-scale fronts. We conducted experiments on detonation diffraction in a 2D channel configuration using stoichiometric mixtures of ethylene, ethane, and methane with oxygen as the oxidizer. The critical channel heights and global curvatures were found to be in excellent agreement with the critical curvatures independently measured by Xiao and Radulescu [22] in quasi-steady experiments using exponential horns for the three mixtures tested. This suggests that the dynamics of propagating detonations can be effectively captured by the behaviour of a single unit cell propagating in a diverging ray tube and the concept of the global curvature on large scales is meaningful.

In the second paper, we explore whether incorporating the global effect of curvature is effective in capturing weakly transient phenomena of detonation formation. A novel technique was introduced to isolate the process of reactive Mach shock formation from the reflection of two decaying shocks. Three distinct regimes were identified: detonation formation, ignition behind the decaying Mach shock, and Mach shock without ignition. We demonstrated that the formation of a quasi-steady detonation wave aligns with the theory of weakly unsteady curved detonations. However, the critical conditions distinguishing between ignition and no-ignition regimes in both mixtures can be predicted using a decay rate model that accounts for the expansion behind the decaying shock.

In the third paper, we investigated the propagation of detonations through narrow channels. Unlike in detonation diffraction and initiation experiments, the detonation wave in this case is quasi-steady, with lateral flow divergence driven by boundary layer effects along the side walls. We used argon and helium as diluents in a hydrogen-oxygen mixture because, in the absence of losses, both diluents have the same kinetics, Mach number, and specific heat ratio, which should result in similar cellular dynamics. However, the experiments revealed differences in velocity deficits and cell sizes, even though the induction

zone length remained constant across the mixtures. These differences were explained by considering the impact of lateral flow divergence caused by boundary layer losses. A quasi-two-dimensional inviscid approach with two-step chemistry was used, modelling losses due to viscous boundary layers by incorporating an equivalent mass divergence in the lateral direction using Fay's source term formulation and Mirels' compressible laminar boundary layer solutions. The numerical simulations showed excellent agreement with experimental results, both in terms of cell dynamics and velocity deficits. These results indicate that even with the presence of the small-scale cellular structure in the detonation front, detonation will respond to a global flow divergence due to the long reaction zone time scale.

In the fourth paper, inspired by previous works [31–33] showing that detonation structure often recovers a quasi-one-dimensional form similar to the ZND model, including an average sonic surface, we measured the mean pressure evolution of detonations propagating in narrow channels, accounting for the presence of losses. The hydrodynamic thickness was found to be approximately one cell width, $\lambda$. In terms of modelling, for regular mixtures with a long reaction zone, the simple one-dimensional ZND model with the loss term effectively predicts the pressure evolution of the reflected wave. However, for the irregular methane-oxygen mixture, where the ZND model fails to capture the global reaction zone structure, we proposed a simplified one-step combustion model tailored to the global reaction zone. This model closely matched the decay rate observed in experiments up to the sonic surface.

In the final paper, we focused on predicting the dynamics of the newly formed Mach shock after triple point reflections within the cellular structure of detonations. We extended the existing three-shock theory by incorporating the assumptions of a reactive Mach shock and implementing real gas calculations. Our study showed that in inert gas simulations, the Mach stem velocity predictions remained consistent regardless of the mixture composition. However, in equilibrium composition calculations, the results were highly sensitive to the compressibility of the test gas. To validate our model, we conducted experiments using test gases with a wide range of compressibility, allowing for a thorough assessment of the model's accuracy. Despite the inherent uncertainties in experimental measurements, the close agreement between the experimental data and model predictions demonstrated the model's effectiveness in accurately capturing and predicting detonation dynamics.

## 7.1 Future works

The closure of the problem further requires a comprehensive description of the gases burning within the cellular structure. This includes ignition behind the Mach shock, incident shock and reflected shocks, as well as the burning process of gas pockets left behind. In Chapter 3 of this work, we successfully isolated the formation and dynamics of the Mach shock. Our experiments demonstrated three regimes: one with no ignition, one with ignition and another where detonation occurs. Due to the importance of the ignition process and its substantial contribution to the detonation front in a detonation cell, further investigation is needed to fully describe the ignition regime. The experimental isolation of a

single Mach reflection offers the opportunity to use a deterministic and reproducible set-up to model the feedback of the reactivity provided by the different burning regions on the lead shock dynamics. The well-posedness of the problem also permits modeling each sub-process in an unambiguous way.

Although the above experiments offer insights into the ignition process and its effect on the front, they do not provide an average description of the cellular structure. To do so the experiments conducted in thin channels allowed us to determine the location of the sonic surface and establish the average structure. This setup appears as the most suitable to finally validate a sub-cell model. It also appears to provide the framework to test the effect of non-steadiness, for example, allowing the detonation to transmit from a much wider channel into the thinner one, and monitor the relaxation to the new steady-state solution. This would provide the test bed for a $D$-$\dot{D}$-$\kappa$ description for cellular detonations.

# References


[1] J. S. Lee and M. I. Radulescu. On the hydrodynamic thickness of cellular detonations. *Combustion, Explosion and Shock Waves*, 41:745–765, 2005.

[2] W. Fickett and W. C. Davis. *Detonation : Theory and Experiment.* University of California Press, 1979.

[3] M. I. Radulescu, G. J. Sharpe, J. S. Lee, C. B. Kiyanda, A. J. Higgins, and R. K. Hanson. The ignition mechanism in irregular structure gaseous detonations. *Proceedings of the Combustion Institute*, 30(2):1859–1867, 2005.

[4] J. S. Lee. Dynamic parameters of gaseous detonations. *Annual Review of Fluid Mechanics*, 16(1):311–336, 1984.

[5] J. S. Lee. *The Detonation Phenomenon.* Cambridge University Press, 2008.

[6] M. I. Radulescu, G. Sharpe, C. K. Law, and J. H. Lee. The hydrodynamic structure of unstable cellular detonations. *Journal of Fluid Mechanics*, 580:31–81, 2007.

[7] R. Strehlow, R. E. Maurer, and S. Rajan. Transverse waves in detonations. i-spacing in the hydrogen-oxygensystem. *AIAA Journal*, 7(2):323–328, 1969.

[8] E. S. Oran, J. P. Boris, T. Young, M. Flanigan, T. Burks, and M. Picone. Numerical simulations of detonations in hydrogen-air and methane-air mixtures. In *Symposium International on Combustion*, volume 18, pages 1641–1649. Elsevier, 1981.

[9] J. E. Shepherd. Detonation in gases. *Proceedings of the Combustion Institute*, 32(1):83–98, 2009.

[10] Y. N. Denisov and Y. K. Troshin. Pulsating and spinning detonation of gaseous mixtures in tubes. *Dokl. Akad. Nauk SSSR*, 125:110–113, 1959.

[11] D. R. White. Turbulent structure of gaseous detonation. *The Physics of Fluids*, 4(4):465–480, 1961.

[12] R. I. Soloukhin. Multiheaded structure of gaseous detonation. *Combustion and Flame*, 10(1):51–58, 1966.

[13] J. M. Austin. *The role of instability in gaseous detonation.* Ph.D. Thesis, California Institute of Technology, Pasadena, California, 2003.

[14] I. O. Moen, S. B. Murray, D. Bjerketvedt, A. Rinnan, R. Knystautas, and J. H. Lee. Diffraction of detonation from tubes into a large fuel-air explosive cloud. In *Symposium International on Combustion*, volume 19, pages 635–644. Elsevier, 1982.

[15] R. A. Strehlow, R. Liaugminas, R. H. Watson, and J. R. Eyman. Transverse wave structure in detonations. *Symposium International on Combustion*, 11(1):683–692, 1967.

[16] D. H. Edwards, A. T. Jones, and D. E. Phillips. The location of the chapman-jouguet surface in a multi-headed detonation wave. *Journal of Physics D: Applied Physics*, 9(9):1331, 1976.

[17] Y. B. Zeldovich. On the theory of the propagation of detonation in gaseous systems. *Zh. Éksper. Teoret. Fiz.*, 10:542–568, 1940.

[18] J. Von Neumann. Theory of shock waves. Technical report, Army Air Forces Headquarters, Wright Field, Ohio, 1943.

[19] W. Döring. On detonation processes in gases. *Annalen der Physik*, 43:421–436, 1943.

[20] Q. Xiao, A. Sow, B. M. Maxwell, and M. I. Radulescu. Effect of boundary layer losses on 2D detonation cellular structures. *Proceedings of the Combustion Institute*, 38:3641–3649, 2021.

[21] J. C. Libouton, M. Dormal, and P. J. Van Tiggelen. Reinitiation process at the end of the detonation cell. *Gasdynamics of Detonations and Explosions*, pages 358–369, 1981.

[22] Q. Xiao and M. I. Radulescu. Role of instability on the limits of laterally strained detonation waves. *Combustion and Flame*, 220:410–428, 2020.

[23] M. I. Radulescu. A detonation paradox: Why inviscid detonation simulations predict the incorrect trend for the role of instability in gaseous cellular detonations? *Combustion and Flame*, 195:151–162, 2018.

[24] M. I. Radulescu and B. Borzou. Dynamics of detonations with a constant mean flow divergence. *Journal of Fluid Mechanics*, 845:346–377, 2018.

[25] R. Mevel, Q. Xiao, S. Gallier, and M. I. Radulescu. Hydrogen-oxygen-argon detonation diffraction in a narrow channel. *Proceedings of the Twenty-six ICDERS, Boston*, 2017.

[26] H. Nakayama, T. Moriya, J. Kasahara, A. Matsuo, Y. Sasamoto, and I. Funaki. Stable detonation wave propagation in rectangular-cross-section curved channels. *Combustion and Flame*, 159(2):859–869, 2012.

[27] H. Nakayama, J. Kasahara, A. Matsuo, and I. Funaki. Front shock behavior of stable curved detonation waves in rectangular-cross-section curved channels. *Proceedings of the Combustion Institute*, 34(2):1939–1947, 2013.

[28] D. H. Edwards, G. O. Thomas, and M. A. Nettleton. The diffraction of a planar detonation wave at an abrupt area change. *Journal of Fluid Mechanics*, 95(1):79–96, 1979.

[29] D. H. Edwards and G. O. Thomas. Diffraction of a planar detonation in various fuel-oxygen mixtures at an area change. In *Gasdynamics of detonations and explosions. International colloquium on gasdynamics of explosions and reactive systems, 7th, Gottingen, West Germany, August 20-24, 1979, technical papers*, 1981.

[30] E. Schultz. *Detonation diffraction through an abrupt area expansion*. Ph.D. Thesis, California Institute of Technology, Pasadena, California, 2000.

[31] M. I. Radulescu, G. Sharpe, and C. K. Law. Effect of cellular instabilities on the blast initiation of weakly unstable detonations. In *Proceedings of the 21st International Colloquium on the Dynamics of Explosions and Reactive Systems, Poitiers*, 2007.

[32] B. Maxwell, R. Bhattacharjee, S. Lau-Chapdelaine, S. Falle, G. Sharpe, and M. I. Radulescu. Influence of turbulent fluctuations on detonation propagation. *Journal of Fluid Mechanics*, 818:646–696, 2017.

[33] M. Reynaud, F. Virot, and A. Chinnayya. A computational study of the interaction of gaseous detonations with a compressible layer. *Physics of Fluids*, 29(5):056101, 2017.

[34] J. B. Bdzil and D. S. Stewart. The dynamics of detonation in explosive systems. *Annu. Rev. Fluid Mech.*, 39(1):263–292, 2007.

[35] R. Klein, J. C. Krok, and J. E. Shepherd. Curved quasi-steady detonations, asymptotic analysis and detailed chemical kinetics. 1995.

[36] Chemical mechanism: Combustion research group at uc san diego. https://web.eng.ucsd.edu/mae/groups/combustion/mechanism.html, 2014.

[37] L. He and P. Clavin. On the direct initiation of gaseous detonations by an energy source. *Journal of Fluid Mechanics*, 277:227–248, 1994.

[38] M. Short and J. B. Bdzil. Propagation laws for steady curved detonations with chain-branching kinetics. *Journal of Fluid Mechanics*, 479:39–64, 2003.

[39] J. Yao and D. S. Stewart. On the normal detonation shock velocity-curvature relationship for materials with large activation energy. *Combustion and Flame*, 100(4):519–528, 1995.

[40] P. Vidal. Critical slow dynamics of detonation in a gas with non-uniform initial temperature and composition: a large-activation-energy analysis. *International journal of spray and combustion dynamics*, 1(4):435–471, 2009.

[41] H. Lee and D. S. Stewart. Calculation of linear detonation instability: one-dimensional instability of plane detonation. *Journal of Fluid Mechanics*, 216:103–132, 1990.

[42] Q. Xiao and M. I. Radulescu. Dynamics of hydrogen–oxygen–argon cellular detonations with a constant mean lateral strain rate. *Combustion and Flame*, 215:437–457, 2020.

[43] Q. Xiao, R. Mevel, S. Gallier, and M. I. Radulescu. Ray-tracking methods for characterizing the dynamics of curved detonation. *Physics of Fluids*, 34(6), 2022.

[44] H. Hornung. Regular and mach reflection of shock waves. *Annual review of Fluid Mechanics*, 18:33–58, 1986.

[45] A. K. Oppenheim, J. J. Smolen, D. Kwak, and P. A. Urtiew. On the dynamics of shock intersections. In *Fifth Symposium International on Detonation, ONR, Department of Navy, Arlington, Va*, pages 119–136, 1972.